Università degli Studi di Napoli
"Federico II"

Facoltà di Ingegneria

Dottorato di Ricerca in "Ingegneria Aerospaziale, Navale e della Qualità" – XXVII Ciclo

Settore scientifico disciplinare ING-IND/05: Impianti e Sistemi Aerospaziali

Developing Innovative Inertial Systems based on advanced MEMS sensors

Dr. Alessandro Simonetti

Tutors:

Ch.mo Prof. Ing. Domenico Accardo

Ing. Domenico De Simone (Axitude s.r.l.)

Abstract

Current technological improvements allow for the realization of MEMS inertial sensors that have several advanced peculiarities such as low production cost, wide bandwidth, high-reliability, small-size, low-power consumption, and lightweight configuration. These advantages combined with new generation MEMS higher levels of accuracy and the development of innovative algorithms is allowing MEMS technology to replace expensive, bulky, heavy and power requiring Fiber Optic Gyroscopes in most applications.

This thesis deals with the development of various innovative MEMS-based inertial systems suitable to accomplish different tasks.

First, a low-cost Inertial Navigation System solution composed of industrial-grade inertial sensors, magnetometer and GNSS antenna/receiver suitable for Unmanned Aircraft Systems applications is shown. Such aeronautical platforms require attitude determination capabilities more enhanced than the standard attitude measurement accuracy FAA requirements.

Then, a land navigator system built around an Inertial Measurement Unit with quasi-tactical level gyroscopes linked with a GNSS equipment and an odometer is exposed. Both civil and military applications are demanding for self-contained, dead-reckoning systems able to provide a continuous and reliable Position, Velocity and Timing solution even in GNSS denied and degraded environments.

Finally, a ZUPT algorithm able to accurately initialize a MEMS-based INS navigation state and north-finding activities employing tactical-grade MEMS gyroscopes are described. Each inertial navigation system shall be accurately initialized before navigation in order to improve its performance. Attitude initialization is the most difficult task to satisfy and heading self-initialization has been not considered possible for many years utilizing MEMS gyroscopes.

KEYWORDS: MEMS, UAV, Land Navigator, ZUPT, North-finding

Acknowledgements

This work would not have been possible without the contribution, support, help, advice and participation of many people.

First of all, I would like to express my deepest gratitude, appreciation and love to my parents, Giuseppe and Rosalba, for their unlimited and unconditional love, inspiration and care. They taught me the benefits of hard work and instilled in me the drive to succeed and do my best in all endeavors. There is no doubt I never would have accomplished the completion of this thesis if not for their guidance, support and encouragement.

Thanks are given to Prof. Domenico Accardo, my academic tutor, for his continuous support, encouragement and guidance throughout the period of the PhD and in particular for helping me into the realization of the applications described in this thesis. He was always present, affable and helpful for every my problem.

Then I wish to thank all the people I have met at the GMA/Axitude company during my PhD program: they always encouraged me and behaved with me like if I were a their colleague from a lot of time.

A special thank goes to my company tutor, Eng. Domenico De Simone, for his collaboration and support.

A great amount of thanks goes to all my family and friends for the encouragement and kindness they have constantly demonstrated me.

At last but not least, I want to express my immense gratitude and I would like to dedicate this thesis to the most important person of my life, my sweet and loving Annamaria, who changed my life and made me a better person. Thank you for everything, my love.

This research carried out in the GMA/Axitude company has been supported and would not have been possible without the contribution of Regione Campania through the project named “PhD in the Factory”.

Contents

List of Acronyms and Abbreviations

ADC	Analog-to-Digital Converter
AHRS	Attitude and Heading Reference System
ARW	Angular Random Walk
ATU	Aircraft Transducer Unit
CAN	Controller Area Network
CVG	Coriolis Vibrating Gyroscope
DCM	Digital Magnetic Compass
DGPS	Differential GPS
DTG	Dynamically Tuned Gyroscope
EASA	European Aviation Safety Agency
ECEF	Earth-Centered Earth-Fixed
EGNOS	European Geostationary Navigation Overlay System
EKF	Extended Kalman Filter
EUT	Equipment Under Test
FAA	Federal Aviation Administration
FOG	Fiber Optic Gyroscope
FPGA	Field Programmable Gate Array
GAGAN	GPS Aided Geo-Augmented Navigation
GNSS	Global Navigation Satellite System

GPS	Global Positioning System
HW	Hardware
IMU	Inertial Measurement Unit
INS	Inertial Navigation System
ISA	Inertial Sensors Assembly
KF	Kalman Filter
LLH	Latitude, Longitude, Height
LNS	Land Navigator System
MEMS	Micro-Electro-Mechanical-System
MRAD	Milliradian
MSA	Magnetic Sensor Assembly
MSAS	Multi-functional Satellite Augmentation System
MSU	Magnetic Sensing Unit
NED	North-East-Down
OEM	Original Equipment Manufacturer
PF	Particle Filter
PVT	Position, Velocity and Timing
RAIM	Receiver Autonomous Integrity Monitoring
RLG	Ring Laser Gyroscope
RMS	Root Mean Square
RTK	Real Time Kinematics

SBAS Satellite-Based Augmentation System

SW Software

UAS Unmanned Aerial System

UAV Unmanned Aerial Vehicle

VRW Velocity Random Walk

WAAS Wide Area Augmentation System

WGS World Geodetic System

ZUPT Zero Velocity Update

Introduction

The last decade has been characterized by a proliferation of solid-state inertial sensors, such as Micro-Electro-Mechanical-System (MEMS), due to their significant cost, size, weight, and robustness advantages. Current generation MEMS sensors are able to provide measurements with levels of accuracy very close to that demonstrated by expensive, bulky, heavy and power requiring devices based on Fiber Optic technology. This performance has been gained by exploiting innovative sensor configurations and by increasing the level of accuracy in sensor manufacturing.

The main scope of this thesis is to explore and develop low-cost innovative Hardware and Software architectures for MEMS-based inertial systems combining new generation MEMS sensors and innovative data fusion algorithms in order to replace Fiber Optic technology in most applications.

In more details, the research activities focus on the realization of MEMS-based devices and algorithms able to:

1. Compute and attitude solution suitable for Unmanned Aircraft Systems (UAS). Nowadays, UAS are largely adopted in civil and military applications such as disaster management, search and rescue missions, target detection and tracking, traffic monitoring, weather observation, collision avoidance, mapping and geophysics exploration. These aeronautical platform require an attitude solution more accurate than the standard requirements accepted so far;
2. Provide a Position, Velocity and Timing (PVT) solution with continuity and integrity for land applications. A PVT solution is usually provided by a GNSS user equipment installed on-board the host vehicle, but this solution relies on receiving at least four line-of-sight satellites signals. Scenarios such as streets surrounded by very tall buildings (usually referred as urban canyons) or mountainous areas may easily degrade or block the signals coming from the satellites. As a consequence, there is an growing demand for a device able to

compute a self-contained and affordable PVT solution, completely independent from external devices.

3. Accurately initialize an INS navigation state within a short alignment time. Especially for low-cost INS, the initial alignment is still a challenging issue because of the high noises from the low-cost inertial sensors. Nevertheless, this drawback may be overcome implementing and advanced data fusion algorithm relying on the fact that the host vehicle is at rest and non-rotating during the initialization phase;
4. Self-initialize azimuth angle. Low-cost INS usually relies on Earth's magnetic field measurements to initialize heading angle, but the accuracy of this solution is limited by external magnetic interferences and local Earth's magnetic field distortions. An alternative approach is the so-called gyrocompassing, that provides an azimuth angle observing Earth's rate horizontal component, but this procedure requires accurate and stable measurements capabilities. Hence, gyrocompassing by MEMS has not been retained possible for many years, but due to recent performance improvements it is interesting to explore again this option from both academic and industrial viewpoints.

The activities described in this thesis result from the collaboration between the Department of Industrial Engineering of the University of Naples "Federico II" and Axitude s.r.l., an Italian high technology company developing integrated inertial navigation solutions for marine, land and aeronautical applications, covering both civil and military markets.

This thesis is structured in accordance with the following outline.

Chapter 1 contains:

- an overview of UAS application scenario and the scopes of this first research theme;

- a description of the sensors and of the adopted hardware and software architectures;
- an illustration of the conducted testing activities, subdivided in lab testing, van testing and flight testing;
- finally, an explanation and a discussion of some results from carried out experimental tests.

In Chapter 2 are illustrated:

- an overview of Land Navigation context and the scopes of this second research activity;
- an explanation of the sensors and of the adopted hardware and software architectures;
- a description of the Extended Kalman Filter (EKF) implemented for this application;
- an illustration of the carried out testing activities, subdivided in lab testing, van testing and PC simulations;
- some results and discussions from conducted experimental and numerical tests.

Chapter 3 reports:

- an overview of the fine alignment task and the scopes of this third research theme;
- a block diagram model of the implemented ZUPT fine alignment algorithm;
- an accurate description of the ZUPT algorithm;
- an exposure of some ZUPT output from carried out field tests and, finally, a discussion about ZUPT algorithm pros/cons.

In Chapter 4 are exposed:

- an overview of the north-finding scenario and the scopes of this fourth research activity;
- a discussion about the adopted methods and sensors;
- a description of the testing activities;
- some results about the conducted experimental and numerical tests.

Finally, conclusions and recommendations for future research activities are explained.

Chapter 1

1.1 UAS Applications Scenario

Attitude measurement performance onboard aeronautical transport platforms is a key issue to enhance mission capabilities of current systems. Indeed, the standard attitude measurement accuracy FAA requirements, i.e. 1° rms for pitch and roll and 3° rms for heading, are intended for typical mission profiles that where adopted in the past. Currently, developing aeronautical platforms, such as Unmanned Aircraft Systems and Personal Aircraft, require high performance heading and attitude determination units to control the orientation with respect to ground or flying targets of their payloads, such as microwave and laser sensors, optical cameras, and weapons, installed in strap-down configurations [1]. UAS are more demanding in terms of attitude determination performance than manned aircraft for two main reasons: the absence of a human pilot and the need of performing autonomous flight in case of loss of data link with the Ground Control Station [2]-[3].

Since high performance INSs are very expensive and therefore not suitable for low-cost applications, contemporary research has been focused on Micro-Electro-Mechanical-System (MEMS) based INS [4].

This chapter reports the research activities into developing the Axitude innovative combined GPS Navigation and GPS-aided Attitude and Heading reference system, the AX1-GNS3 device, for UAV applications. In more details, the following sections will illustrate:

- the inertial sensors that have been chosen;
- the schematic model of the device;
- the testing strategy adopted to fully comply with the prefixed aim;
- a performance evaluation and results analysis of the conducted tests.

1.2 Adopted HW and SW Solutions

Scope of this first research activity has been to develop an innovative MEMS based INS solution for UAV applications. It has been chosen to develop this new platform following two main design guidelines:

1. to increase the performance in terms of attitude determination respect to the FAA requirements;
2. and at the same time to keep costs low.

In other words, the required increased level of accuracy shall be realized exploiting low-cost hardware. As a consequence, industrial-grade MEMS inertial sensors have been selected for this application and, in order to characterize these sensors, an Allan Variance analysis [5]-[6] has been conducted. The Allan variance method of data analysis is a time domain analysis technique originally developed to study the frequency stability of oscillators. In general, the method can be applied to analyze the noise characteristics of any precision measurement instrument. The attractiveness of this method is that the Allan variance, when plotted in logarithmic scales, can discriminate different contributing error sources by simply examining the varying slopes on the Allan plot.

Figures 1.1 and 1.2 report an Allan Variance plot of the gyroscopes and of the accelerometers, respectively.

Tables 1.1 and 1.2 contain the two main noise terms that affect the gyroscopes (that are Angular Random Walk and Bias Instability), and the accelerometers (that are Velocity Random Walk and, again, the Bias Instability). The percentage between the brackets represents the level of confidence of that noise coefficient value.

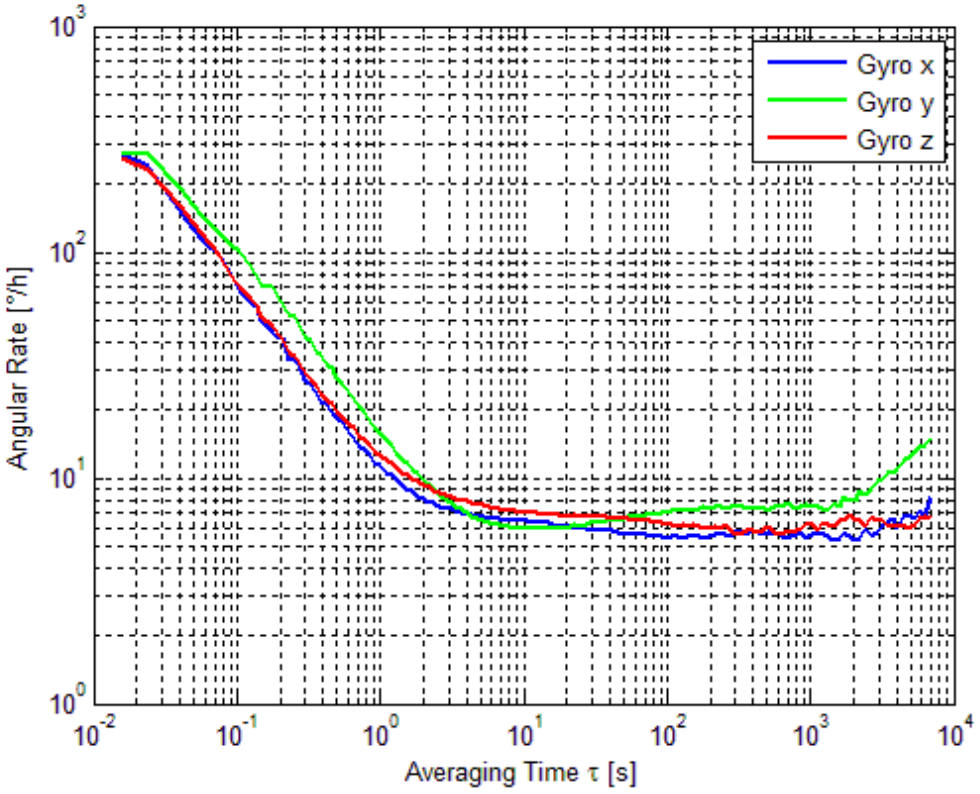

Figure 1.1 – Gyroscopes Allan Variance Plot

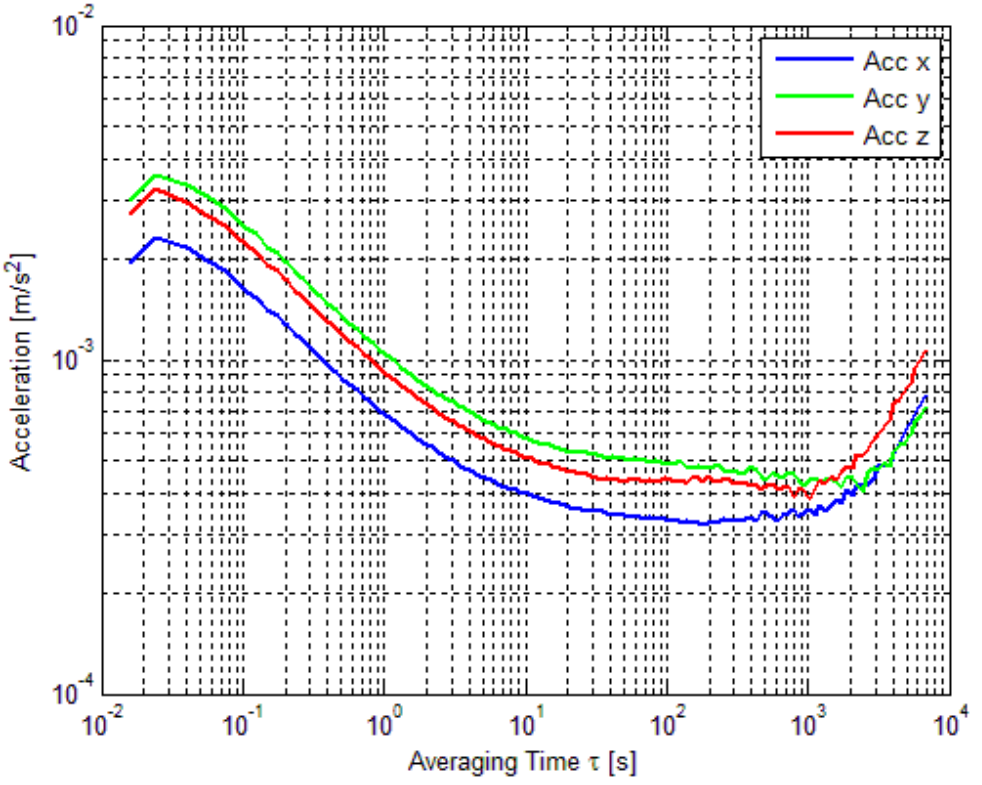

Figure 1.2 – Accelerometers Allan Variance Plot

	ARW $(°/\sqrt{h})$	Bias Instability $(°/h)$
Gyro X	~ 0.2 (99.7%)	~ 8 (99.1 %)
Gyro Y	~ 0.2 (99.6%)	~ 8 (99.1%)
Gyro Z	~ 0.2 (99.7%)	~ 8 (94.8%)

Table 1.1 – Main Noise Parameters for Gyroscopes

	VRW $(m/s\sqrt{h})$	Bias Instability (m/sh)
Acc X	~ 0.04 (99.7%)	~ 2 (96.9%)
Acc Y	~ 0.05 (99.7%)	~ 2 (94.0%)
Acc Z	~ 0.05 (99.7%)	~ 2 (95.4%)

Table 1.2 – Main Noise Parameters for Accelerometers

These values are typical of MEMS industrial-grade inertial sensors.

The subsequent design choice has regarded the SW solution. Figure 1.3 represents the block diagram of the INS model adopted.

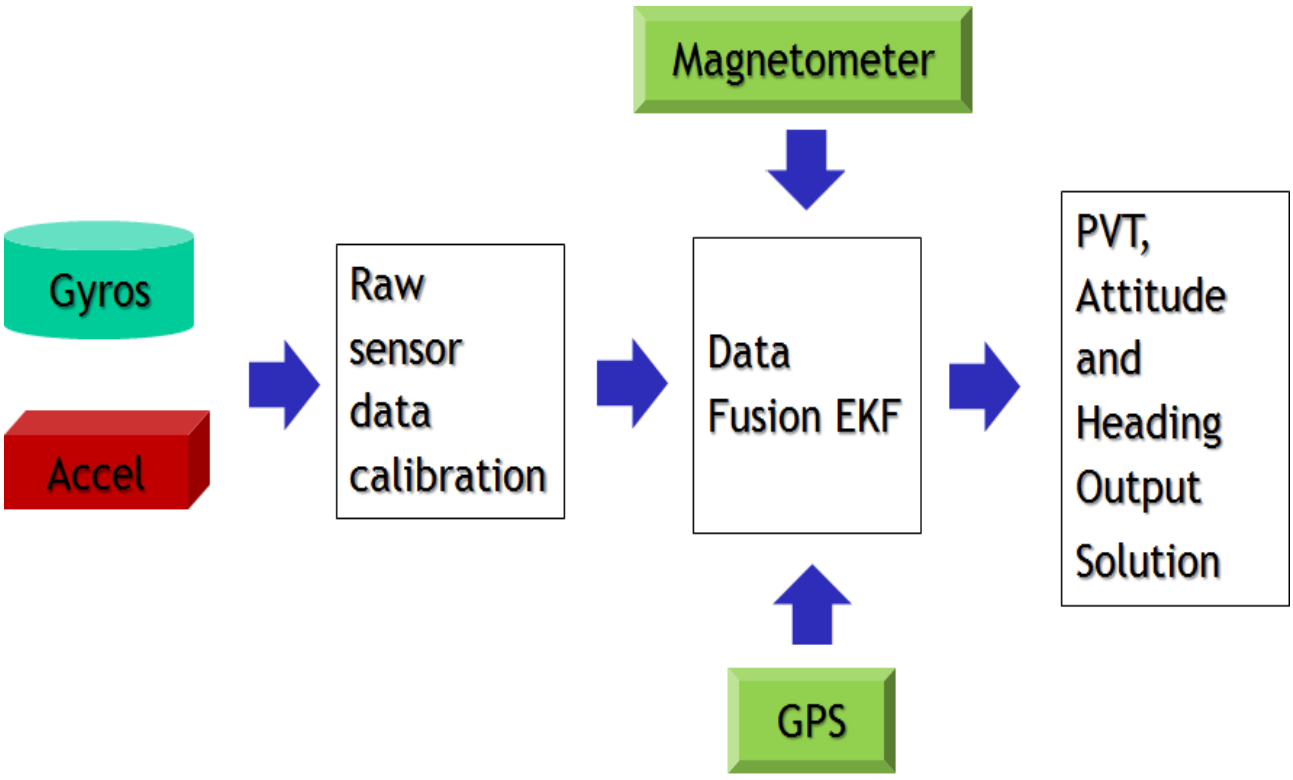

Figure 1.3 – INS Block Diagram Model

From the model it is possible to recognize the presence of a GNSS receiver and of a magnetometer. These devices are usually used as reference in the INS initialization phase and as aiding during the INS navigation phase in order to bound the drift of the navigation solution. It is also possible to note that is implemented a compensation of the inertial sensors' raw data (applying a set of calibration coefficients that are evaluated after an indoor calibration procedure) in order to remove the deterministic errors typical of MEMS inertial sensors. In order to optimally combine all the above mentioned systems, an applied optimal estimation tool like Kalman filtering (KF) [7] is usually used to fuse IMU, GPS and Magnetometer data in real-time.
Figure 1.4 shows the final system, developed at the end of this research activity, the AX1-GNS3 system.

Figure 1.4 – AX1-GNS3 System

It is formed by three physical separate units (the AX1-ATU, the AX1-MSU and the AXA-GPS) communicating through dedicated connections (see Figure 1.5):

- AX1-ATU: it is an attitude sensor based on MEMS technology that is directly derived from the already approved Axitude AX1-[] family (EASA.21O.931). The AX1-ATU device includes an Inertial Sensor Assembly (ISA), containing three orthogonally mounted angular rate sensors and three orthogonally

mounted accelerometers. The inertial sensors are based on MEMS technology and they are mounted in a strap-down configuration with input axes aligned to the object body reference system.

- AX1-MSU: it is a remote magnetic sensing unit used to perform heading sensing by evaluating the direction in the local level frame of the Earth Magnetic Field vector. This function is accomplished by means of a three-axis Magneto-resistive Sensor Assembly (MSA) housed in a case compatible with existing fluxgate sensor and a processing unit that basically elaborates the magnetic measurements.
- AXA-GPS: it is a OEM satellite sensor system that receives and utilizes the signals coming from GPS satellite constellation and Satellite-Based Augmentation System (SBAS), such as WAAS, EGNOS, MSAS and GAGAN. The GPS receiver is able to detect and exclude failed satellites using the Receiver Autonomous Integrity Monitoring (RAIM) algorithm. The AXA-GPS communicates with the AX1-ATU through a bi-directional serial communication link and it provides the time mark synchronization to GPS time through a digital signal.

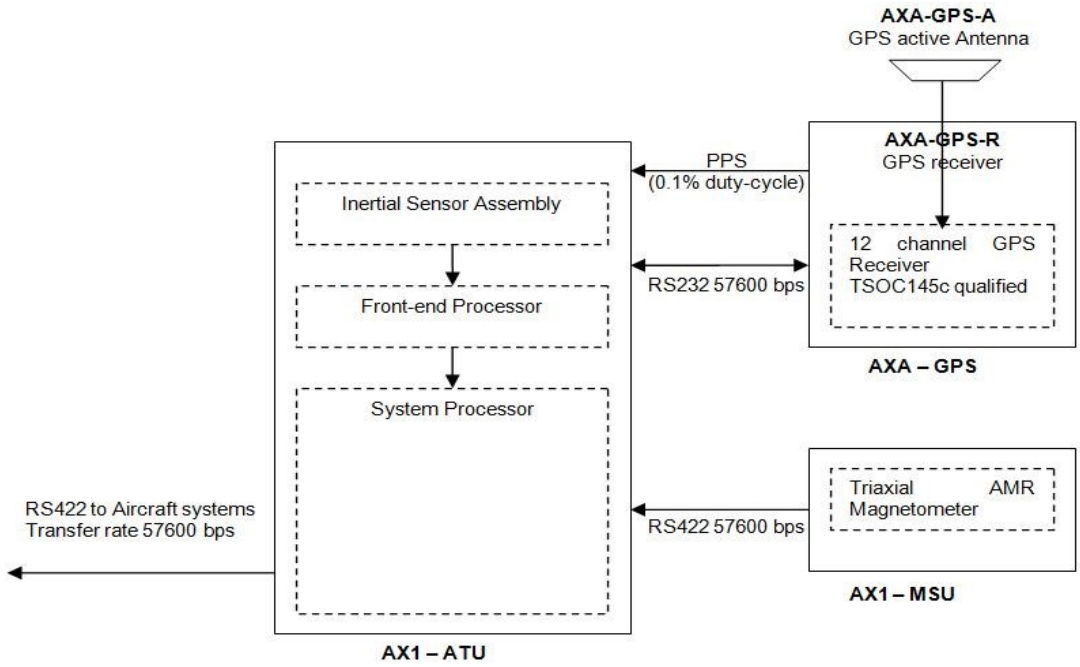

Figure 1.5 – AX1-GNS3 separated units and their connections

A three-steps testing strategy has been adopted in order to achieve an high attitude determination measurement accuracy suitable to comply with UAV applications' requirements:

1. Laboratory Testing for raw sensor data calibration in order to evaluate and compensate the accelerations and angular rates measurement deterministic errors;
2. Van Testing for EKF tuning and SW validation;
3. Flight Testing for in-flight performance evaluation.

This testing strategy will be exposed in more details in the next sections.

1.3 Lab Testing

The major error sources for inertial navigation systems are due to gyro and accelerometer inertial sensor imperfections, incorrect navigation system initialization, and imperfections in the gravity model used in the computations. But, in nearly all integrated navigation systems and in particular for MEMS sensors, the largest errors are due to the inertial sensors. Whether the inertial sensor error is caused by internal mechanical imperfections, electronics errors, or other sources, the effect is to cause errors in the indicated outputs of these devices. Typically, the uncertainty of measurement results is due to bias and scale factor errors and their dependence with operating temperature, sensitivity's axis misalignment due to fabrication and sensors' assembly, non-linearity, hysteresis, shock, vibration and acceleration unwanted dependencies, noise with specific spectral density distribution, aging.

MEMS inertial sensors performances can be greatly improved through static and dynamic tests on a turntable and thermal tests in a climatic chamber in order to compensate their deterministic sources of errors. Figures 1.6 and 1.7 depict the AX1-ATU mounted on a turntable used to execute static and dynamic tests in the Axitude laboratory in two different positions. Figure 1.8 shows the climatic chamber utilized

to perform thermal tests and Figure 1.9 depicts the AX1-ATU and the AX1-MSU at rest in the climatic chamber. As explained before, an Allan Variance Analysis has also been conducted to stochastically characterize the sensors' random processes.

Figure 1.6 – AX1-ATU mounted on the turntable

Figure 1.7 – AX1-ATU mounted on the turntable (other position)

Figure 1.8 – Climatic Chamber in the Axitude Laboratory

Figure 1.9 – AX1-ATU and AX1-MSU in the climatic chamber

Experimental results show residuals errors less than 17 mg for the accelerometers and less than the 0.7% of the gyroscopes full scale value for the gyros. Figure 1.10 shows the compensated angular rates compared with the turntable angular rates, taken as reference.

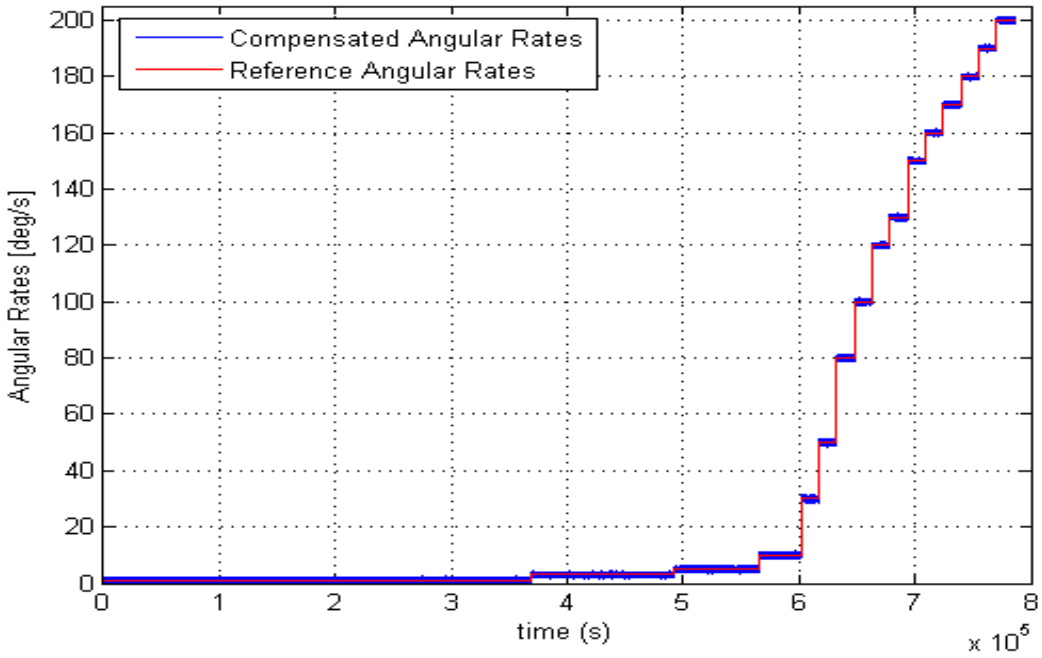

Figure 1.10 – Compensated Angular Rates vs Reference Angular Rates

Nevertheless, also if MEMS accuracy can be greatly improved through a calibration procedure, it becomes more and more challenging to verify navigation performance of integrated navigation systems. This is a complex task due to several critical issues such as:

1. The intrinsic dynamical and statistical models of sensor and systems;
2. The selected data fusion strategy, that is usually based on an Extended Kalman Filter due to nonlinearities in sensor and dynamics models;
3. The typical and the worst case maneuvers that must be performed to determine a trustworthy dynamical model of the aircraft where the system is installed.

Thus, numerical and indoor testing is not considered significant in most cases, since nonlinear dynamical models, non-Gaussian sensor error models, and the wide range of operative conditions cannot be simulated with the required fidelity level. Consequently, field testing is the best option to validate an integrated navigation system [8]-[9].

1.4 Van Testing

The AX1-GNS3 testing activities included a Van Test to be performed during November 2014 in the surroundings of Giugliano in Campania (NA), Italy.

The Van Test was performed to satisfy the following purposes:

1. to give a first demonstration of the Axitude AX1-GNS3 system capabilities;
2. to allow a tuning of the EKF;
3. to validate the embedded SW.

In the following sub-section will be exposed a comparison between attitude, velocity and position provided by the Axitude system and the same quantities measured in the same dynamic conditions by nominally more accurate systems, taken as reference.

1.4.1 Van Test Setup

The following Figures 1.11 and 1.12 show the Van Test setup.

Figure 1.11 – Van Test Setup

Figure 1.12 – Van Test Setup, zoom on the various devices

From these figures it is possible to recognize the AX1-GNS3 system, configured to work as depicted in Figure 1.13.

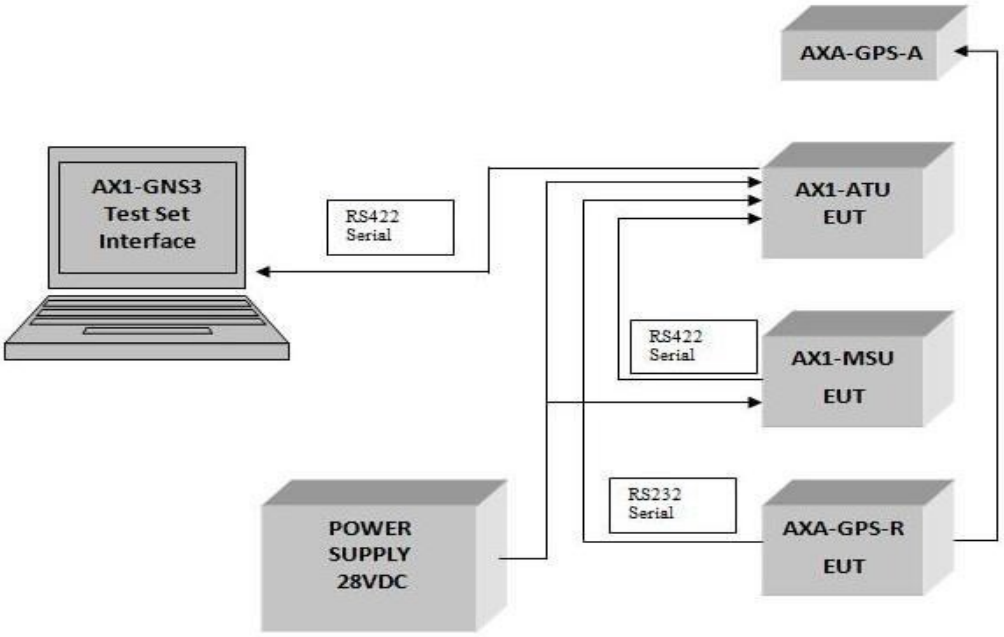

Figure 1.13 – AX1-GNS3 test configuration block diagram

The INS/GPS iNAV-FMS [10] of the *iMAR GmbH* Company, procured by the CIRA's LGNC laboratory, has been selected as the reference inertial system during the Flight Test.

The iNAV-FMS is an inertial measurement unit with Fiber Optic Gyros (FOGs). It is an integrated system composed by the following units:

- three-axis FOG gyros;
- three-axis piezoceramic accelerometers;
- an integrated twelve channel GPS receiver unit tuned on L1 frequency;
- three-axis integrated digital magnetometer.

In order to obtain the best performance in terms of accuracy, the heading computed by the iNAV-FMS reference system will be aligned with the "true heading" through the execution of an in-flight "8" maneuver.

The operating features of the system iNAV-FMS are depicted in the table below:

Parameter	Value
Gyros measurement range	± 500 °/s
Accelerometers measurement range	±10 g
Gyros resolution	0.1 arcsec
Accelerometers resolution	< 100 µg
Gyros bandwidth	> 200 Hz
Accelerometers bandwidth	> 70 Hz
Non-linearity	< 0.03 %
Scale factor error	< 0.03 %
Gyros bias	< 0.5°/hr
Roll and pitch accuracy	< 0.2 deg (no aiding) < 0.1 deg (with GPS aiding)
Heading accuracy (True heading alignment is performed in flight)	< 0.15 deg (with GPS aiding)
Alignment time (True heading alignment is performed in flight)	< 60 sec
Output rate	1..400Hz
Digital interfaces	RS-232/RS-422/Ethernet/CAN
Operating temperature	-40..+70°C
Weight	4.1 Kg
Size	270 x 145 x 132 mm
Input supply voltage	10-34 VDC

Table 1.3 – iMAR iNAV-FMS main features

The iNAV-FMS device was configured to provide on a RS-232 interface, at a frequency of 50 Hz, at least the following parameters:

Parameter
Measurement reference time
Roll angle
Pitch angle
Heading angle
Angular rates
Linear accelerations

Table 1.4 – iMAR iNAV-FMS output

Figure 1.14 – iMAR iNAV-FMS

A GPS-RTK receiver from the Trimble Company [11] was configured to provide, at the frequency of 5 Hz, PVT (Position, Velocity and Time) measurements taken as reference for the AX1-GNS3 system PVT solution. Its corresponding antenna was placed near the AXA-GPS antenna and receiver.

A ground-based antenna was placed near the test area at a very-well known position, on the roof of the GMA/Axitude Company, as shown in the figures below.

Figure 1.15 – Ground-based antenna of GPS-RTK

Figure 1.16 – Ground-based antenna of GPS-RTK (other point of view)

1.4.2 Van Test: Data Charts

The present sub-section shows some graphical results of the Van Test. In particular, the graphs contain:

- The ground path provided by the GPS-RTK system;
- A roll/pitch solution comparison between the AX1-GNS3 and the iNAV-FMS reference system;
- A comparison between the linear velocity and the geodetic position as measured by the AX1-GNS3 and the GPS-RTK devices.

In the following figure (realized through *Google Earth*^{TM}) the "*Ground path*" obtained through the geodetic positions given by the GPS-RTK is shown. The green balloon in the figure indicates the position of the GPS-RTK ground-based antenna placed on the roof of the GMA Company.

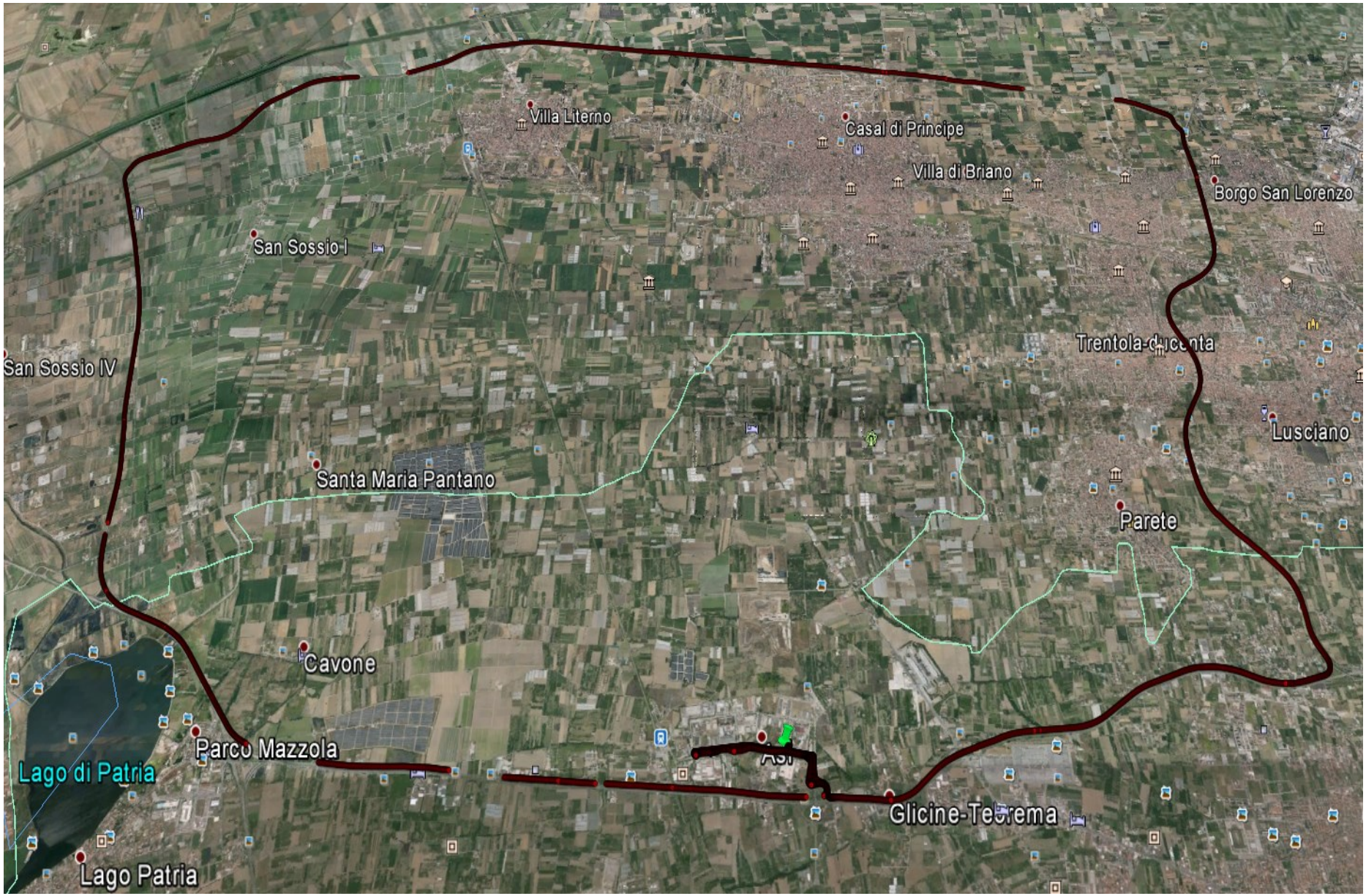

Figure 1.17 – Van Test “Ground Path”

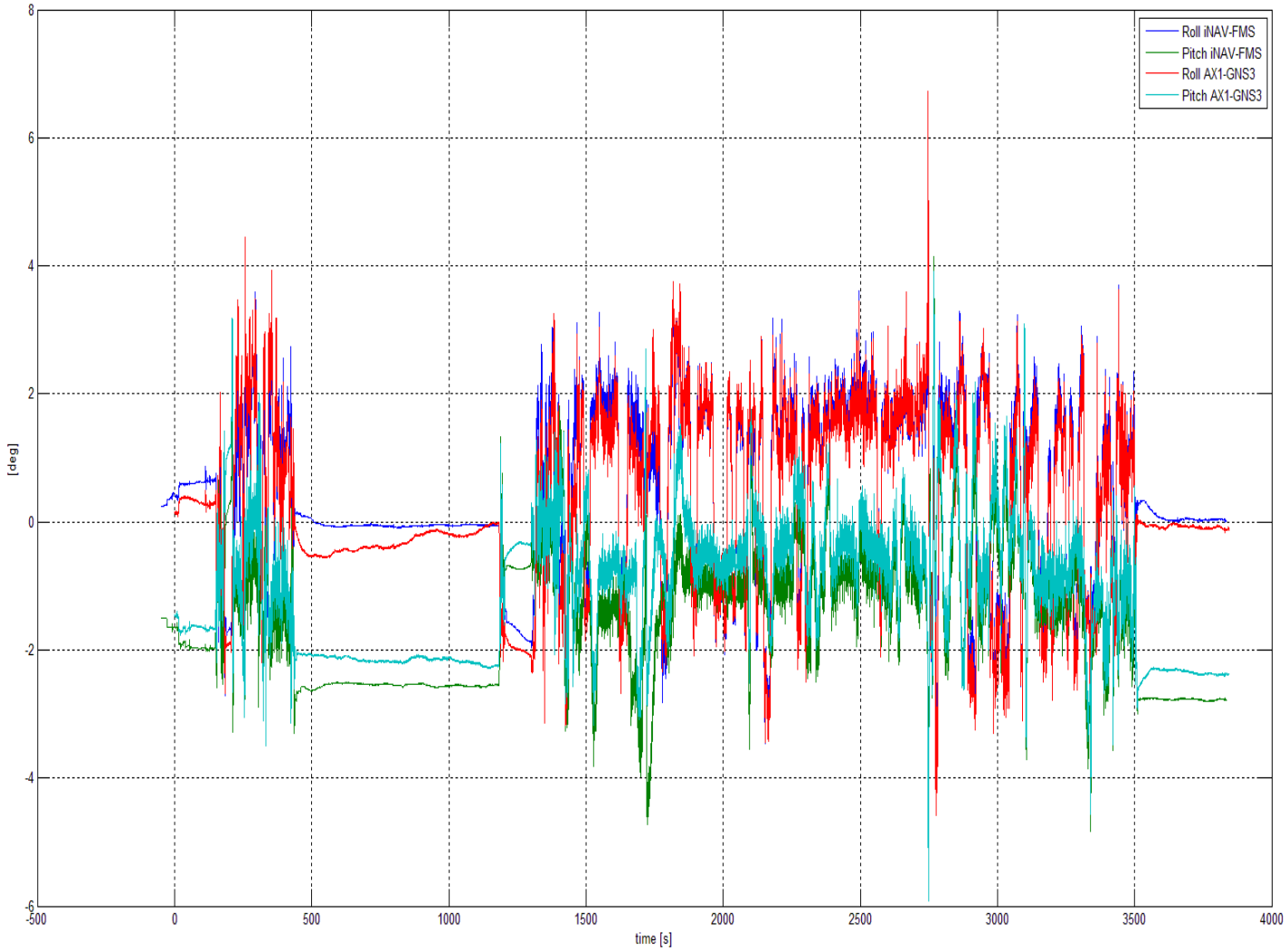

Figure 1.18 – Roll and Pitch angles comparison between AX1-GNS3 system and iNAV-FMS reference system

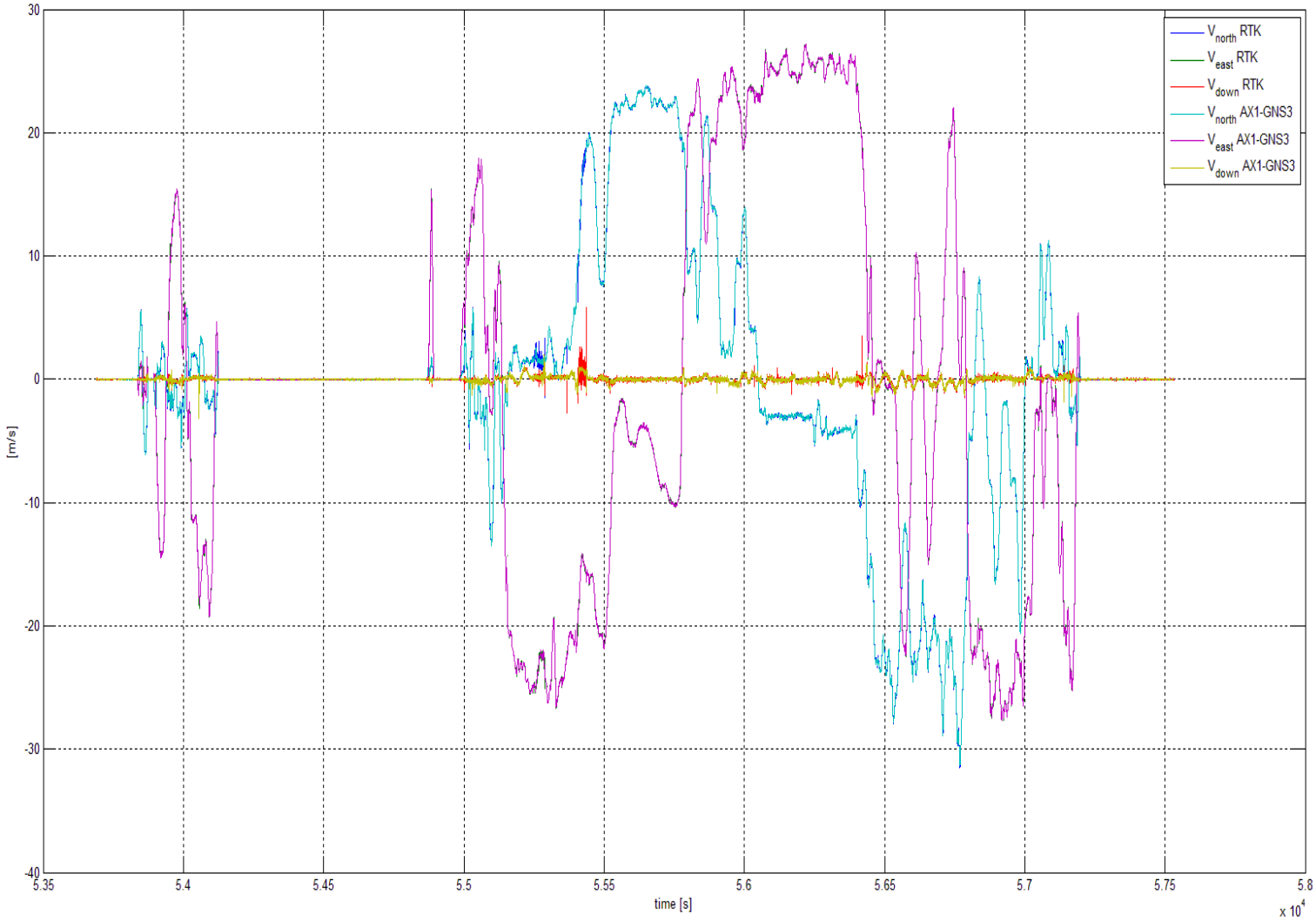

Figure 1.19 – NED Velocity comparison between AX1-GNS3 system and GPS-RTK reference system

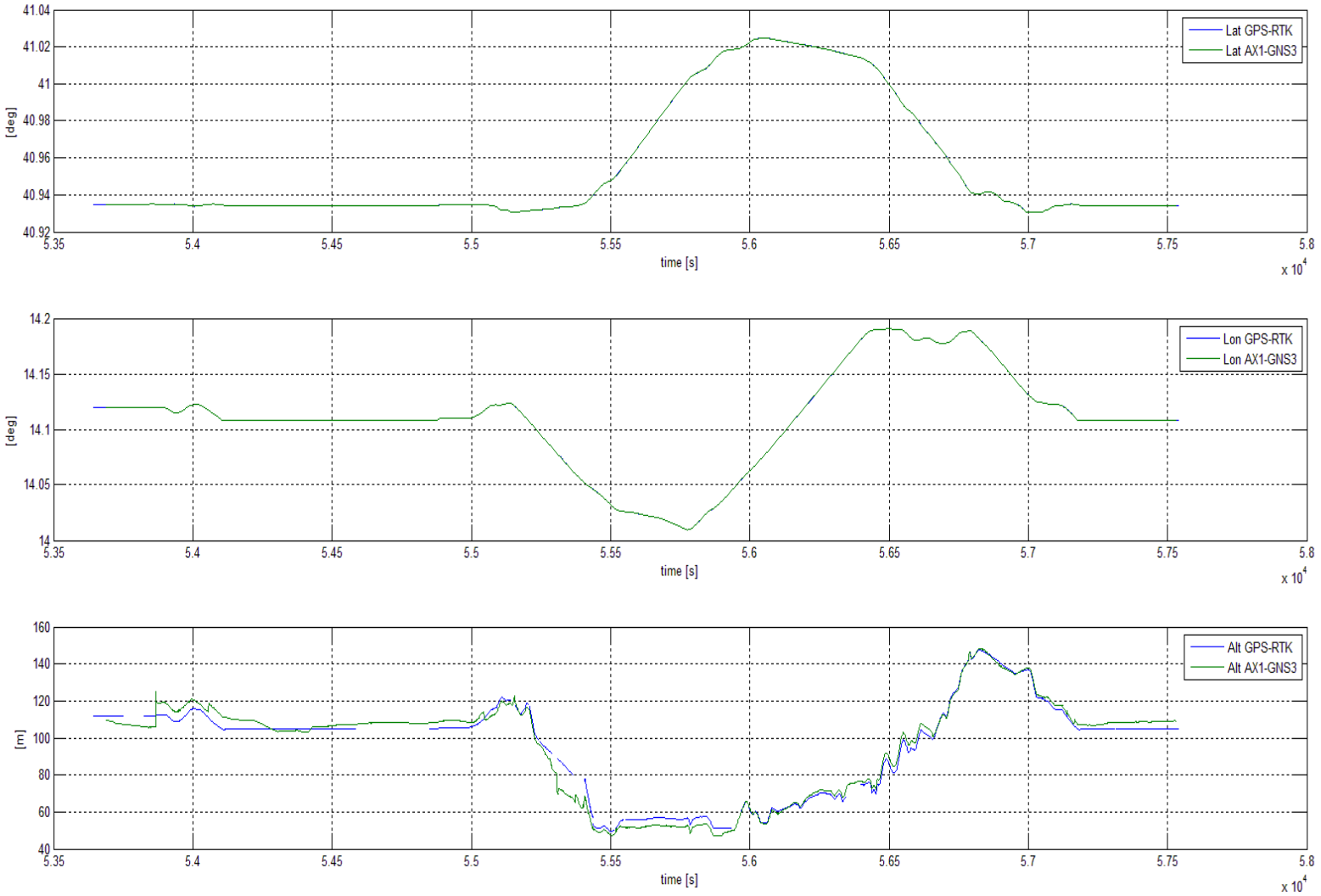

Figure 1.20 – LLH Geodetic Position comparison between AX1-GNS3 system and GPS-RTK reference system

Many of these outputs, like

- roll and pitch angles;
- V down;
- WGS-84 Altitude.

are not plotted because of a particular interest for a performance evaluation in a Van Test, but because they are helpful in the optics to satisfy the Van Test purposes, that are:

1. to give a first demonstration of the Axitude AX1-GNS3 system capabilities;
2. to allow a tuning of the EKF;
3. to validate the embedded SW.

These purposes have been fully satisfied by this Van test activity.

1.5 Flight Testing Activities

The AX1-GNS3 testing activities included a Flight Test to be performed during December 2014 in the surroundings of Castelvolturno (NA), Italy.

Aim of this Flight Test was to give a first demonstration of the Axitude AX1-GNS3 overall in-flight capabilities through a comparison between attitude, velocity and position provided by the Axitude system and the same quantities measured in the same dynamic conditions by nominally more accurate systems, taken as reference.

The Flight Test was carried out on the Tecnam P-92 Echo aircraft. The following figures show the Flight Test setup.

Figure 1.21 – Tecnam P-92 Echo aircraft

1.5.1 Flight Test Setup

In the Figures 1.22-1.23, it is possible to recognize the AX1-GNS3 system configured to work as explained in Figure 1.13.

Figure 1.22 – Flight Test Setup

Figure 1.23 – Flight Test Setup, other point of view

Also in the same figures it is possible to recognize the iNAV-FMS and the GPS-RTK reference systems already adopted during the Van Test. The GPS-RTK receiver and antenna are depicted in Figure 1.24 and 1.25. In the latter figure it is possible to note that the GPS-RTK antenna is placed close to the AXA-GPS antenna.

Figure 1.24 – GPS-RTK Rover Receiver

Figure 1.25 – GPS-RTK Rover Antenna

A ground-based antenna was placed near the test area at a very-well known position as shown in the Figure 1.26 below.

Figure 1.26 – Ground-based antenna of GPS-RTK

Other test equipment comprises:

- **Mounting Fixtures.** A dedicated interface fixture has been posed inside the aircraft in order to fix the Equipment Under Test (EUT) components and the reference system devices.
- **Three GPS antennas** to be used with AX1-GNS3, iNAV-FMS and the GPS-RTK "rover" receiver.
- **Connection Cables**. For this testing session purposes the AX1-GNS3 was equipped with a series of dedicated cables similar to ones designed for the installation. Each of them was used to connect the AX1-GNS3 components between them and with the communication port of the interface PC (the AX1-ATU).
- A couple of **data logger PC**: They were standard Windows based (2000, XP or Seven) personal computers equipped with either a RS-422 and a RS-232 interface and a graphic card with OpenGL support, suitable for running software environments described below;
- **GNS3 Saver Software** Where needed this software suite can be also replaced with a command line version of the interface support software that receive the same data from EUT and produce the same outputs on log files.

1.5.2 Flight Test: Data Plots

The purpose of the Flight Test was to perform a series of maneuvers in manual control mode or even automatic, acquiring the measurements of the various systems installed on board the aircraft in order to evaluate the performance of the AX1-GNS3 system under different operating conditions of attitude, acceleration, velocity and geodetic position.

The present sub-section shows the graphical results of the Flight Test. In particular, the graphs contain:

- An attitude solution comparison between the AX1-GNS3 and the iNAV-FMS reference system;
- Angular rates and linear accelerations provided by the AX1-GNS3 product;
- A comparison between the linear velocity and the geodetic position as measured by the AX1-GNS3 and the GPS-RTK devices.

In more details, this subsection is structured as here reported:

- Initially the ground path, the attitude angles, the linear accelerations, the angular rates, the linear velocities and the geodetic positions as provided by the AX1-GNS3 system are depicted;
- Then a comparison between the measurements of the attitude angles realized by the AX1-GNS3 and its reference system (the iMAR iNAV-FMS) is shown; moreover, the deviations of roll, pitch and true heading measurements are reported;
- In the following sub-section, the linear velocities as measured by the AX1-GNS3 and the GPS-RTK devices are reported. Besides, the deviations between the AX1-GNS3 and the GPS-RTK measurements are shown.
- Finally the geodetic positions as measured by the AX1-GNS3 and the GPS-RTK systems are analyzed in the same manner as explained in the previous sub-section for the linear velocities.

The Flight Test lasted about 45 minutes. In the following figure (realized through *Google Earth*^{TM}) the "*Ground path*" obtained through the geodetic positions given by the AX1-GNS3 is shown.

Figure 1.27 – Flight Test "Ground Path"

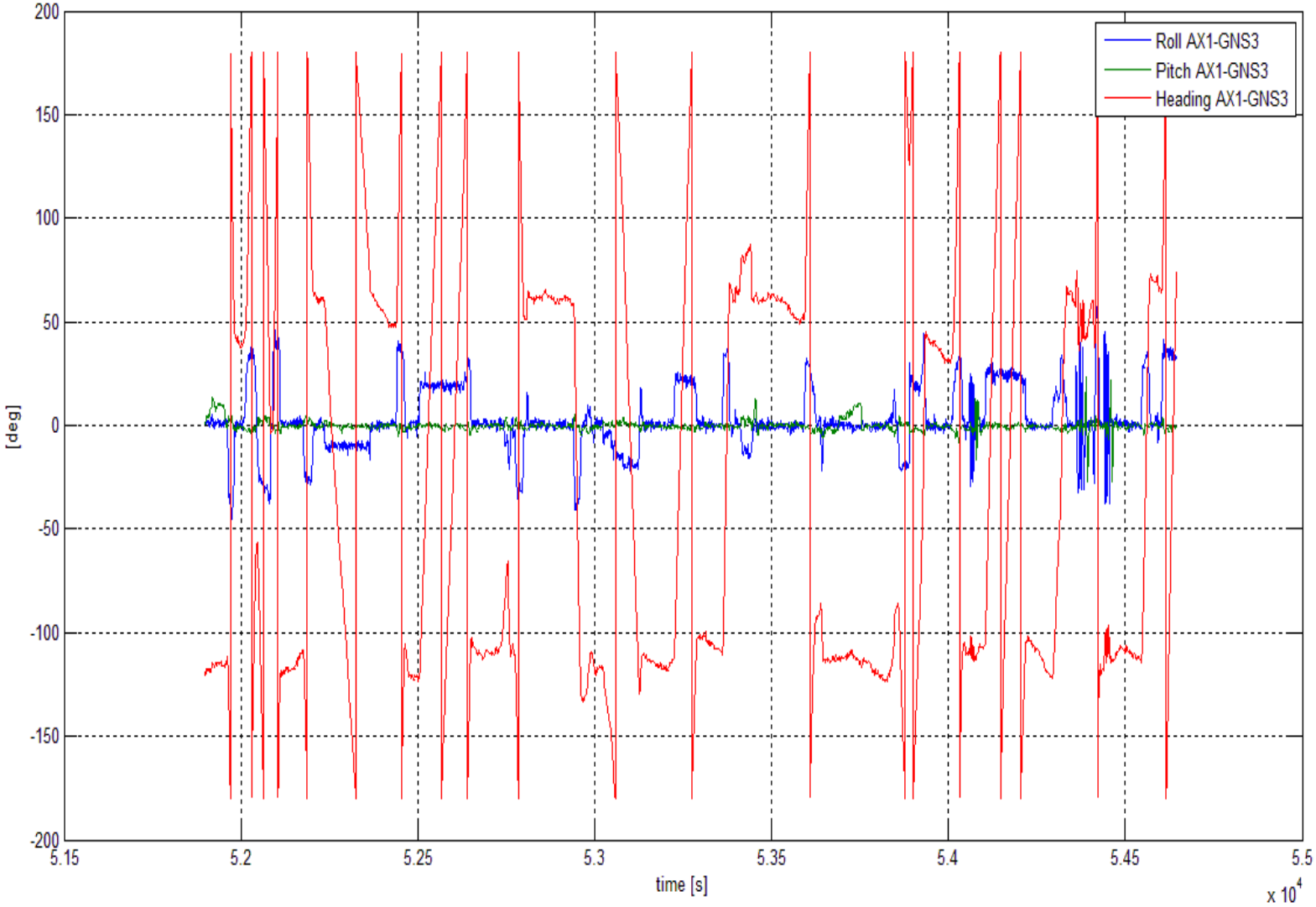

Figure 1.28 – Roll, Pitch and Heading angles computed by the AX1-GNS3 system

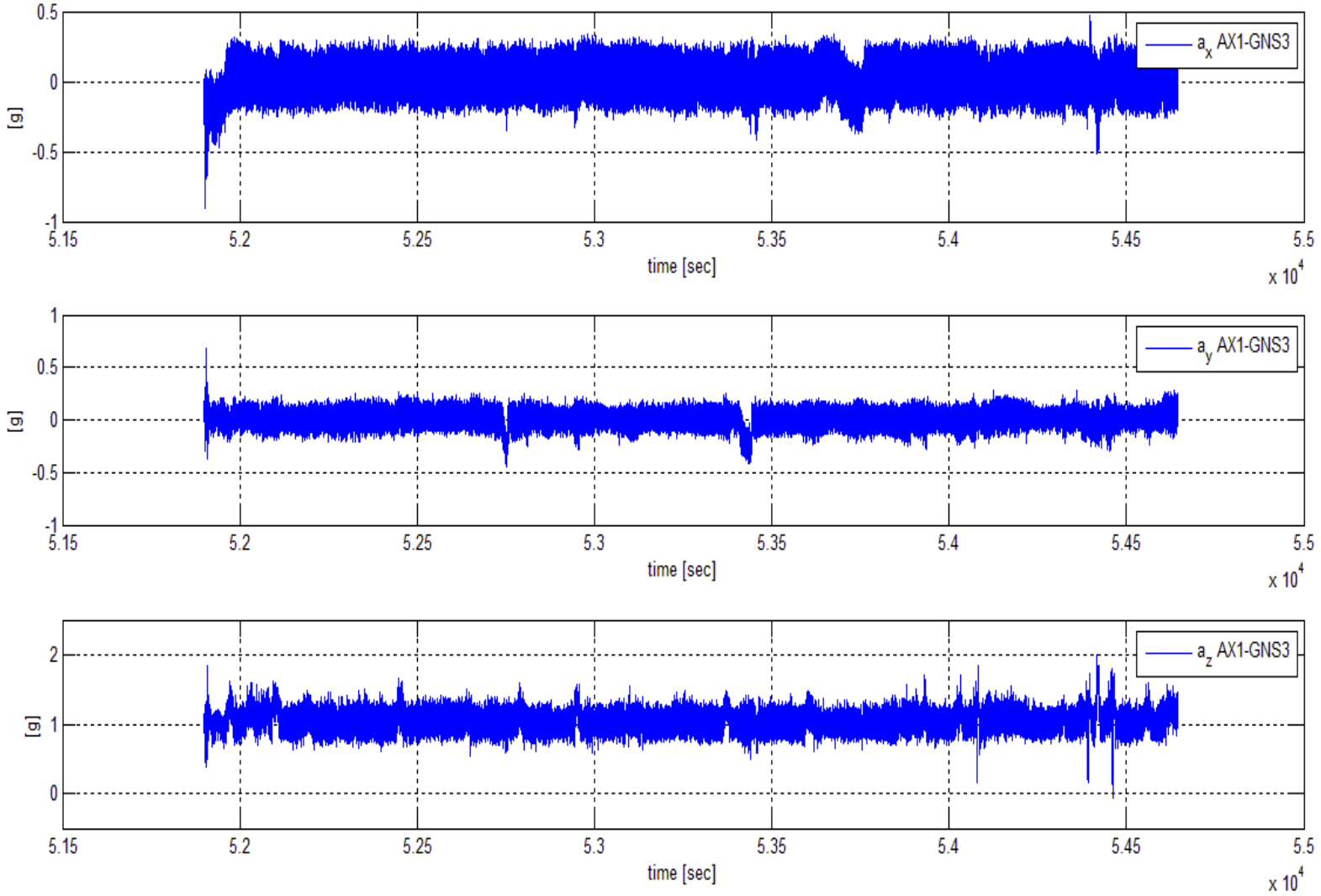

Figure 1.29 – Body accelerations computed by the AX1-GNS3 system

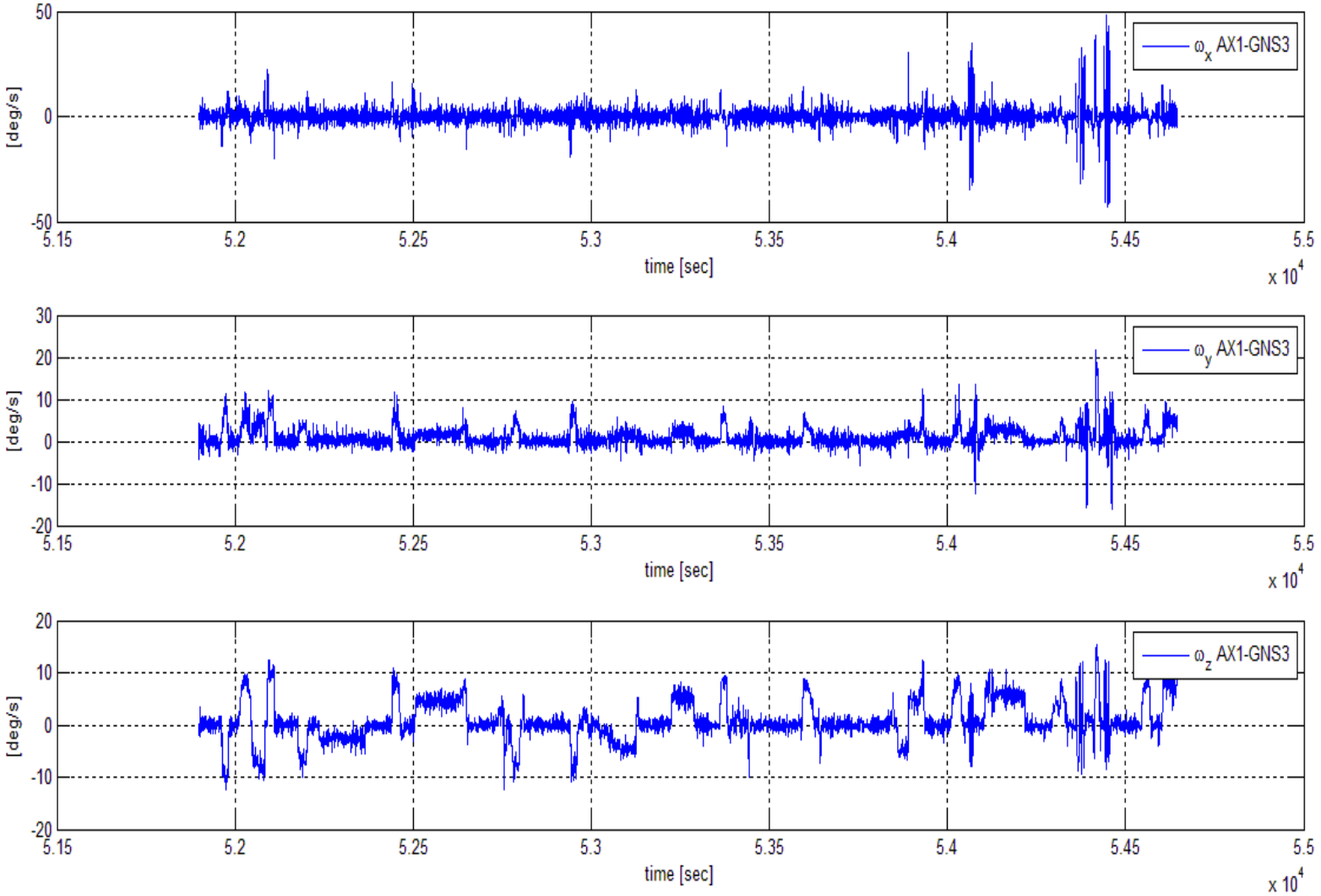

Figure 1.30 – Body angular rates computed by the AX1-GNS3 system

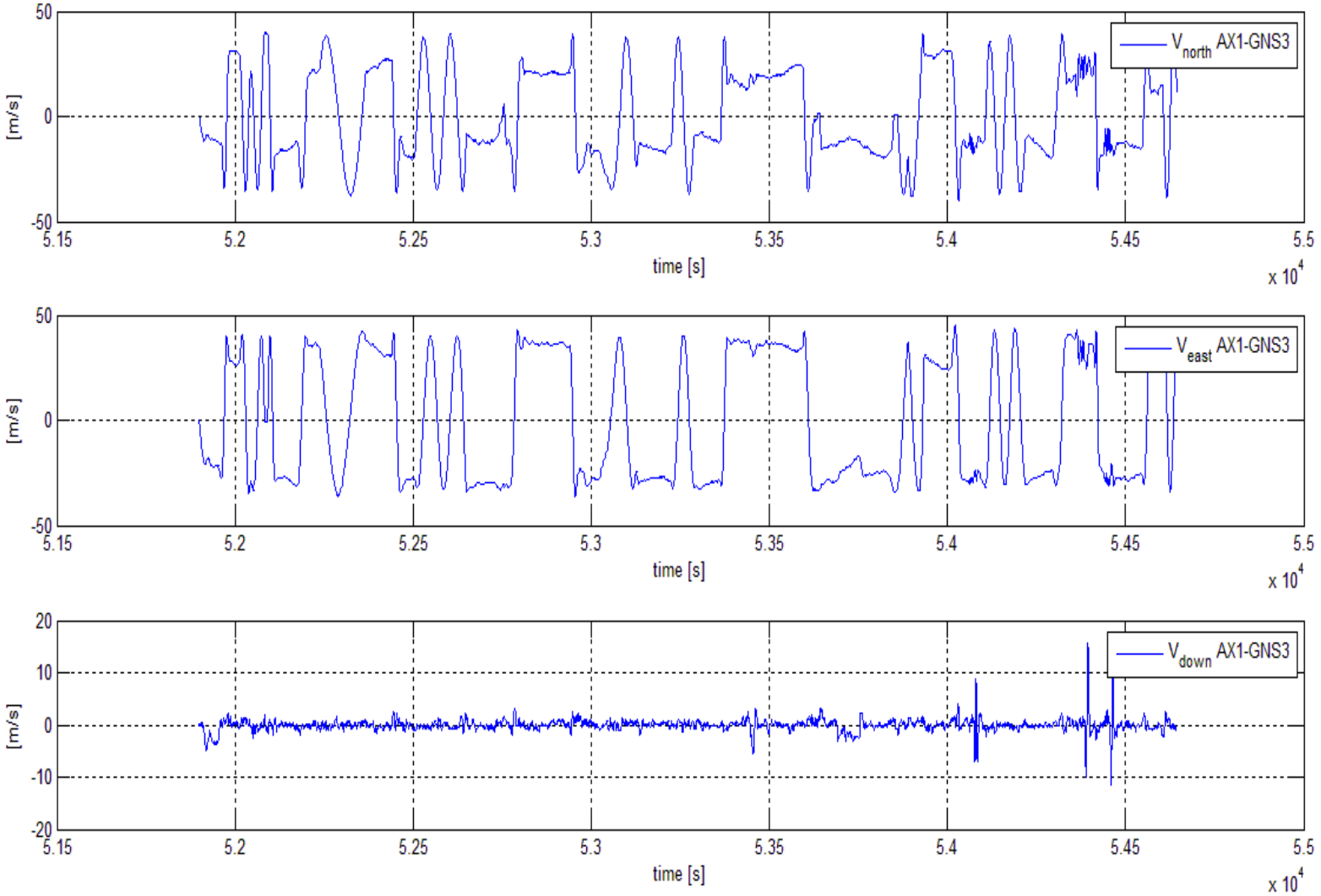

Figure 1.31 – NED linear velocities computed by the AX1-GNS3 system

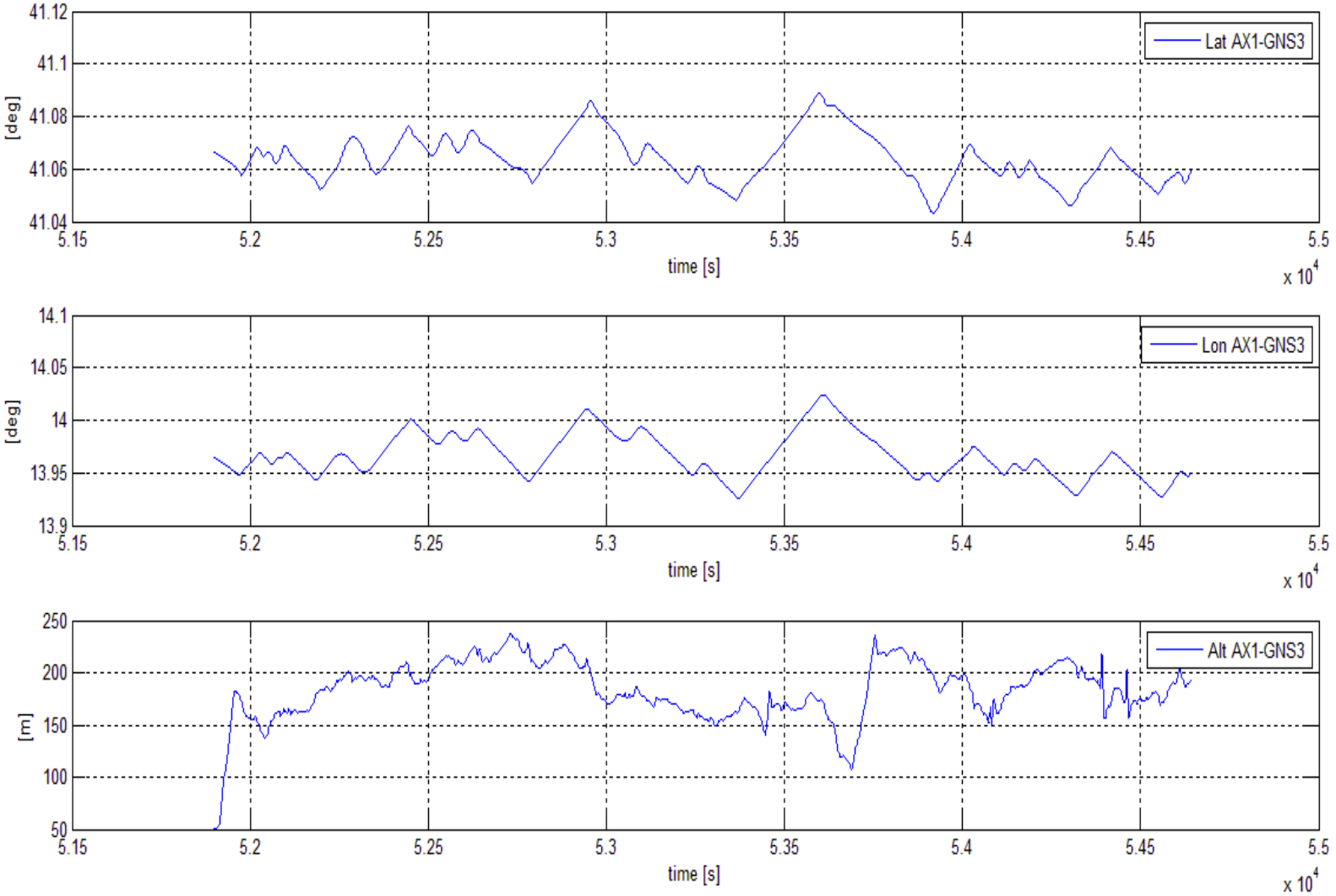

Figure 1.32 – Geodetic positions computed by the AX1-GNS3 system

1.5.3 Flight Test: Attitude Comparison

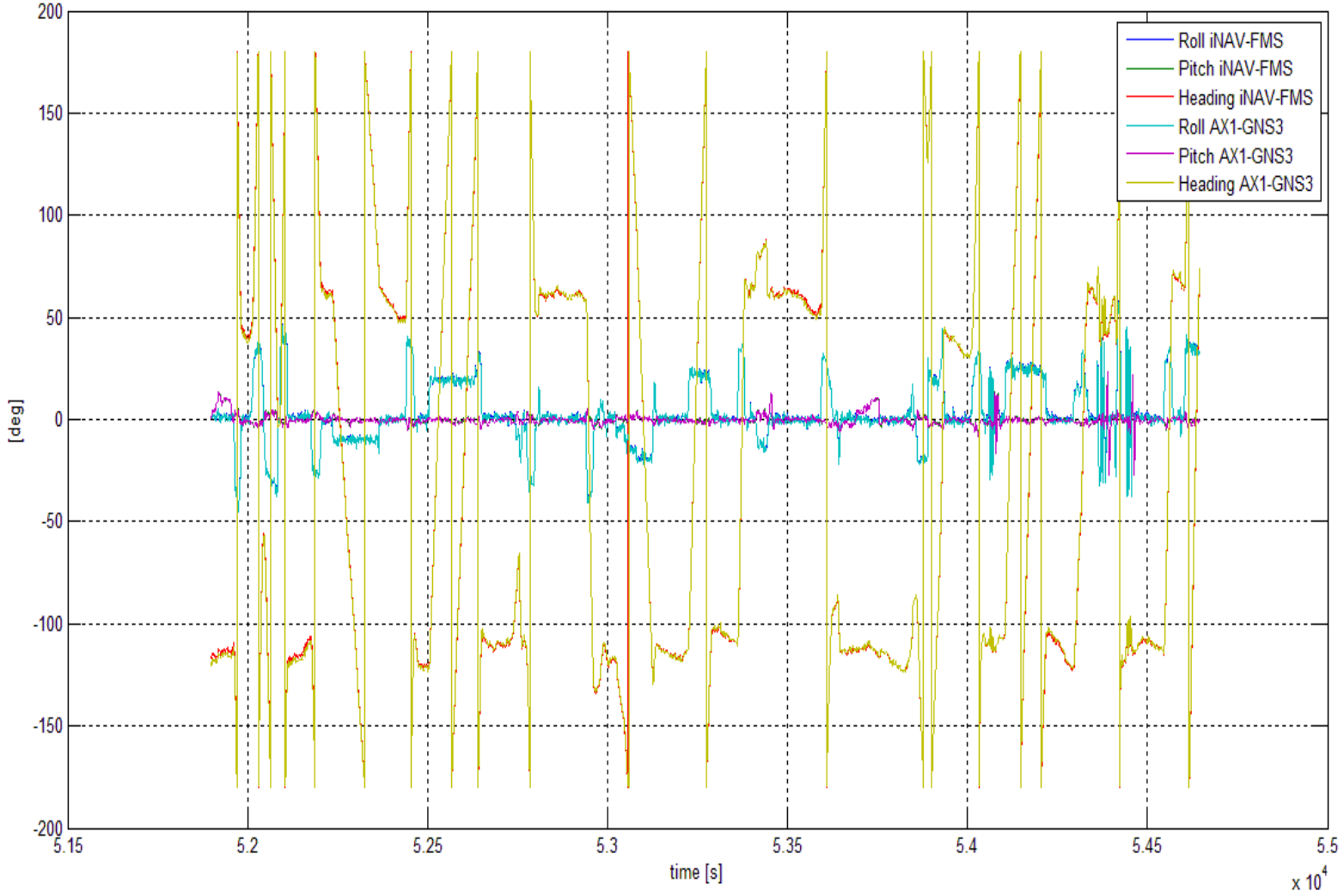

Figure 1.33 – Roll, Pitch and True Heading angles comparison

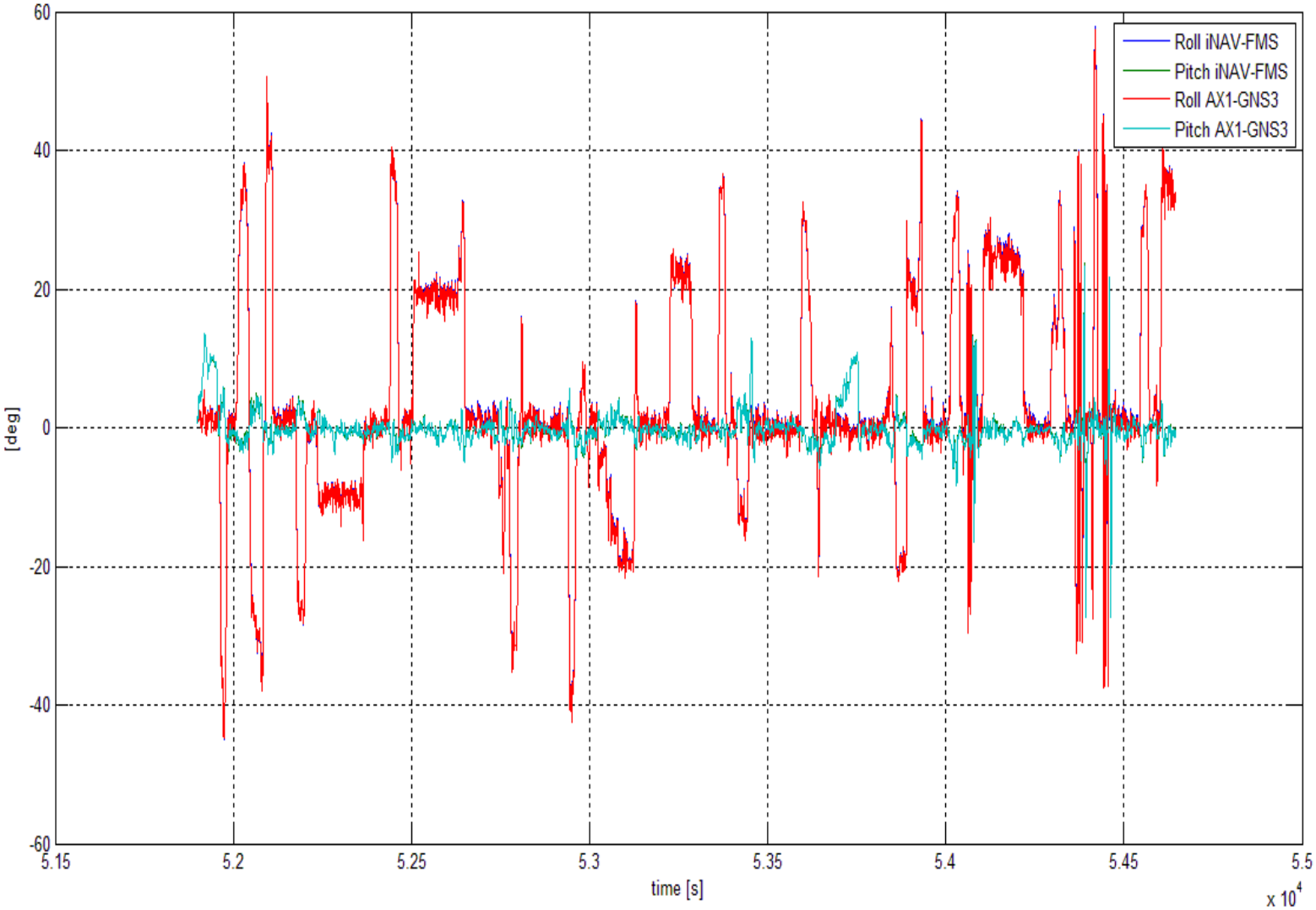

Figure 1.34 – Roll and Pitch angles comparison

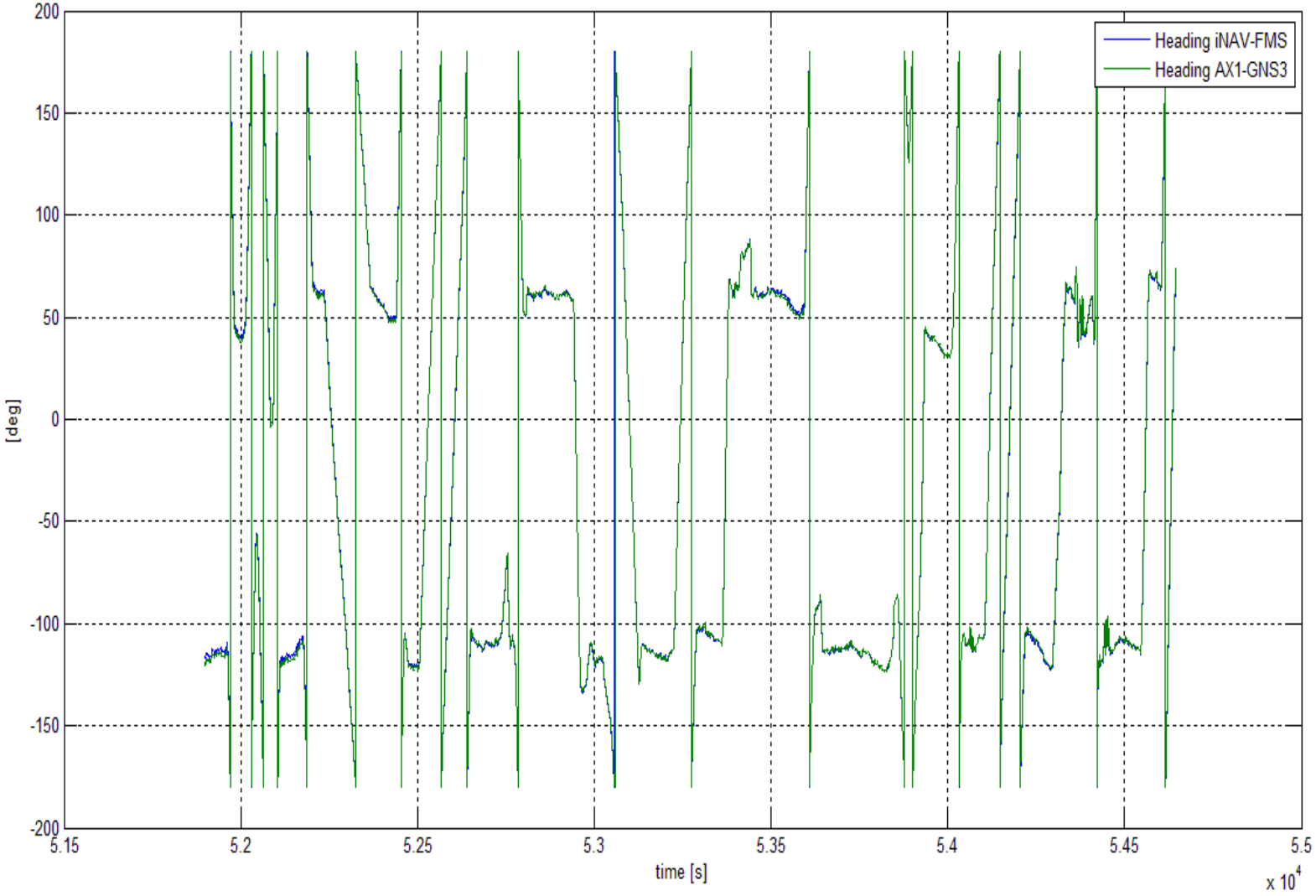

Figure 1.35 – True Heading angle comparison

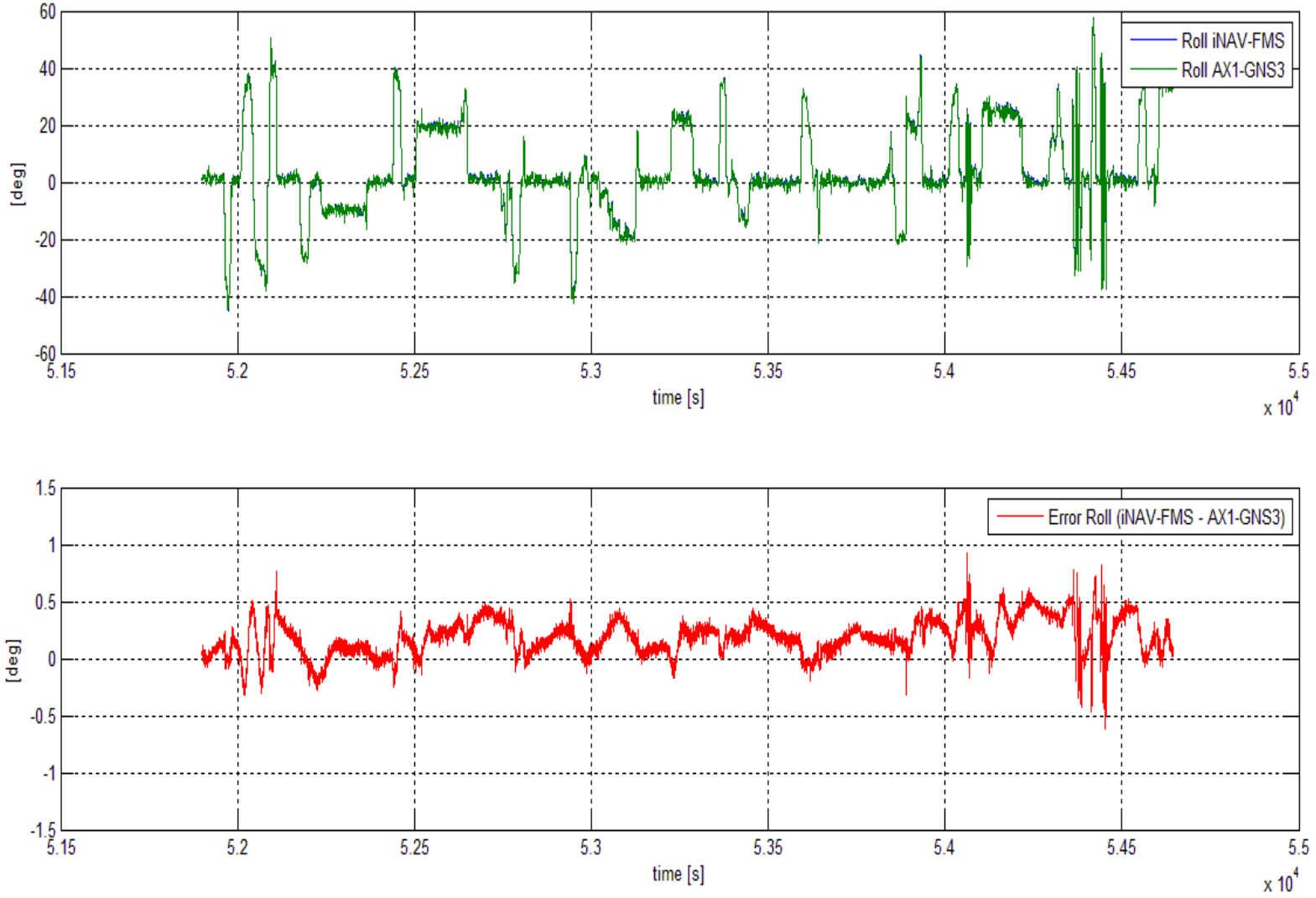

Figure 1.36 – Roll angle deviation

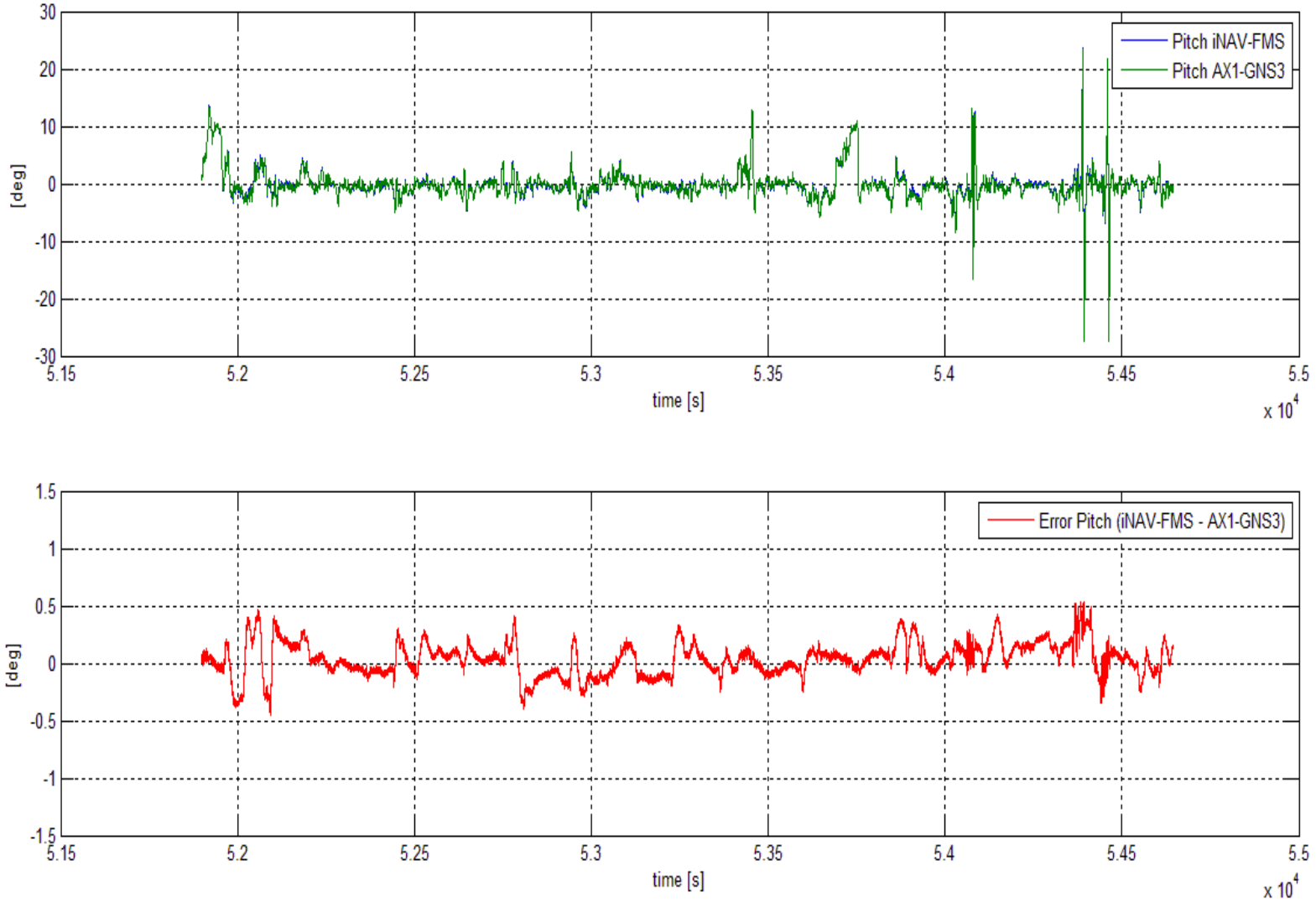

Figure 1.37 – Pitch angle deviation

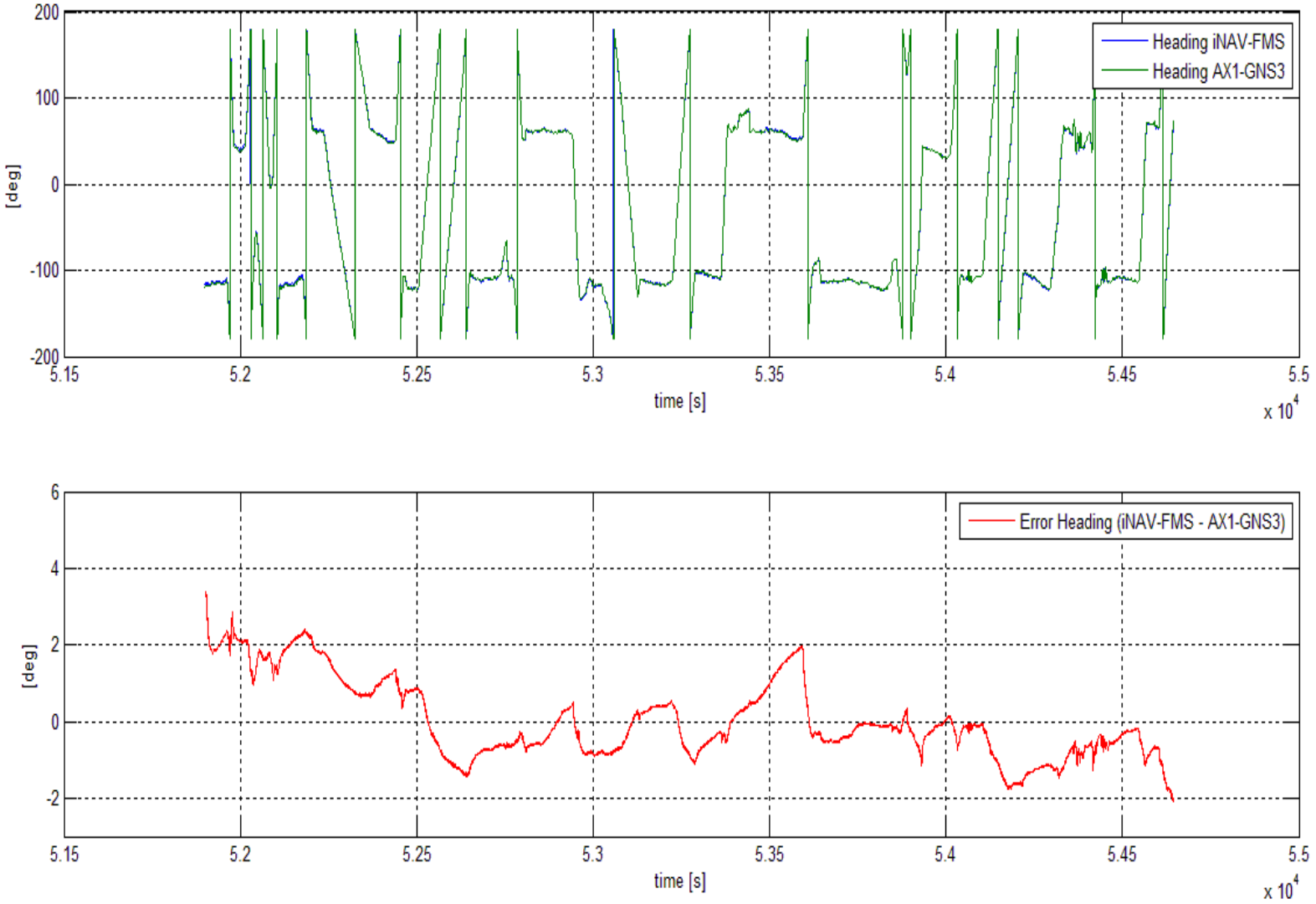

Figure 1.38 – True Heading angle deviation after eight-shape maneuver

1.5.4 Flight Test: Linear Velocity Comparison

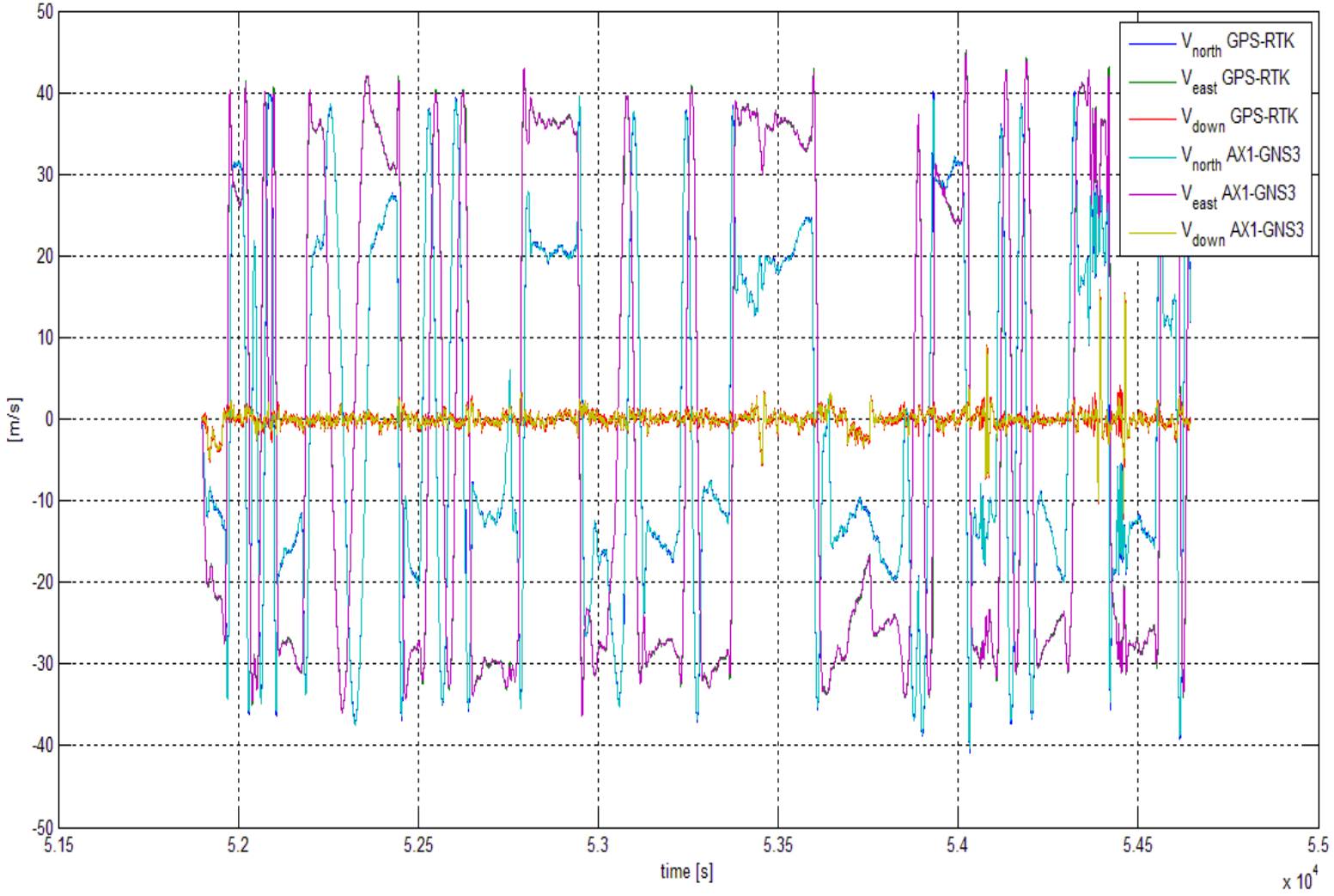

Figure 1.39 – NED velocities comparison between AX1-GNS3 system and GPS-RTK

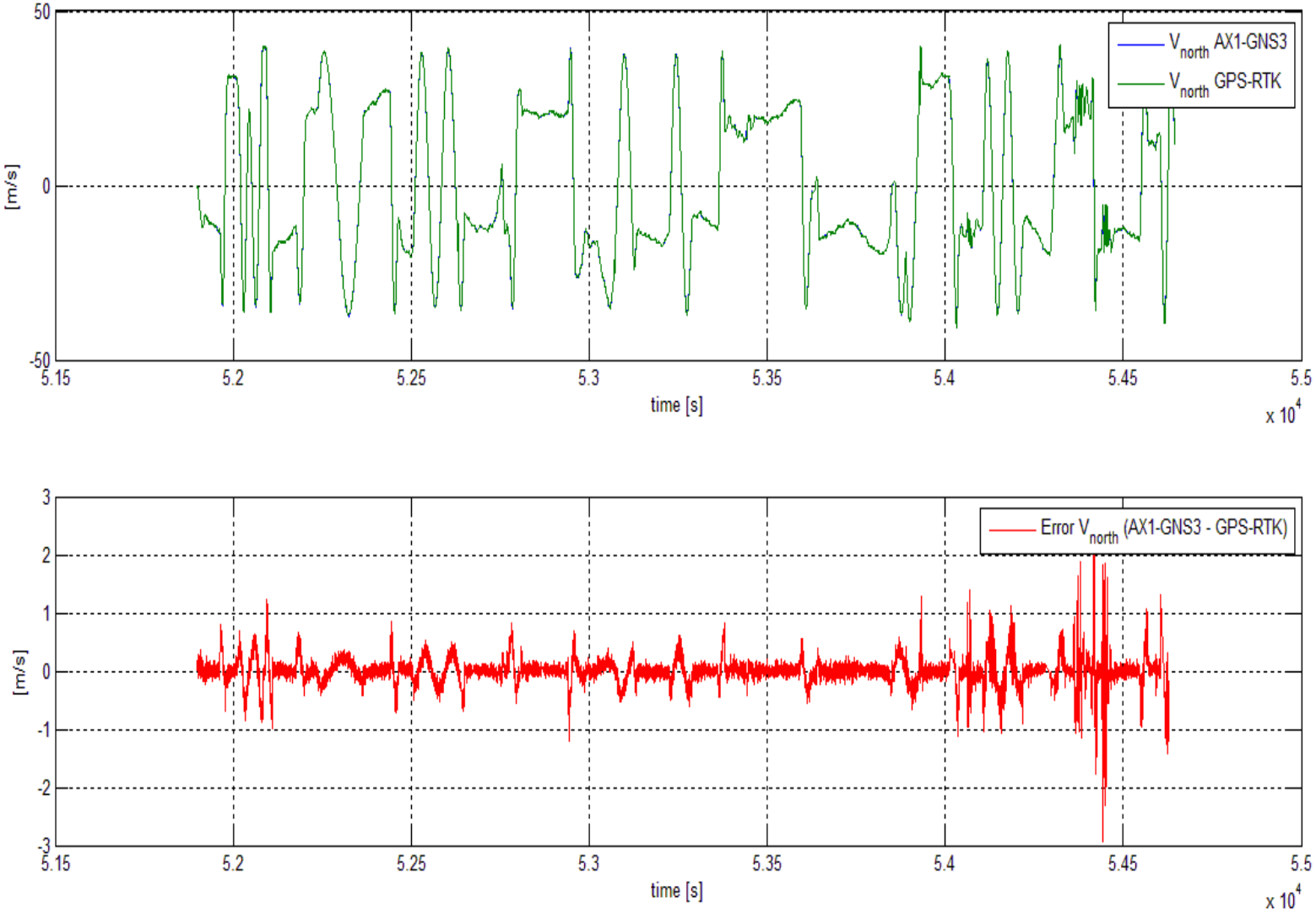

Figure 1.40 – V north deviation between AX1-GNS3 system and GPS-RTK

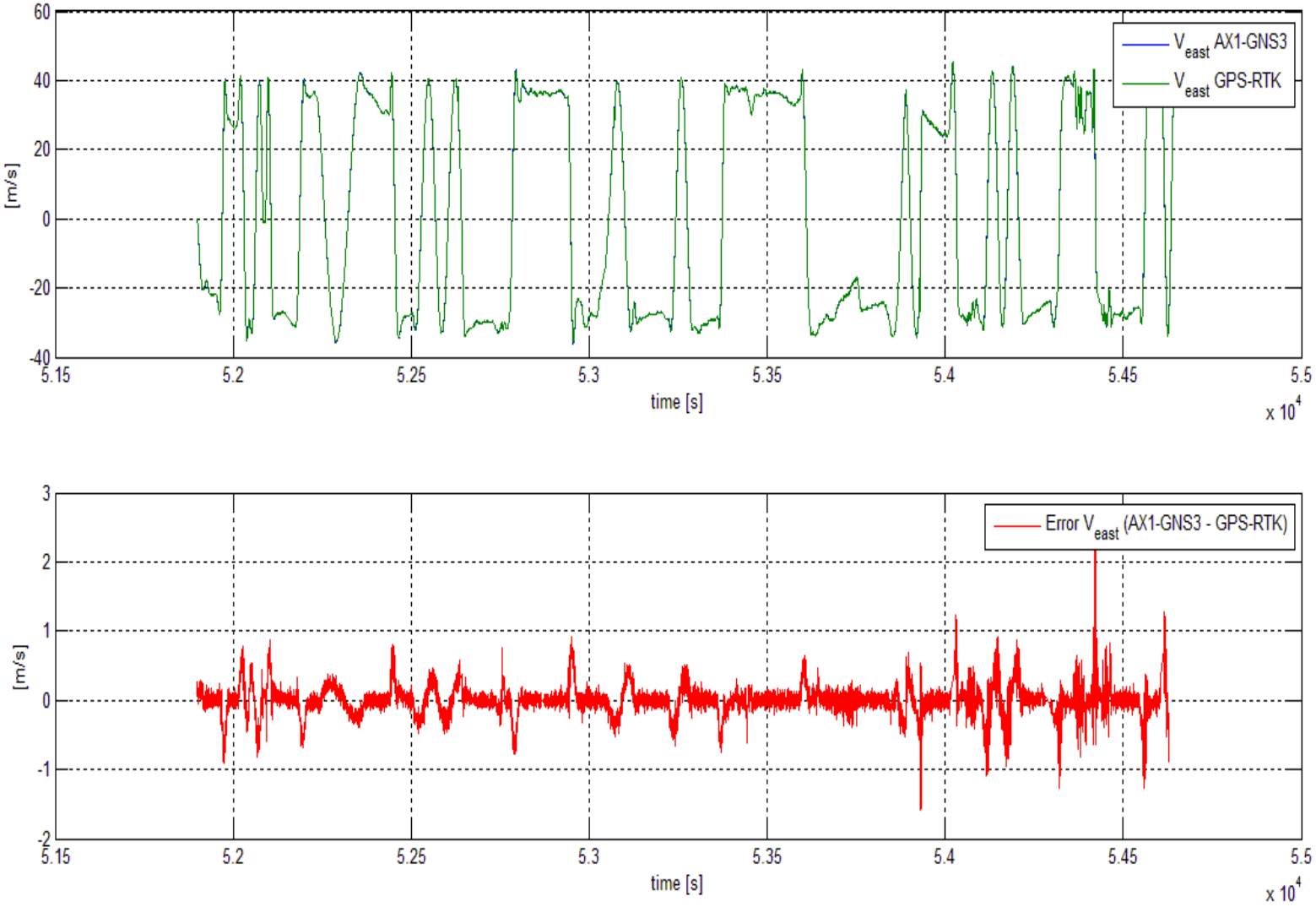

Figure 1.41 – V east deviation between AX1-GNS3 system and GPS-RTK

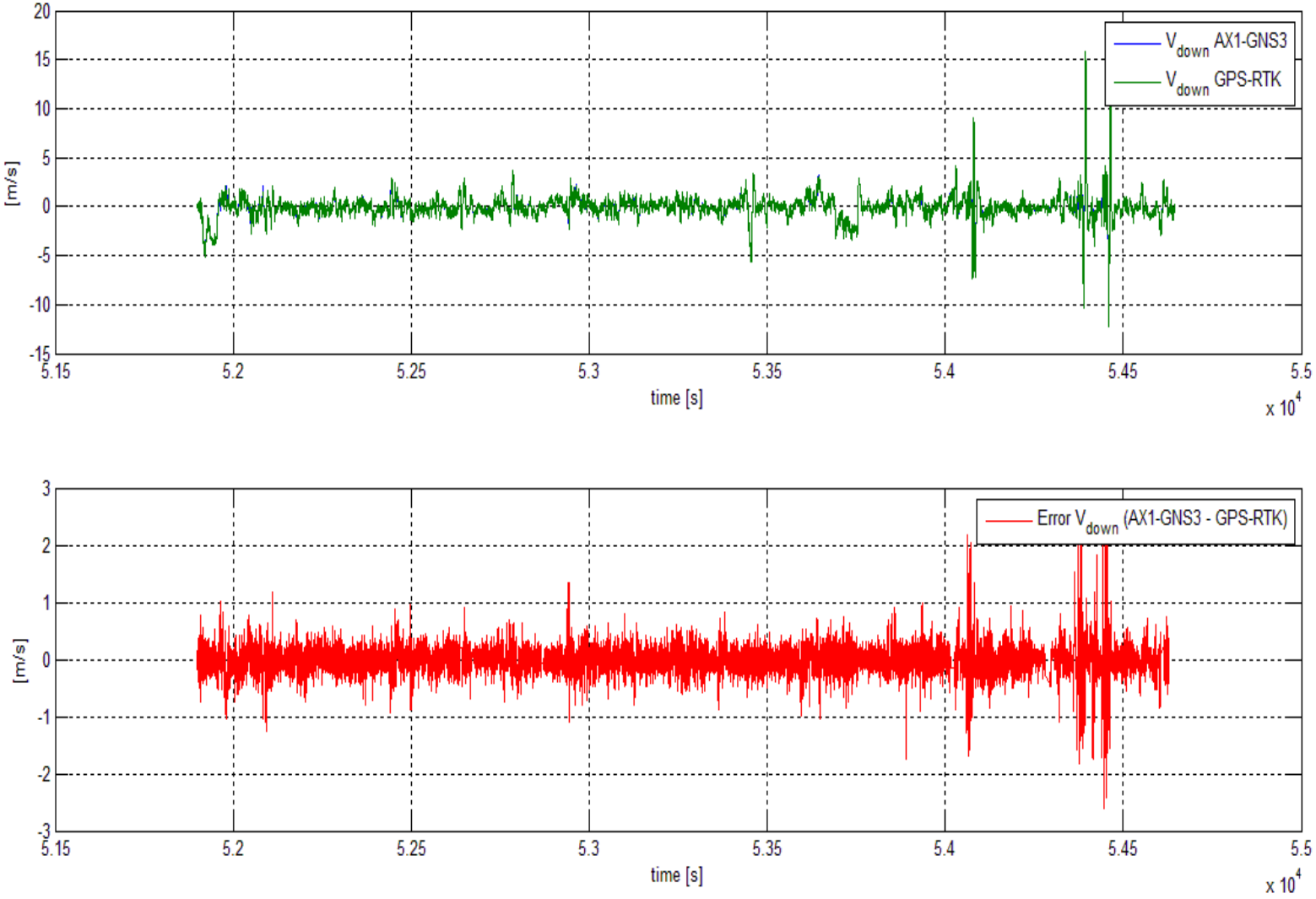

Figure 1.42 – V down deviation between AX1-GNS3 system and GPS-RTK

1.5.5 Flight Test: Geodetic Position Comparison

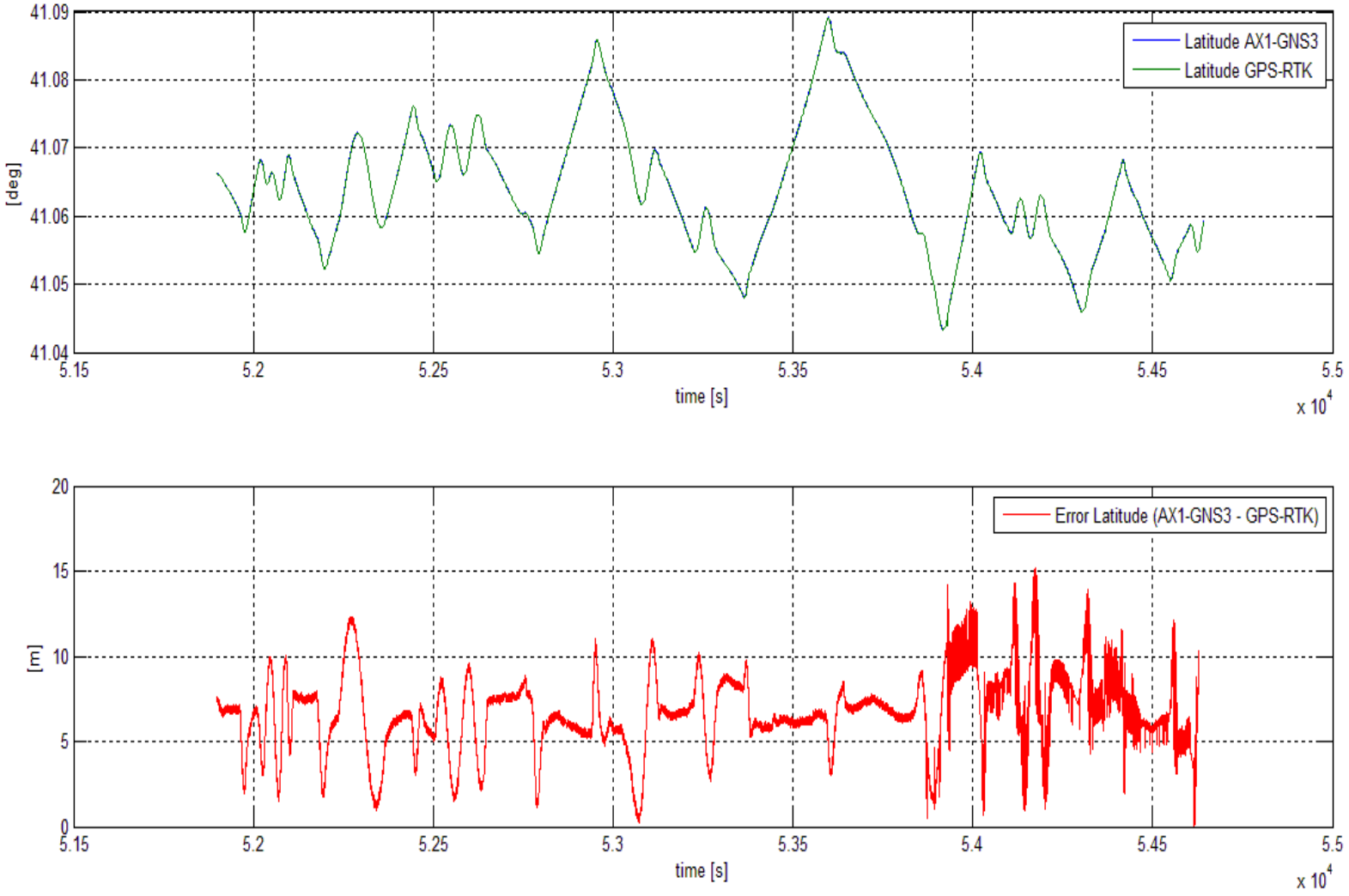

Figure 1.43 – Latitude deviation between AX1-GNS3 system and GPS-RTK

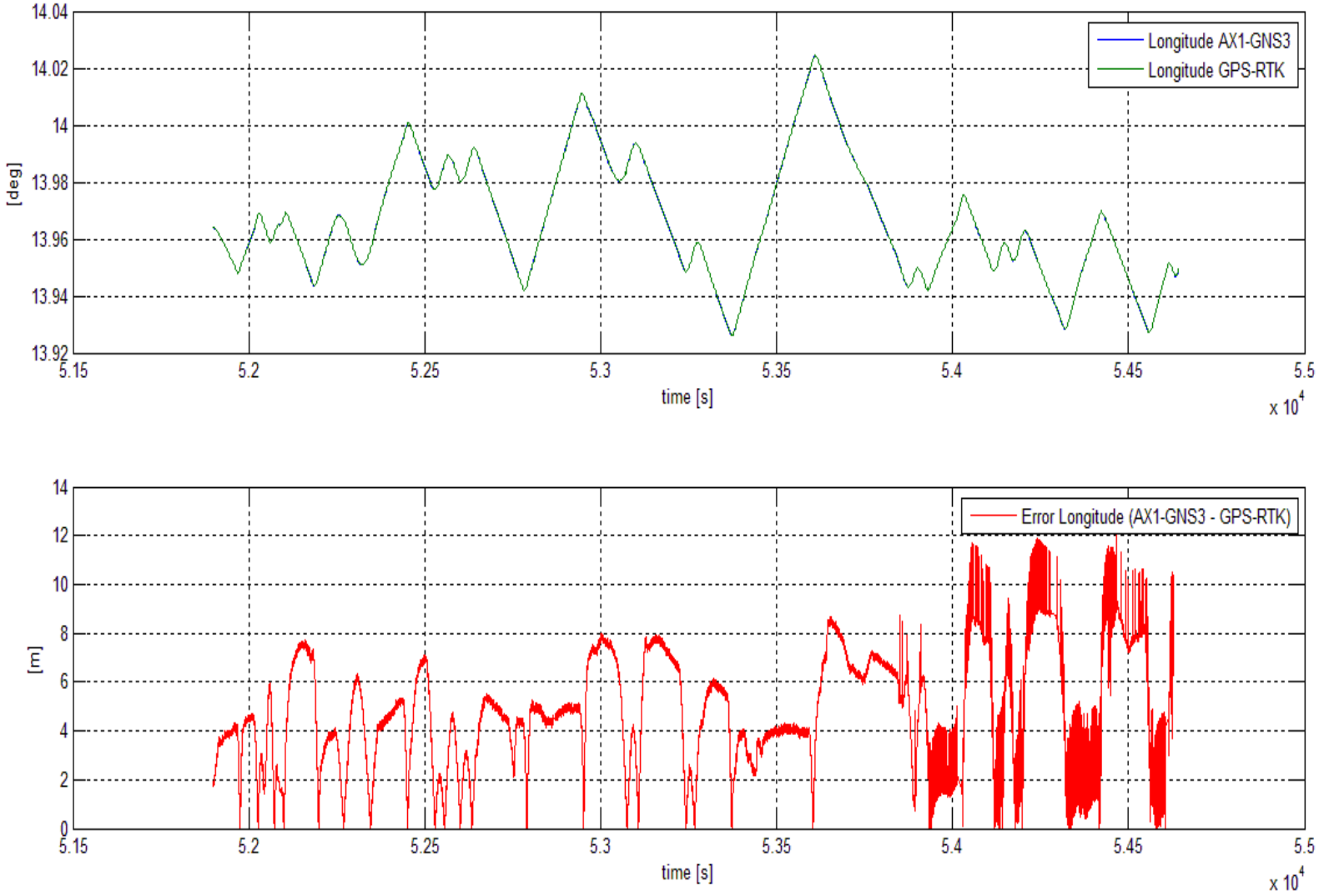

Figure 1.44 – Longitude deviation between AX1-GNS3 system and GPS-RTK

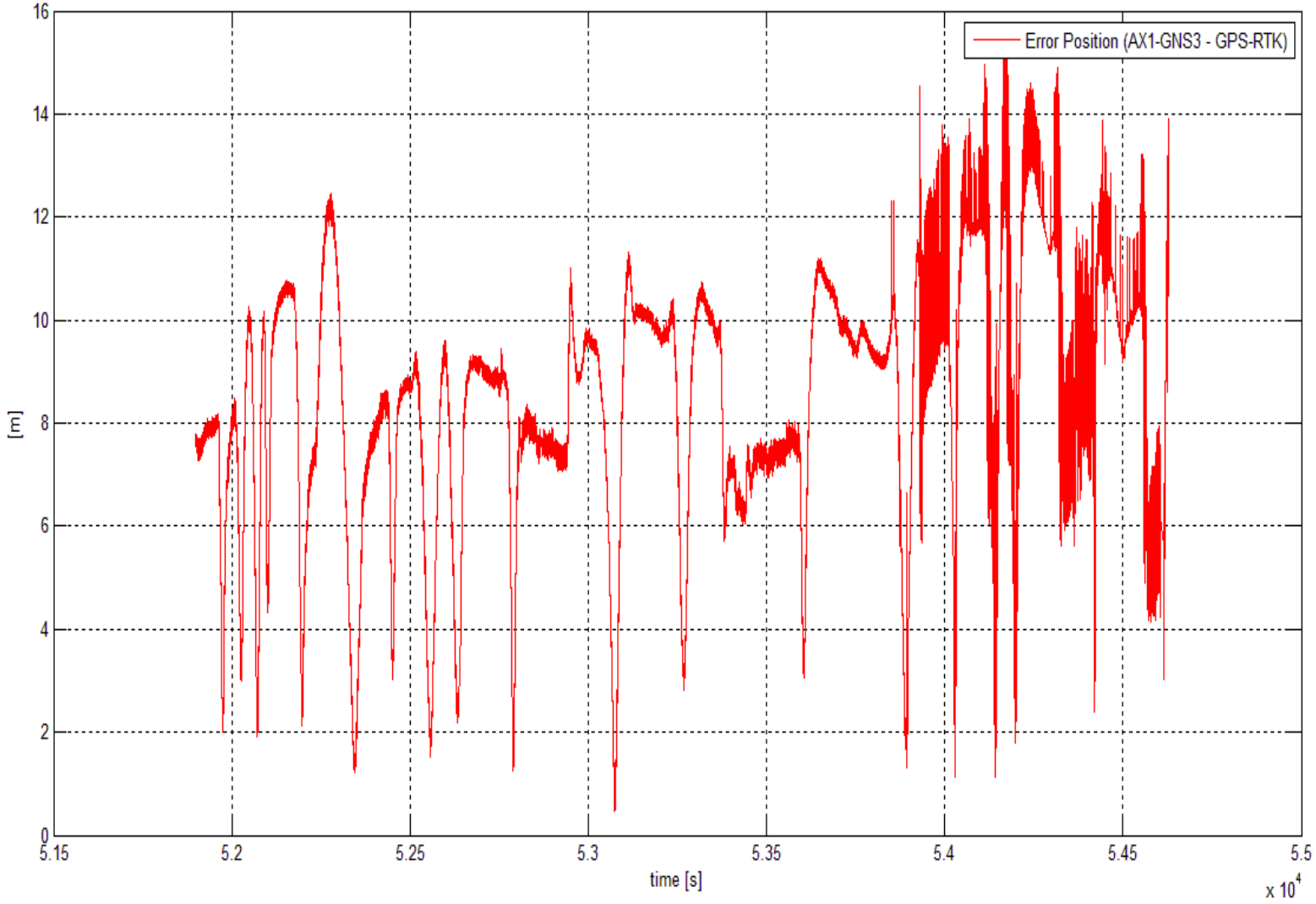

Figure 1.45 – Horizontal Position deviation between AX1-GNS3 system and GPS-RTK

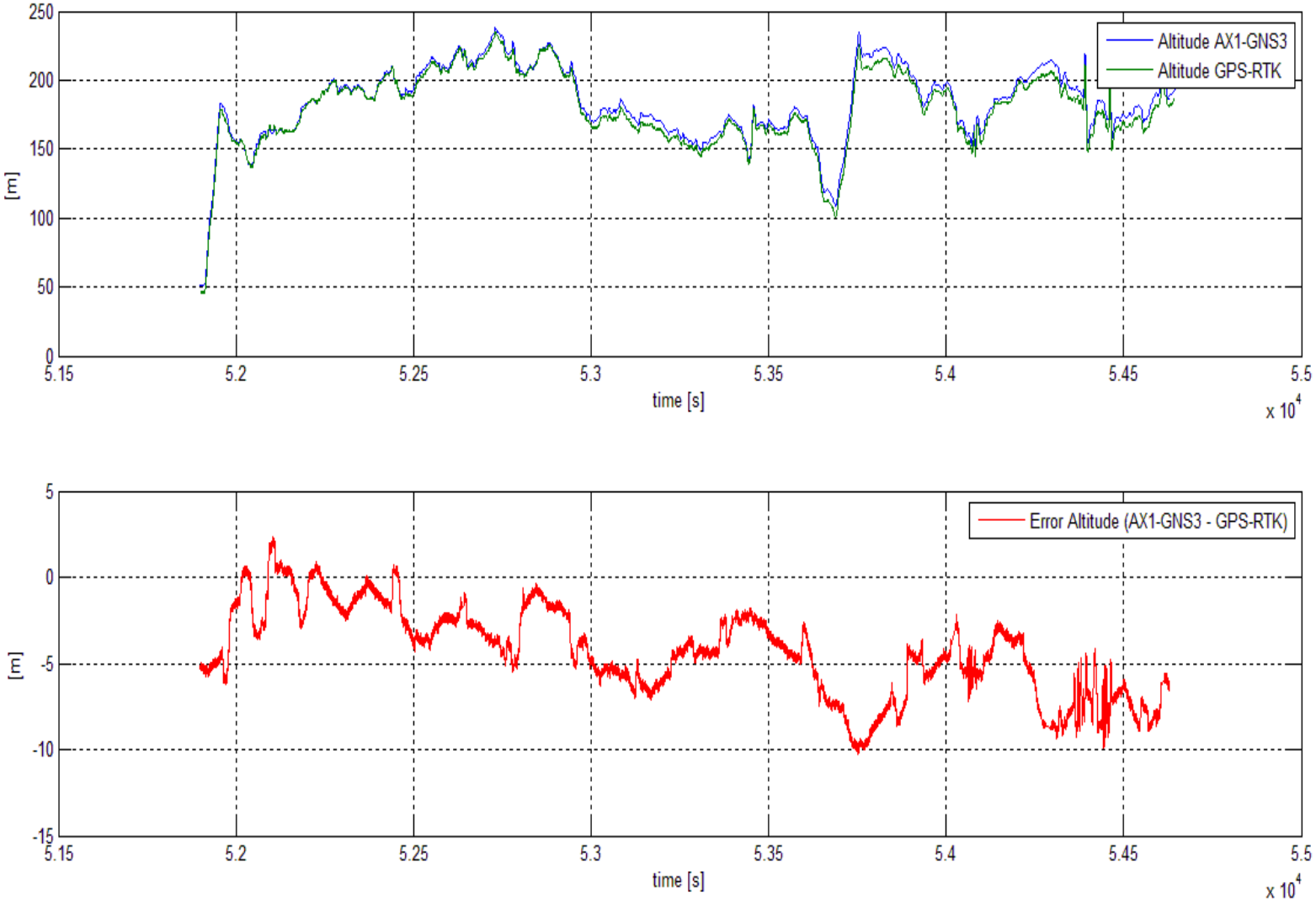

Figure 1.46 – Altitude deviation between AX1-GNS3 system and GPS-RTK

1.5.6 Flight Test: Results and Conclusions

The following tables contain the main statistics of the AX1-GNS3 Flight Test output deviations from the reference devices output.

It is important to underline that the AX1-GNS3 NED velocity and geodetic position deviations from the Trimble GPS-RTK are computed only when the GPS-RTK provide a valid output with a cm-order accuracy.

Flight Test							
Parameter	**Max Deviation**	**Mean Deviation**	**Std. Dev. (1σ)**	**RMS**	**Mean Deviation + 1σ**	**Mean Deviation + 3σ**	**Reference System**
ΔRoll [deg]	0.92	0.19	0.16	0.25	0.35	0.67	iNAV-FMS
ΔPitch [deg]	0.54	0.038	0.15	0.15	0.19	0.49	iNAV-FMS
ΔHeading [deg]	3.42	0.041	1.03	1.03	1.07	3.13	iNAV-FMS

Table 1.5 – Attitude statistics

Flight Test							
Parameter	**Max Deviation**	**Mean Deviation**	**Std. Dev. (1σ)**	**RMS**	**Mean Deviation + 1σ**	**Mean Deviation + 3σ**	**Reference System**
Vnorth [m/s]	2.92	0.0030	0.25	0.25	0.25	0.75	GPS-RTK
Veast [m/s]	2.60	-0.0040	0.23	0.23	0.23	0.69	GPS-RTK
Vdown [m/s]	2,74	-0.0093	0.28	0.28	0.29	0.85	GPS-RTK
Latitude [m]	15.18	6.67	2.14	7.00	8.81	13.09	GPS-RTK
Longitude [m]	12.10	4.70	2.43	5.29	7.13	11.99	GPS-RTK
Position [m]	15.76	8.43	2.42	8.77	10.85	15.69	GPS-RTK
Altitude [m]	10.28	-4.29	2.55	4.99	6.84	11.94	GPS-RTK

Table 1.6 – Velocity and Position statistics

Considering Table 1.5 it is possible to realize that the aim of this research activity, i.e. to develop an high performance heading and attitude determination system, has been fully satisfied. The AX1-GNS3 system provides an attitude measurement accuracy much higher than FAA requirements, a level of accuracy suitable for UAV applications. Indeed, currently the AX1-GNS3 system has been installed on the Alenia SKY-Y UAS and onboard the Italian largest UAV ever produced, the Piaggio Hammer Head MALE.

Figure 1.47 – Alenia Sky Y UAS

Figure 1.48 – Piaggio P1-HH UAS

Chapter 2

2.1 LNS Applications Scenario

The Global positioning system (GPS) is the most developed and widely used Global Navigation Satellite System (GNSS). It provides positioning, velocity, and time (PVT) information with consistent and acceptable accuracy throughout the world in all-weather conditions [12]-[13]. However, GPS positioning has many inherent shortcomings [14]. The most important problem is the signal outage: interference to the reception of GPS signals can be due to many causes such as telecommunication devices, local interference from signals or oscillators on the same platform, or possibly radar signals in nearby frequency bands. Attenuation of the GPS signal can be caused by trees, buildings, or antenna orientation, and result in reduced signal/noise ratio even without interference. Consider also the situation when the GNSS signal is deliberately blocked (Jamming or Spoofing) in hostile scenarios.
For all these reasons, the availability and reliability of the PVT informations in all environments has become a topic research theme for both military and civilian applications during the last years. As a consequence, another scope of this research activity has been to develop a self-contained, dead-reckoning system for land applications, called Land Navigator System (LNS), with the following requirements:

- to compute a PVT solution at higher frequency than the typical GNSS output solution;
- to provide a geodetic position solution error less than the 3% of the travelled distance without receiving the GPS signal.

This chapter is structured as here reported:

- first, it will be shown the HW/SW solution adopted to satisfy the above explained requirements;

- then, the schematic model of the device and the real developed device will be exposed;
- then it will be illustrated the testing strategy adopted to fully comply with the requirements;
- finally, a performance evaluation and results analysis of the conducted tests will be explained.

2.2 Adopted HW and SW Solutions

One common solution for a LNS is to use an Inertial Navigation System (INS) to bridge the gap in GPS navigation information [15]-[16]. Given the initial values of navigation parameters, the measurements from INS can be processed to determine current position, velocity, and attitude of the moving platform with respect to a certain reference frame [17]. On the other hand INS accuracy deteriorates in the long-term due to sensor's bias, drift, scale factor instability and misalignment. By integrating the GPS and INS signals, a complementary solution can be obtained that is more accurate than that of each independent system. INS has almost no high frequency errors but the errors grow up with time, while GPS, conversely, has high frequency noise but with good long-term accuracy. GPS derived positions can therefore be used to update INS and improve its long-term accuracy, whereas INS provides positioning information during GPS outages, assists GPS signal reacquisition after an outage, and is also capable of providing positioning, velocity, and attitude information at higher data rates than GPS.

However, for land applications the GPS signal can be lost for a long time and, as a consequence, the navigation solely based on INS can produce large errors in position and attitude computations. One possible solution is to employ another sensor for assisting the INS navigation, and the most common choice is to exploit the host vehicle odometer [18]-[19]-[20], due to its low cost and good accuracy capabilities. Some authors utilize two GPS receivers [21] to improve the heading computation.

The most common choice to fuse the INS/Odometer/GPS integrated system data is an Extended Kalman Filter (EKF), both in loosely and in tightly coupled architectures, even if some researchers tried to use enhanced forms of Particle Filters (PF) [22].
Figure 2.1 shows the block diagram model of the solution adopted for this research activity.

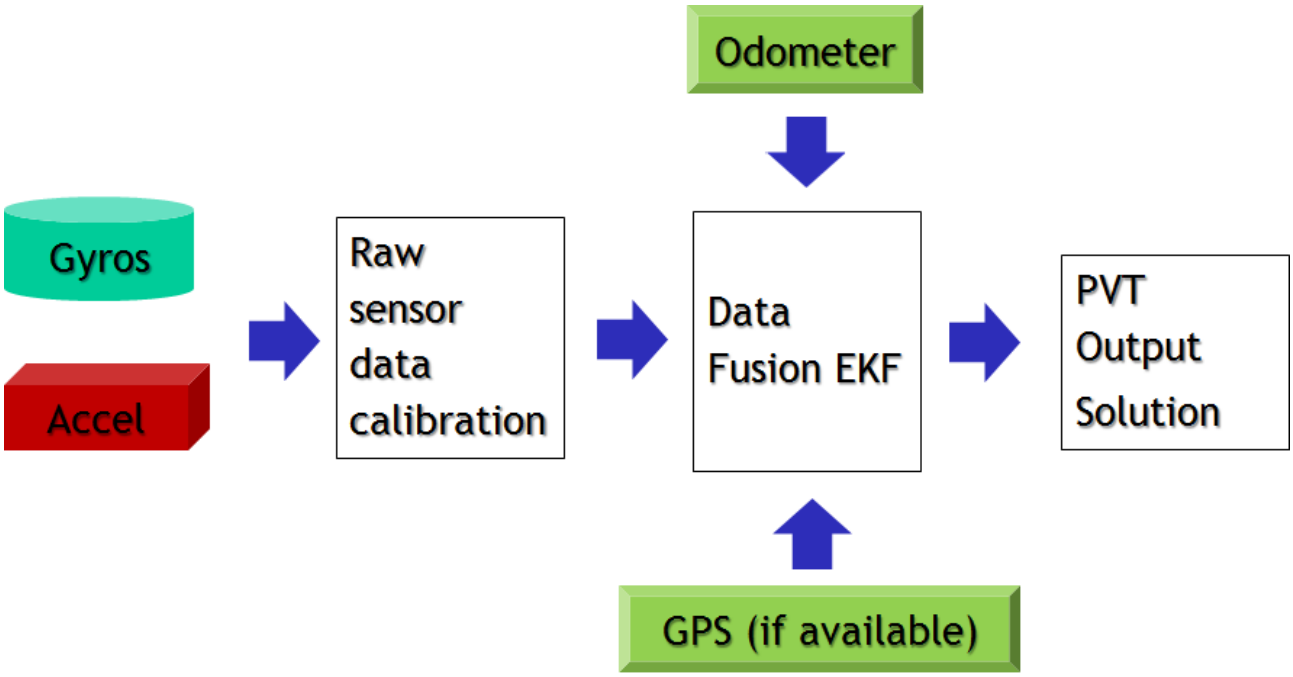

Figure 2.1 – LNS block diagram model

So, the PVT solution is provided through an Extended Kalman Filter that allows a data fusion between the inertial sensors' measurements, the GPS LLH solution (if available) and the odometer output. Again, it is also possible to note that is implemented a compensation of the inertial sensors' raw data (applying a set of calibration coefficients that are evaluated after an indoor calibration procedure) in order to remove the deterministic errors typical of MEMS inertial sensors, as in the case of the AX1-GNS3 product. It has been chosen an EKF instead of a PF because the EKF is less computationally demanding.
Even if many authors have adopted a reduced configuration [23]-[24]-[25]-[26], in this case a triad of accelerometers and of gyroscopes is adopted in order to take in account of possible different mounting configurations. Once mounted, only the z-axis

gyroscope is used to compute the heading angle and only the x-axis and z-axis accelerometers are exploited to evaluate the pitch angle. Roll angle values and variations are considered negligible for land vehicles.

For this application, it is clear that computing an affordable heading angle even in case of GPS outage is fundamental in order to comply with the error requirement above mentioned, so it is important that the gyroscopes provide a very stable output. For this reason, quasi-tactical grade gyroscopes have been chosen. Regarding the accelerometers, since they are used only for the pitch angle computation, it has been evaluated to use industrial-grade accelerometers, with performance levels comparable with the accelerometers integrated in the AX1-GNS3 system for UAV applications.

The following Figure 2.2 reports an Allan Variance plot of the quasi-tactical grade gyroscopes integrated in the LNS:

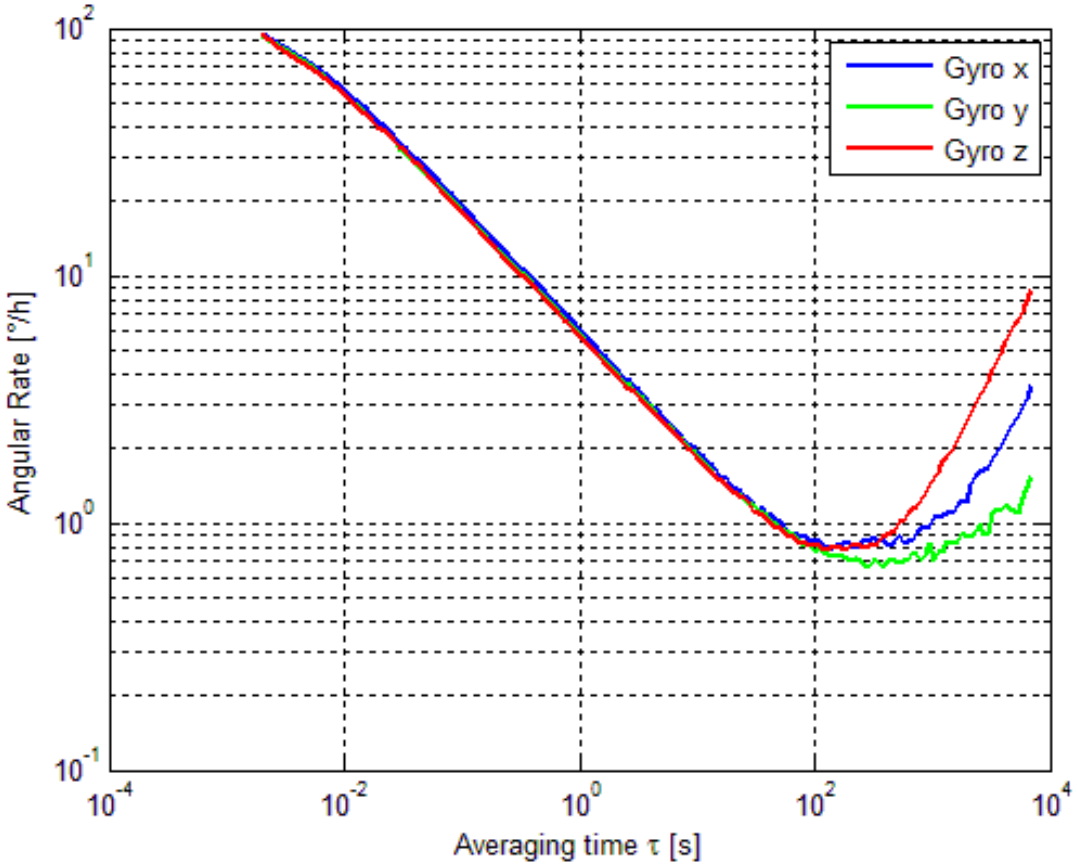

Figure 2.2 – LNS gyroscopes Allan Variance Plot

Table 2.1 contains the ARW and the Bias Instability values that are possible to evaluate from Figure 2.2. It is possible to note that the ARW is of the same levels than the industrial-grade gyroscopes used for UAV applications, but the Bias Instability is one order of magnitude better: this complies with the need for a stable output measurement even if in case of continuous GPS signal loss condition.

	ARW $(°/\sqrt{h})$	Bias Instability $(°/h)$
Gyro X	~ 0.1 (99.7 %)	~ 0.77 (96.4 %)
Gyro Y	~ 0.1 (99.7 %)	~ 0.65 (94.1 %)
Gyro Z	~ 0.1 (99.7 %)	~ 0.77 (96.5 %)

Table 2.1 – Main Noise Parameters for Gyroscopes

In the following Figure 2.3 it is depicted the final product resulting from these design activities, the Axitude AXD-LNS. The odometer is linked to the AXD-LNS via CAN bus, the GPS receiver through a 115200 bps serial interface.

Figure 2.3 – AXD-LNS Interfaces

Some technical specifications are reported in the next Table 2.2.

AXD - LNS Specifications	
Performance	
Update Rate (Hz)	1 (configurable)
Start-Up Time Valid Data (sec)	<5
Fully Stabilized Data (sec)	200
Navigation Accuracy	3% of travelled distance when GPS is not available
Electrical	
Input Supply Voltage	12 to 30 V
Power Consumption	<10 W
Digital Input & Data Format	3x RS232, CAN Bus
Physical	
Size (mm)	173x168x88.5
Weight (Kg)	1.75
Connectors	MIL DTL 26482

Table 2.2 – AXD-LNS Specifications

In the next section a brief AXD-LNS EKF description will be exposed. For more details, consider [27].

2.3 AXD-LNS EKF Description

The AXD-LNS sensor fusion algorithm scope is to provide a continuous and reliable PVT solution. This section contains a description of Kalman filtering algorithm that was used for the design and implementation of AXD-LNS.

2.3.1 EKF Basic Concepts

The state vector evolves according to the state equation

2.1. $\dot{x}(t) = f(x(t),u(t),t) + w(t)$

where $f(x(t),u(t),t)$ is a nonlinear function of the state and control vectors. The process noise *w(t)* is zero-mean white noise described by the process noise matrix *Q*.

2.2. $E[w(t)w^T(t')] = Q\delta(t-t')$

Measurement are assumed to be a nonlinear function of the state, taken at discrete time intervals, and corrupted by measurement noise *v*.

2.3. $z_k = h(x_k) + v_k$

The discrete noise sequence v_k is uncorrelated and zero-mean with covariance

2.4. $E[v_k v_s^T] = R_k \delta_{k,s}$

In the extended Kalman filter (EKF), nonlinear functions are linearized for use in propagating the matrix Ricatti equations and computing the Kalman gain. If the state error vector is defined as the difference between the true state and the state estimate

2.5. $\Delta x(t) = x(t) - \hat{x}(t)$

then a first-order linear approximation is written

2.6. $\Delta\dot{x}(t) = F(t)\Delta x(t) + G(t)\Delta u(t) + w(t)$

To arrive at F and G, the function *f(x,u,t)* is linearized about the state estimate. The Kalman filter produces both pre-measurement and post-measurement state estimates,

and the philosophy of the extended Kalman filter is to use the best state estimate available at the time linearization is required. This will denoted generically as $\hat{x}_k$. Hence,

2.7. $$F(t) = \frac{\partial f(x,u,t)}{\partial x}\Big|x = \hat{x} \quad , \quad G(t) = \frac{\partial f(x,u,t)}{\partial u}\Big|x = \hat{x}$$

The linearized measurement equation is given by

2.8. $$\Delta z_k = H_k \Delta x_k + v_k$$

where Δz_k, the innovation, contains the new information provided by the latest measurement. It is defined by

2.9. $$\Delta z_k = z_k - \hat{z}_k = z_k - h(\hat{x}_k)$$

The measurement sensitivity matrix H_k is found by linearizing $h(\hat{x}_k)$ about the current best state estimate

2.10. $$H_k = \frac{\partial h(x)}{\partial x}\Big|x = \hat{x}_k$$

The continuous Kalman filtering equations are now discretized in order to propagate the Riccati equations over the sampling interval, and discretized according to

2.11. $$\Phi(t) = e^{Ft} \quad , \quad \Phi_k \equiv \Phi(T_s)$$

The matrix Φ_k is called state transition matrix. Discrete versions of *G(t)* and *Q(t)* may be found by

2.12. $$G_k = \int_0^{T_s} \Phi(t) G(t) \Phi^T(t) dt \quad , \quad Q_k = \int_0^{T_s} \Phi(t) Q(t) \Phi^T(t) dt$$

Here again it is assumed that G and Q are approximately constant over the sampling interval T_s. Furthermore, u is assumed constant over the sampling interval. The discrete, linear space model may now be summarized as follows

2.13. $$\Delta x_{k+1} = \Phi_k \Delta x_k + G_k U_k + w_k$$

2.14. $$\Delta z_k = H_k \Delta x_k + v_k$$

The Kalman filter is applied to this model. The state transition matrix Φ_k is usually not used in the propagation step of the Kalman filter. Rather, the nonlinear dynamic equations are numerically integrated or eventually evaluated in a closed form. The state transition matrix is used only for the propagation of the Riccati equations. Anyway, because the accuracy of these computations in not needed at the same level as the state vector propagation, the transition matrix is usually approximated using only the first order term of the Taylor series e^{Ft} i.e., $\Phi_k \approx I + F_k T_s$.

2.3.2 AXD-LNS EKF Initialization Step

The AXD-LNS EKF is initialized in the following way:

- The starting LLH Geodetic Position is provided by the GPS;
- The initial body-reference Velocity is given by the odometer;
- The first pitch angle estimate is computed from the x-axis and z-axis body accelerometers with the host vehicle at rest;
- The starting z-axis gyroscope bias is also evaluated when the host vehicle is at rest;

- The initial heading angle is estimated by the GPS course over ground angle when the host vehicle performs a straight path with the odometer speed continuously higher than a threshold for few seconds.

2.3.3 AXD-LNS EKF Predictor and Integrator Step

The LLH Geodetic Position is obtained by numerically integrating geographic velocity components. Distance traveled is referenced to the body frame, which is then transformed into a local level geographic navigation frame through the pitch and heading angles**.** This implementation assumes that roll angle is sufficiently small that can be ignored.

First of all, the pitch and heading angles are updated taking in account for the inertial sensors' measurements. In more details, the pitch angle θ is evaluated from the low-pass filtered accelerometers' measurements after subtracting the accelerations due to dynamics. The heading angle ψ is obtained through a mathematical integration of the z-axis gyroscope output:

2.15. $$\psi(t_k + \tau) = \psi(t_k) + \int_{t_k}^{t_k+\tau} \dot{\psi}(t_k)dt$$

Once the new pitch and heading angles are computed, it is possible to upgrade the body to NED frame transformation matrix C_b^n. The subsequent step is to rotate the body linear velocity into the NED reference frame:

2.16. $$\underline{v}^n = C_b^n \underline{v}^b$$

The body-referenced velocity has a nonzero value for the first element, that is the speed measured by the odometer, with the other elements zero.

Finally, the latitude φ and longitude λ are obtained by numerically integrating the following differential equations:

2.17. $\dot{\varphi} = \frac{v_{north}}{R_{meridian}+h}$

2.18. $\dot{\lambda} = \frac{v_{east}}{(R_{normal}+h)\cos\varphi}$

After a numerical integration of Eqns. 2.17 and 2.18, the computed latitude φ and longitude λ are not exact, due to the following error sources:

- The gyroscopes and accelerometers measurements are affected by deterministic errors, like bias and scale factor;
- The gyroscopes and accelerometers measurements are affected by stochastic errors, like noise;
- The odometer output is affected by scale factor error.

The introduction of these error sources is reflected by the EKF Covariance Matrix propagation:

2.19. $P_k^- = \Phi_k P_{k-1} \Phi_k^T + Q_k$

where Φ_k represents the linearized form of the state propagation matrix and Q_k is the so-called Process Noise Matrix.
For this application, the error state vector δx_k and the Φ_k matrix are, respectively:

2.20. $\delta x_k = \begin{Bmatrix} \delta d^n \\ \delta d^e \\ \delta SF_{odo} \\ \delta\psi \\ \delta Bias_{gyro} \end{Bmatrix}$

2.21. $$\Phi_k = \begin{bmatrix} 1 & 0 & v_{north}\Delta t & -v_{east}\Delta t & 0 \\ 0 & 1 & v_{east}\Delta t & v_{north}\Delta t & 0 \\ 0 & 0 & 1 & 0 & 0 \\ 0 & 0 & 0 & 1 & \Delta t \\ 0 & 0 & 0 & 0 & 1 \end{bmatrix}$$

where:

- δd^n and δd^e represent the position errors along north and east directions;
- δSF_{odo} is the odometer measurement scale factor error;
- $\delta\psi$ represents the heading angle error;
- $\delta Bias_{gyro}$ is the z-axis gyroscope bias;
- Δt is the EKF step time.

In order to satisfy the performance requirements, the odometer and inertial sensors' errors have to be eliminated as much as possible through a calibration procedure and the residual errors shall be estimated and removed via the implemented EKF. The aiding sensor, that in this application is represented by the GPS (if available), provides stable measurements that can be exploited as reference to estimate these error sources.

2.3.4 AXD-LNS EKF Measurement Update Step

When the GPS provides a valid measurements of geodetic latitude φ_{GPS}, longitude λ_{GPS} and WGS-84 altitude h_{GPS}, the north and east measurement innovation vector δz_k is formed from the difference between the GPS output and the geodetic latitude φ_k^- and longitude λ_k^- computed, at the same time, after the EKF predictor and integrator step described in the previous sub-section:

2.22. $$\delta z_k = \begin{Bmatrix} \Delta n \\ \Delta e \end{Bmatrix} = \begin{Bmatrix} \frac{\varphi_{GPS} - \varphi_k^-}{R_{meridian} + h_{GPS}} \\ \frac{\lambda_{GPS} - \lambda_k^-}{(R_{normal} + h_{GPS})\cos\varphi_k^-} \end{Bmatrix}$$

Then the Kalman Gain Matrix shall be evaluated:

2.23. $$K_k = P_k^- H_k^T (H_k P_k^- H_k^T + R_k)^{-1}$$

taking in account that R_k is the Measurement Error Matrix, P_k^- is the last Covariance Error Matrix evaluated as Eqn. 2.19 during the Predictor and Integrator step, and

2.24. $$H_k = \begin{bmatrix} 1 & 0 & 0 & 0 & 0 \\ 0 & 1 & 0 & 0 & 0 \end{bmatrix}$$

Once K_k is computed, it is possible to evaluate the error state vector δx_k and to update the Covariance Error Matrix P_k:

2.25. $$\delta x_k = K_k \delta z_k$$

2.26. $$P_k = (I - K_k H_k) P_k^-$$

Finally, the "true" state vector x_k shall be evaluated summing the error state vector δx_k to the state vector x_k^- computed after the Predictor and Integrator step and, as a consequence, affected by odometer and inertial sensors' errors:

2.27. $$x_k = x_k^- + \delta x_k$$

2.4 Testing Strategy

A three-steps testing strategy has been adopted in order to achieve an high rate, continuous and affordable PVT solution suitable to comply with the performance requirement, that is a geodetic position error less than the 3% of the travelled distance without receiving the GPS signal:

1. Laboratory Testing for raw sensor data calibration in order to evaluate and compensate the accelerations and angular rates measurement deterministic errors;
2. Van Testing for EKF tuning, SW field validation and performance evaluation;
3. PC simulations to test the EKF capabilities.

Regarding the lab testing, the same procedures described in section § 1.3 have been adopted: MEMS inertial sensors performances have been improved through static and dynamic tests on a turntable and thermal tests in a climatic chamber in order to compensate their deterministic sources of errors. For this reason, only the last two testing strategy points will be exposed in more details in the next sub-sections.

2.4.1 LNS Van Testing Activities

The AXD-LNS testing activities included a Van Test campaign to be performed during July-October 2013 in the surroundings of Giugliano in Campania (NA), Italy.

Aims of this Van Test campaign were:

1. to acquire AXD-LNS system raw data in order to execute a tuning of the EKF explained in section § 2.3;
2. to validate the AXD-LNS embedded SW;
3. to give demonstration of the Axitude AXD-LNS capabilities through a comparison between its geodetic position solution when GPS signal is lost and a reference “true” geodetic position.

Many tests have been performed. For every test, the following procedure has been executed:

- After the AXD-LNS has been turned on, the host vehicle remains at rest for few minutes in order to allow a first estimate of the pitch angle and to compensate the z-axis gyroscope bias;
- Then, the host vehicle executes a straight path with speed higher than a prefixed threshold. In this way, the AXD-LNS true heading is initialized with the GPS course over ground value;
- The host vehicle travels with the GPS signal present, usually only for few minutes in order to allow the EKF convergence;
- Finally, through a SW command, it is "simulated" a GPS signal loss until the end of the journey, but in reality the GPS signal is still acquired. In this way it is possible to compare the AXD-LNS PVT output, computed in absence of the GPS signal, and the "true" PVT output given by the GPS solution.

The following Figure 2.4 shows the Van Test setup, that is the same for every test.

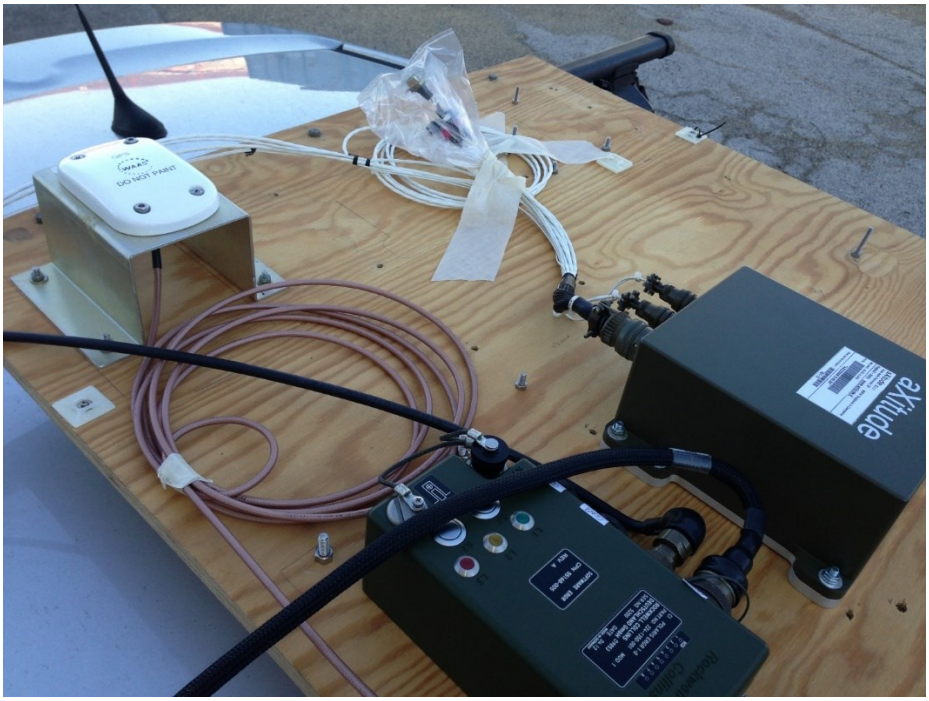

Figure 2.4 – Van Test Setup

Only four tests are reported later in this sub-section. For every test it is reported:

- a first figure (realized through *Google Earth*^{TM}) containing a comparison between the AXD-LNS and the GPS PVT solution. The green balloon represents the point from which the GPS signal is imposed to be lost for the AXD-LNS output;
- a second figure, where the same comparison and the trend of the AXD-LNS geodetic position percentage error over the distance travelled without receiving the GPS signal are shown;
- a table containing the AXD-LNS statistics: when evaluating the performance the first samples have been overlooked because immediately after the GPS signal loss the travelled distance is zero and so the percentage error tends to infinite;
- only for the last test are reported also an WGS-84 altitude comparison and related statistics.

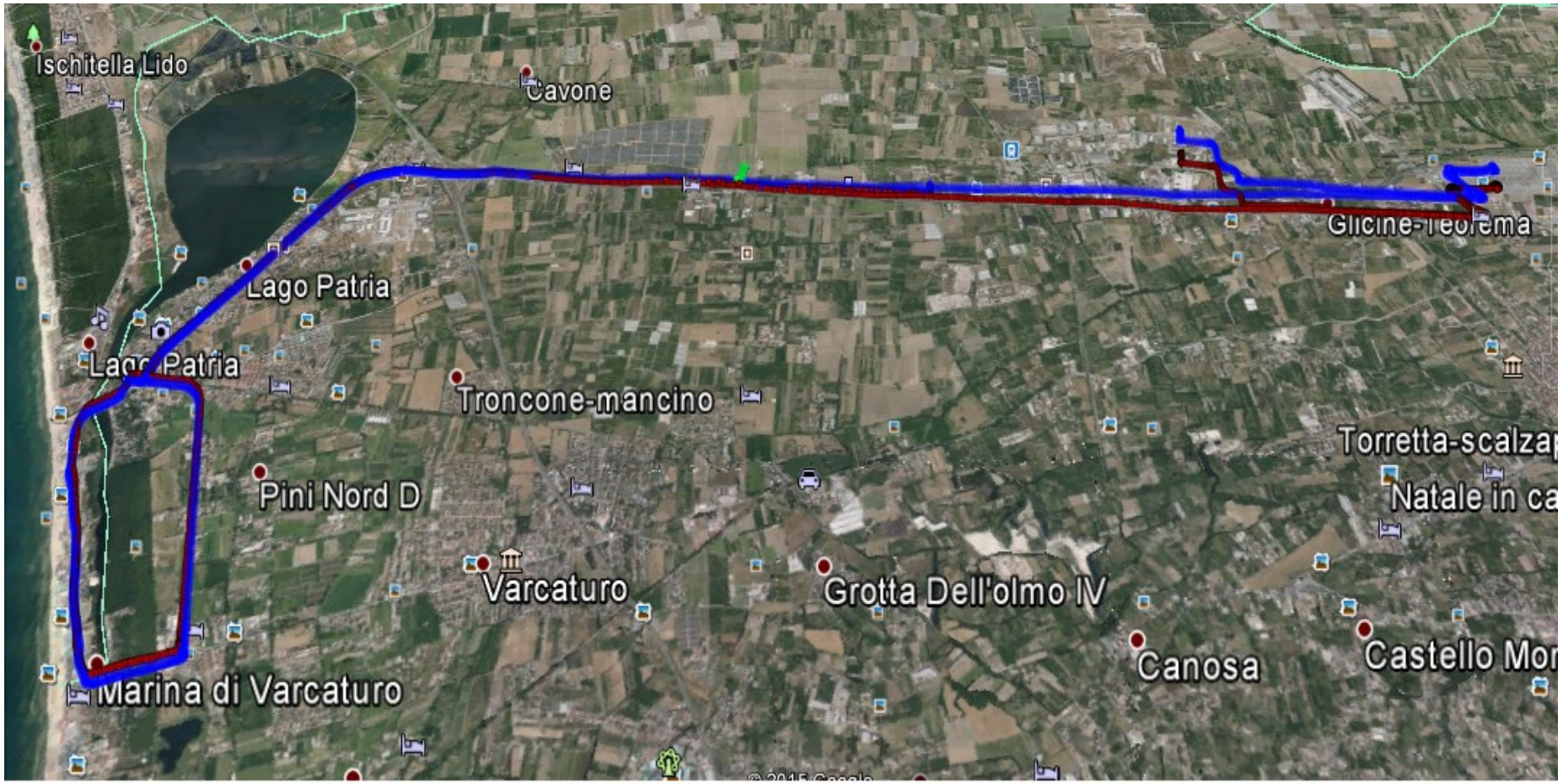

Figure 2.5 – First Van Test: Geodetic Position comparison between AXD-LNS (blue) and GPS (red) solutions

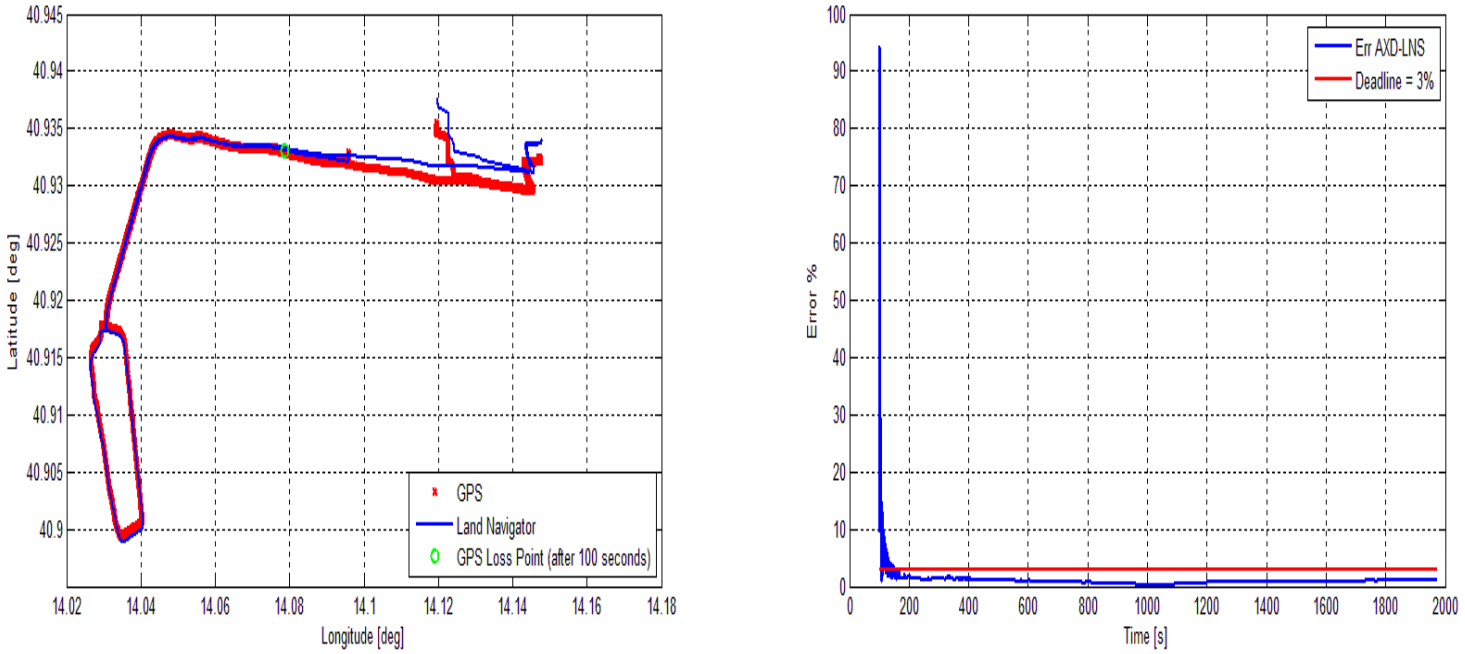

Figure 2.6 – First Van Test: (1) Geodetic Position comparison between AXD-LNS (blue) and GPS (red); (2) AXD-LNS Error % after GPS Loss Point

Performances (without GPS for 26 Km in about 30 minutes)				
Err Max	Err Mean	Err Std	Err Rms	Err 1 σ
< 1.9 %	< 0.8 %	< 0.3 %	< 0.9 %	< 1.1 %

Table 2.3 – First Van Test: AXD-LNS Performances

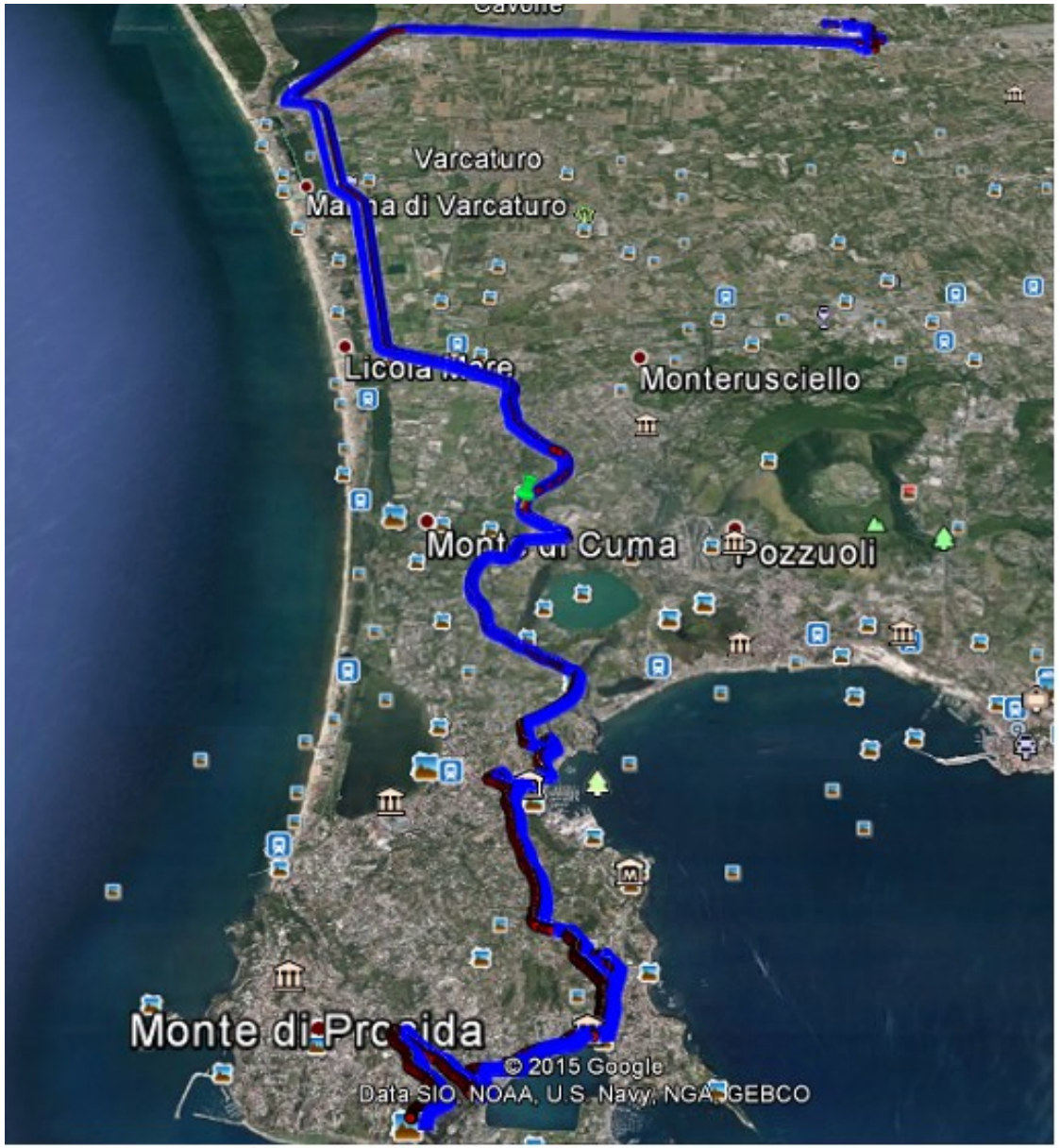

Figure 2.7 – Second Van Test: Geodetic Position comparison between AXD-LNS (blue) and GPS (red) solutions

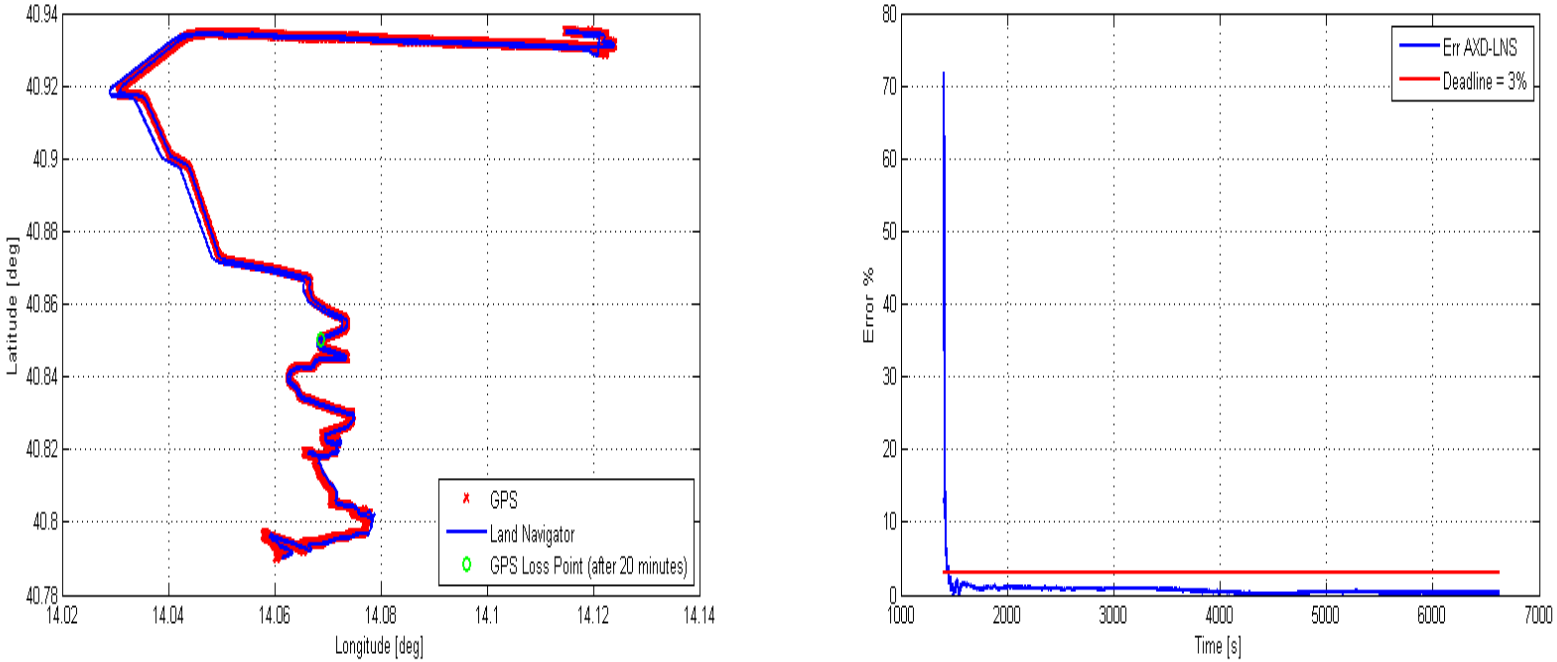

Figure 2.8 – Second Van Test: (1) Geodetic Position comparison between AXD-LNS (blue) and GPS (red); (2) AXD-LNS Error % after GPS Loss Point

Performances (without GPS for 45 Km in about 90 minutes)				
Err Max	Err Mean	Err Std	Err Rms	Err 1 σ
< 1.7 %	< 0.6 %	< 0.3 %	< 0.7 %	< 0.9 %

Table 2.4 – Second Van Test: AXD-LNS Performances

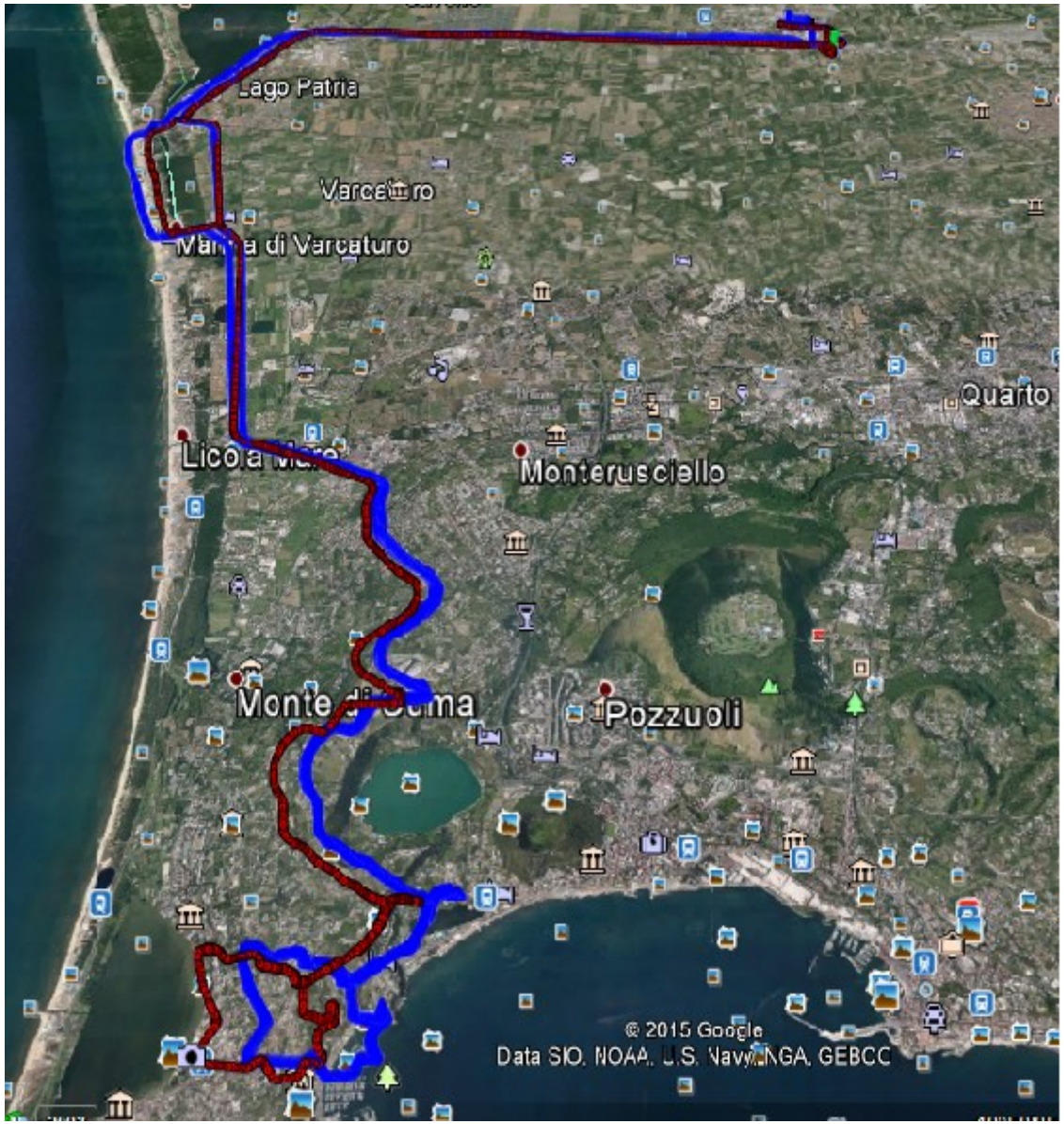

Figure 2.9 – Third Van Test: Geodetic Position comparison between AXD-LNS (blue) and GPS (red) solutions

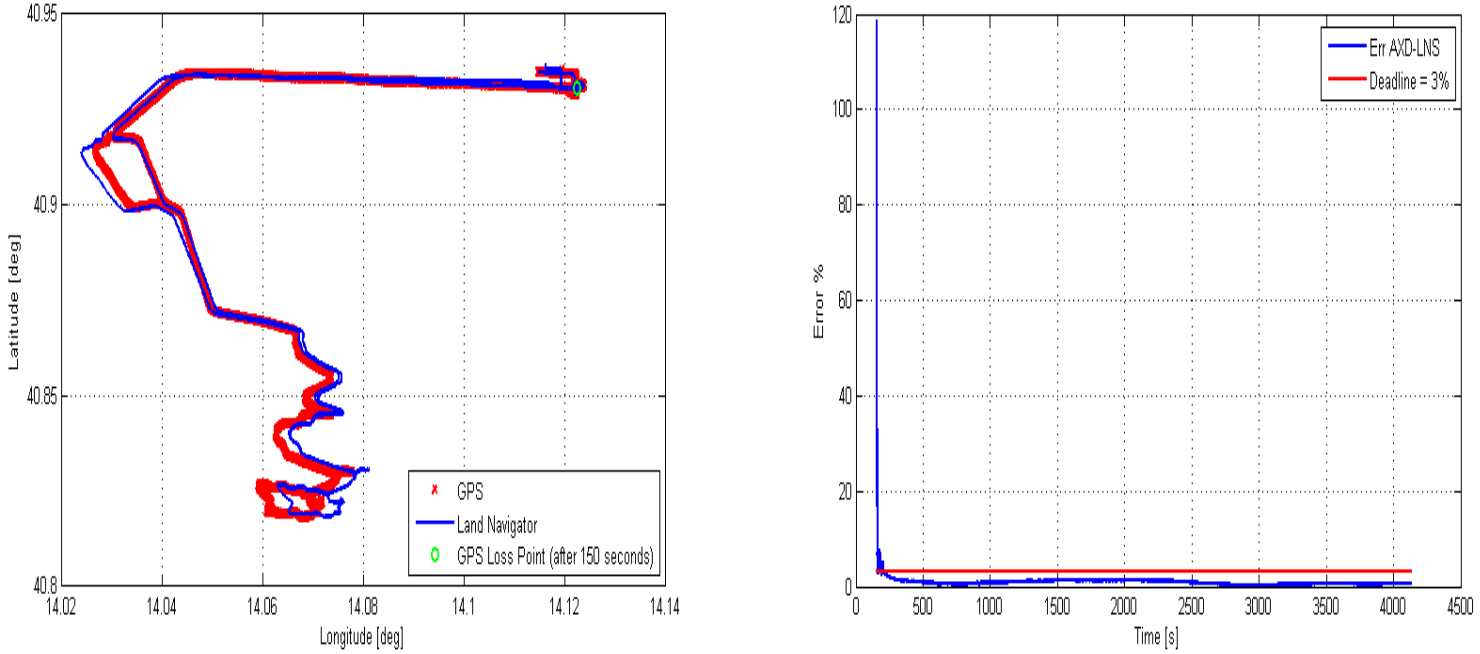

Figure 2.10 – Third Van Test: (1) Geodetic Position comparison between AXD-LNS (blue) and GPS (red); (2) AXD-LNS Error % after GPS Loss Point

Performances (without GPS for 56 Km in about 66 minutes)				
Err Max	Err Mean	Err Std	Err Rms	Err 1 σ
< 2.0 %	< 0.8 %	< 0.4 %	< 0.9 %	< 1.2 %

Table 2.5 – Third Van Test: AXD-LNS Performances

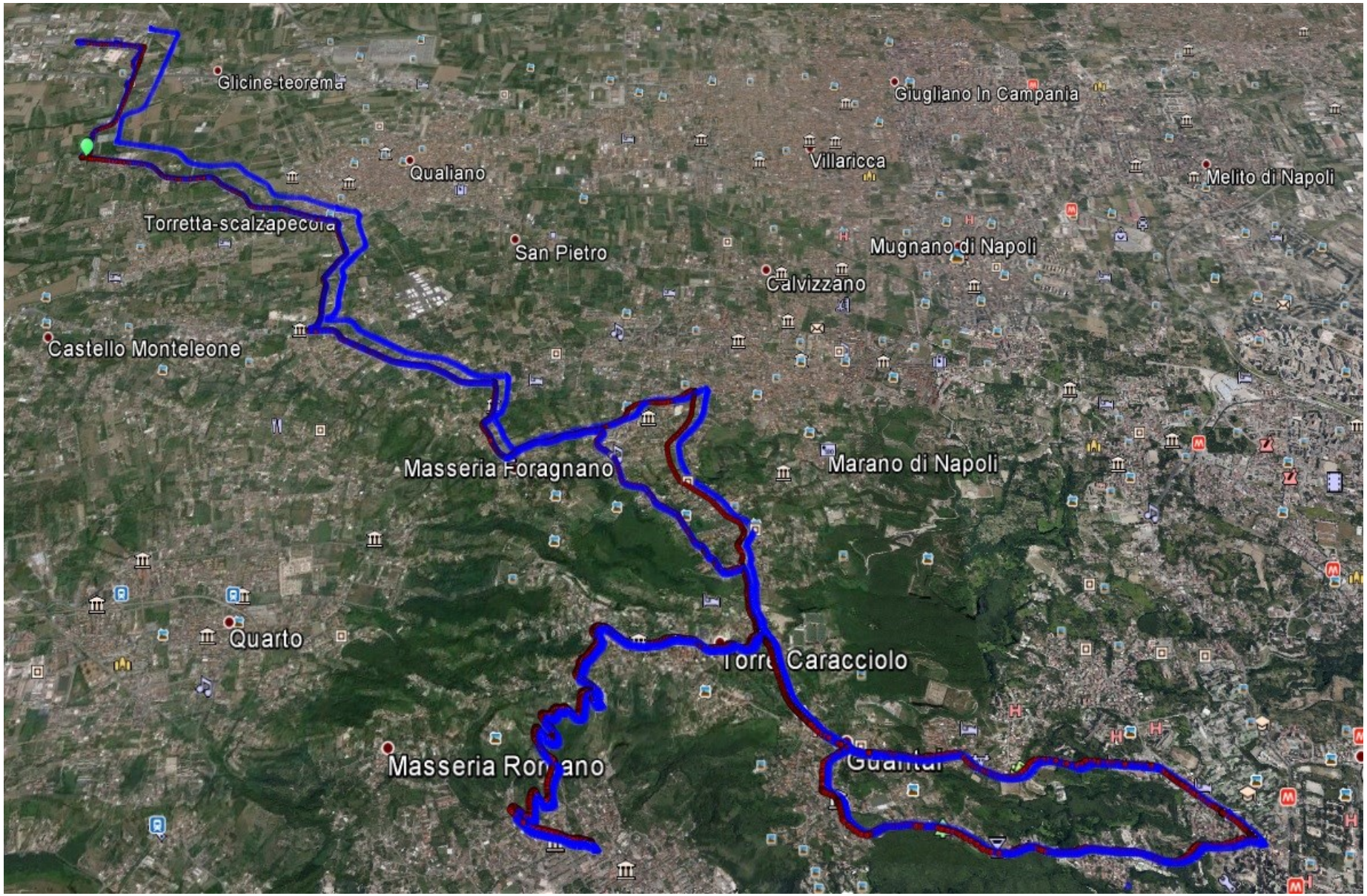

Figure 2.11 – Fourth Van Test: Geodetic Position comparison between AXD-LNS (blue) and GPS (red) solutions

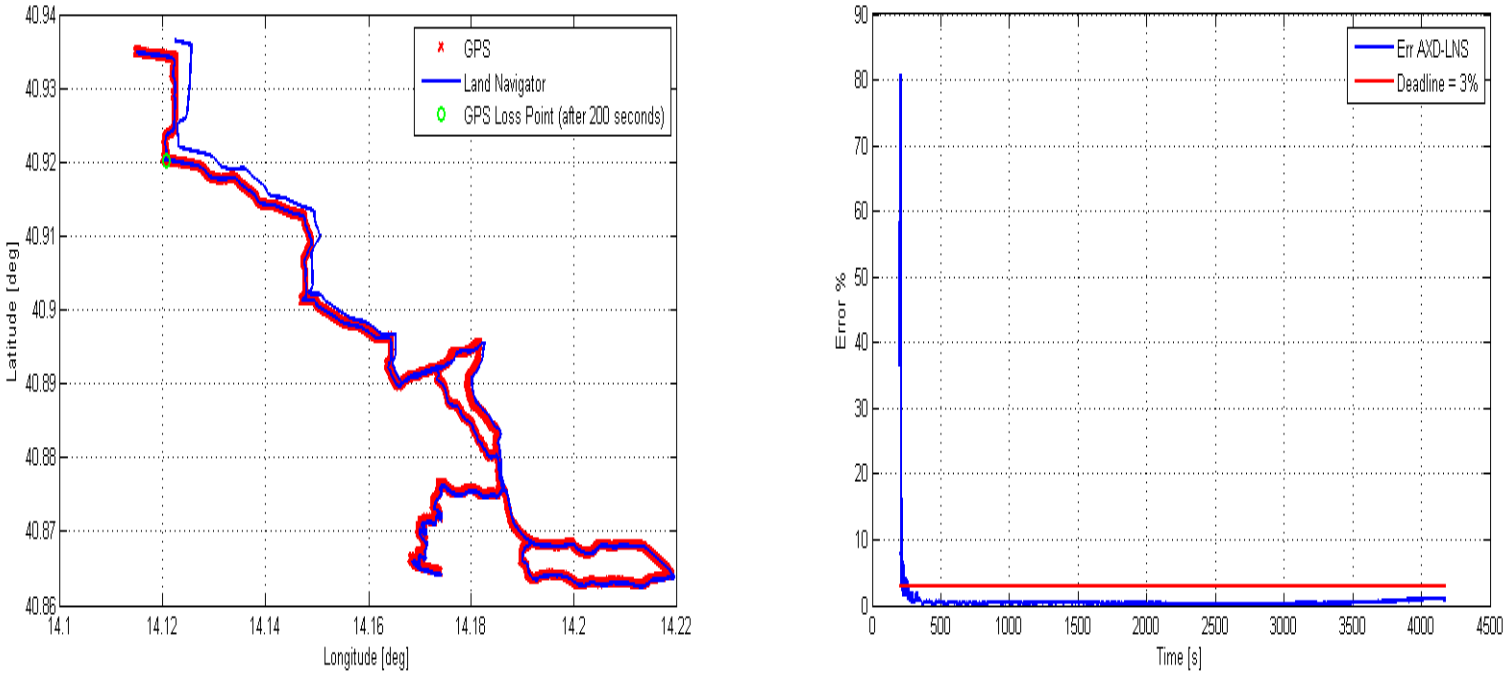

Figure 2.12 – Fourth Van Test: (1) Geodetic Position comparison between AXD-LNS (blue) and GPS (red); (2) AXD-LNS Error % after GPS Loss Point

Performances (without GPS for 40 Km in about 66 minutes)				
Err Max	Err Mean	Err Std	Err Rms	Err 1 σ
< 1 %	< 0.4 %	< 0.2 %	< 0.5 %	< 0.6 %

Table 2.6 – Fourth Van Test: AXD-LNS Performances

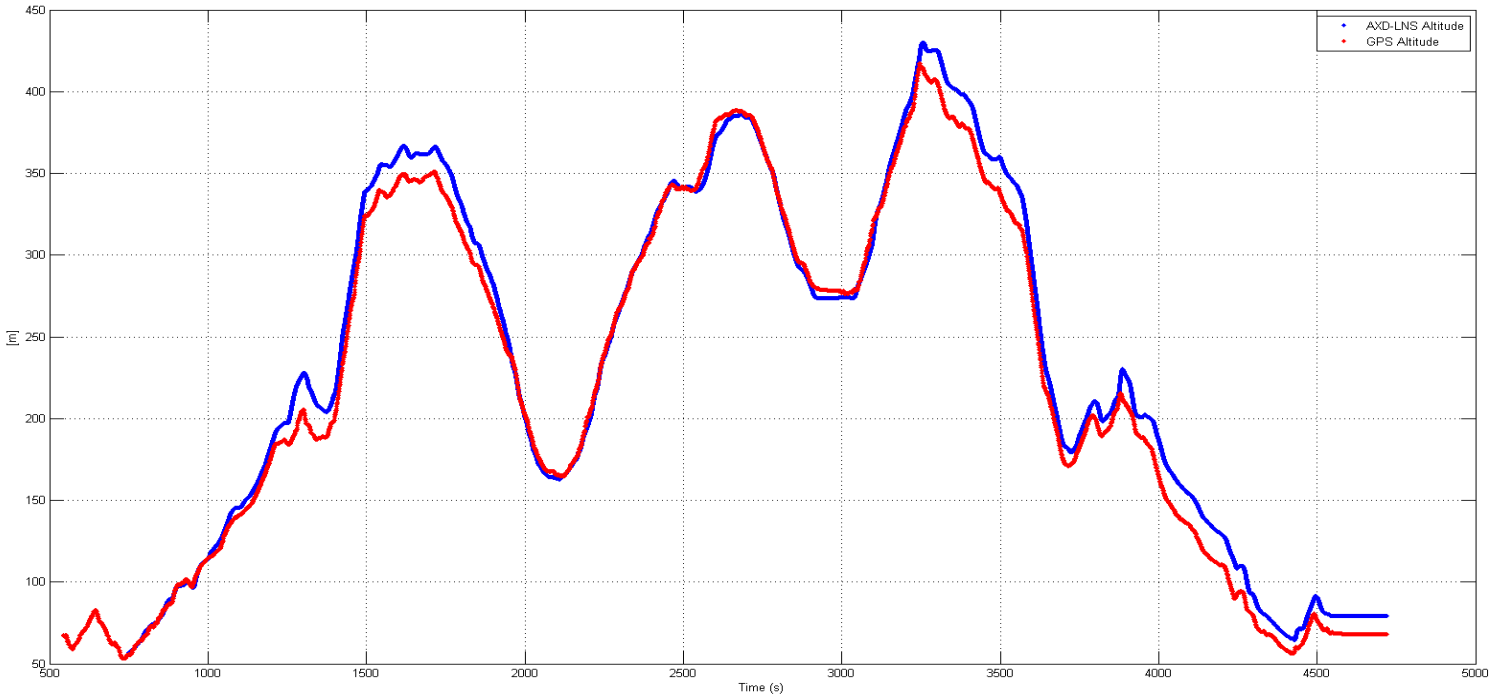

Figure 2.13 – Fourth Van Test: WGS-84 Altitude Position comparison between AXD-LNS (blue) and GPS (red)

Altitude Performances (without GPS for 40 Km in about 66 minutes)			
Err Max	Err Mean	Err Std	Err Rms
≈ 28 m	≈ 10 m	≈ 7 m	≈ 12 m

Table 2.7 – Fourth Van Test: AXD-LNS Altitude Performances

2.4.2 LNS PC Simulation Activities

In this sub-section two AXD-LNS PC simulation activities will be described in order to demonstrate some EKF capabilities. In more details, it will be shown:

1. the EKF capability to recover large heading errors in a very short time;
2. the need for taking in account of the odometer scale factor error.

Regarding the first activity, consider Figure 2.14: the yellow circle indicates the mission start point, the host vehicle is oriented towards west and travels towards west following the red points, that are the GPS geodetic position solutions. It has been simulated that the AXD-LNS receives as input an initial heading different of 180° from its true value, so committing a 180° initial heading error. In fact, the AXD-LNS output (the blue line) is initially oriented towards east. But as soon as the host vehicle moves from its initial position, the EKF corrects this very large initial heading error and in less than a minute reports the heading angle aligned with the road (green circle in Figure 2.14).

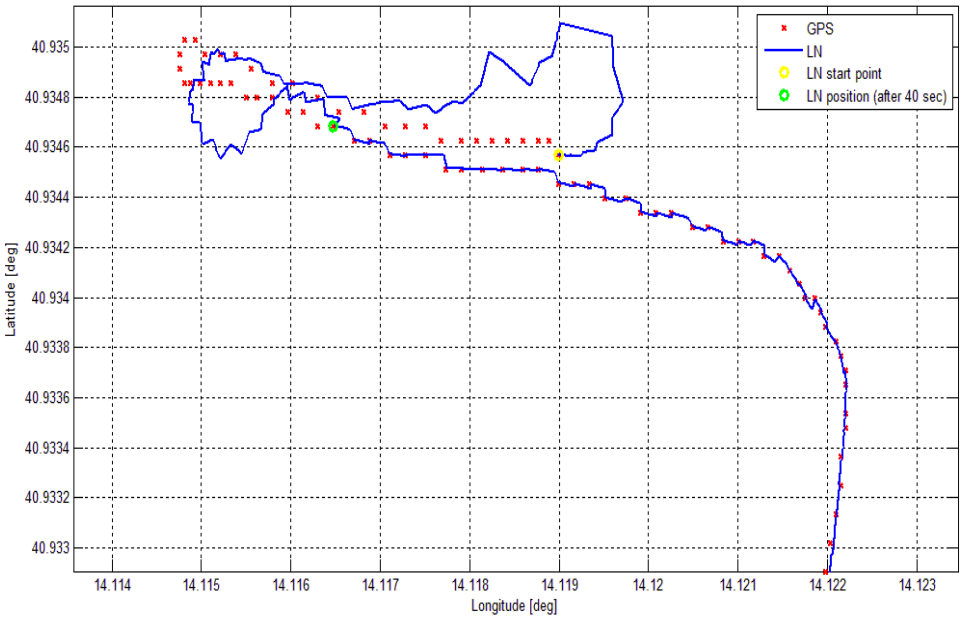

Figure 2.14 – PC Simulation: Very large initial heading error correction in a very short time

Regarding the second activity, look at Figure 2.15: the red points represent a real odometer output, acquired during a van test. It is possible to note that around 3000 seconds after the start of the journey, the host vehicle is at rest for about five minutes. It has been simulated that in this period of time the host vehicle experiments a wheel deflation that results in an 4% increased speed, so when the host vehicle starts again the odometer output is increased of a 4% respect to its original output (blue points in Figure 2.15).

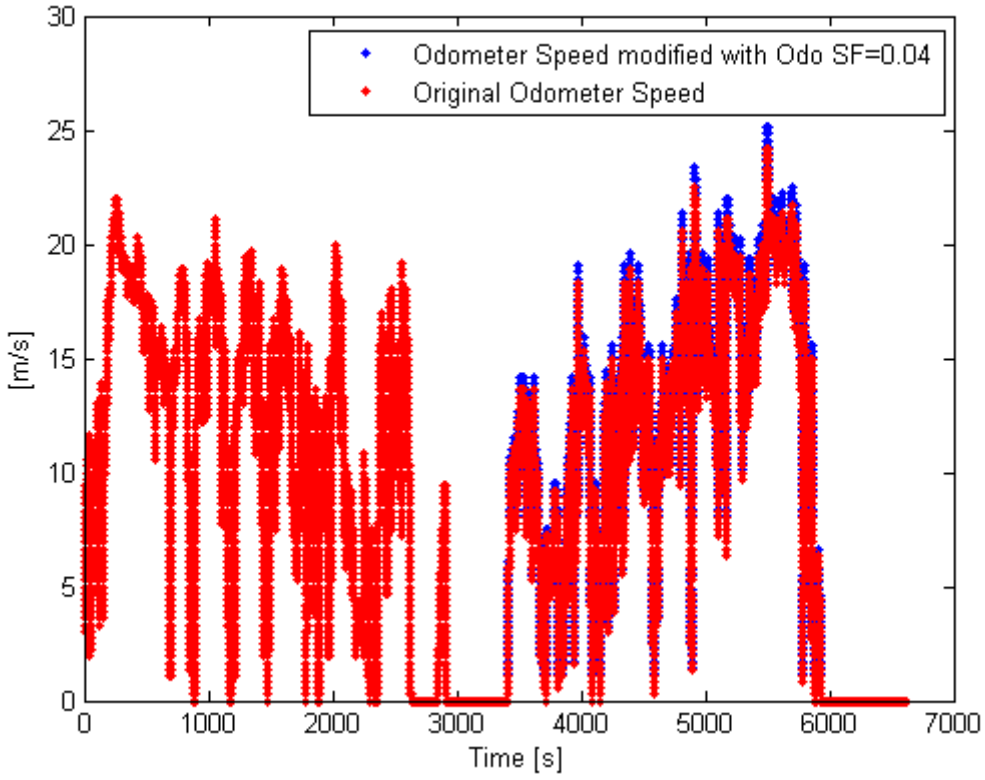

Figure 2.15 – PC Simulation: real odometer data (in red) and simulated odometer output (in blue)

Now it is interesting to investigate the AXD-LNS output if the EKF estimates or not an odometer scale factor error. Figure 2.16 compares the GPS output with the AXD-LNS solution when there is not a scale factor correction implemented in the EKF. The yellow circle indicates the geodetic position where the host vehicle is at rest and "experiments" a wheel deflation. Then the host vehicle starts again to move and it has been simulated that after few minutes (consider the geodetic position indicated by the

green circle in Figure 2.16) the GPS signal is definitely lost. Then the host vehicle travels for about 28 Km in 45 minutes.

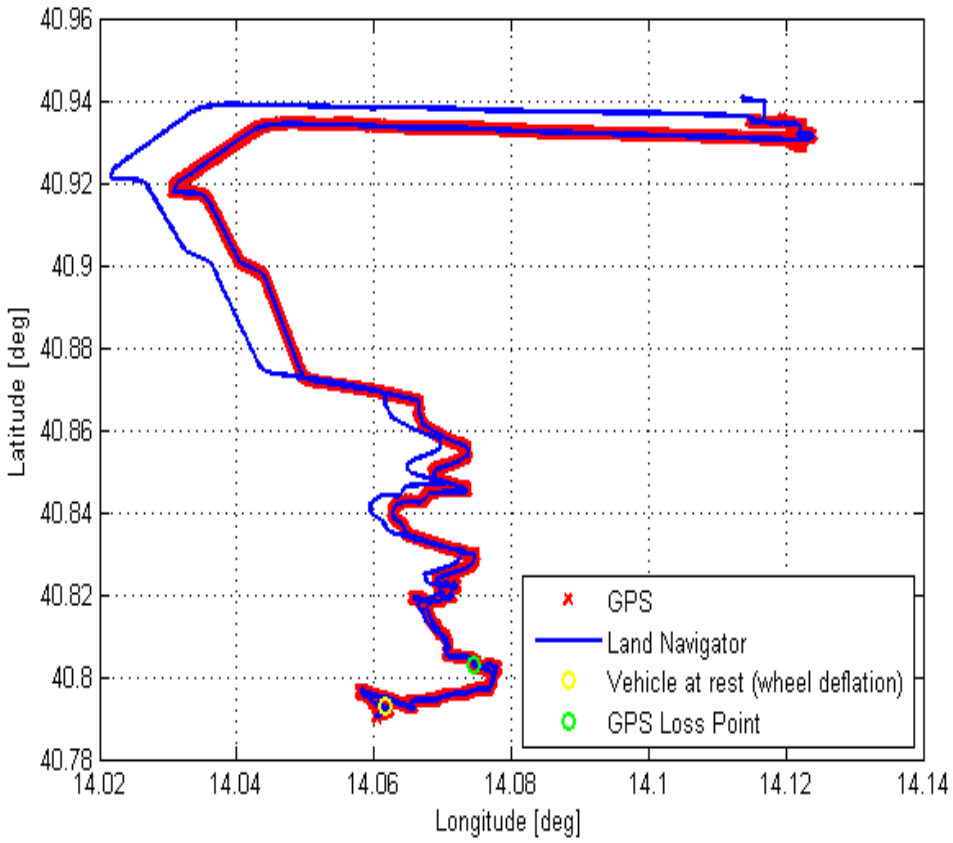

Figure 2.16 – PC Simulation: Geodetic Position comparison between AXD-LNS (blue) and GPS (red) when no scale factor correction is applied

From Figure 2.17 and Table 2.8 it is evident that requirement of a percentage error less than the 3% of the travelled distance without receiving the GPS signal is no longer satisfied.

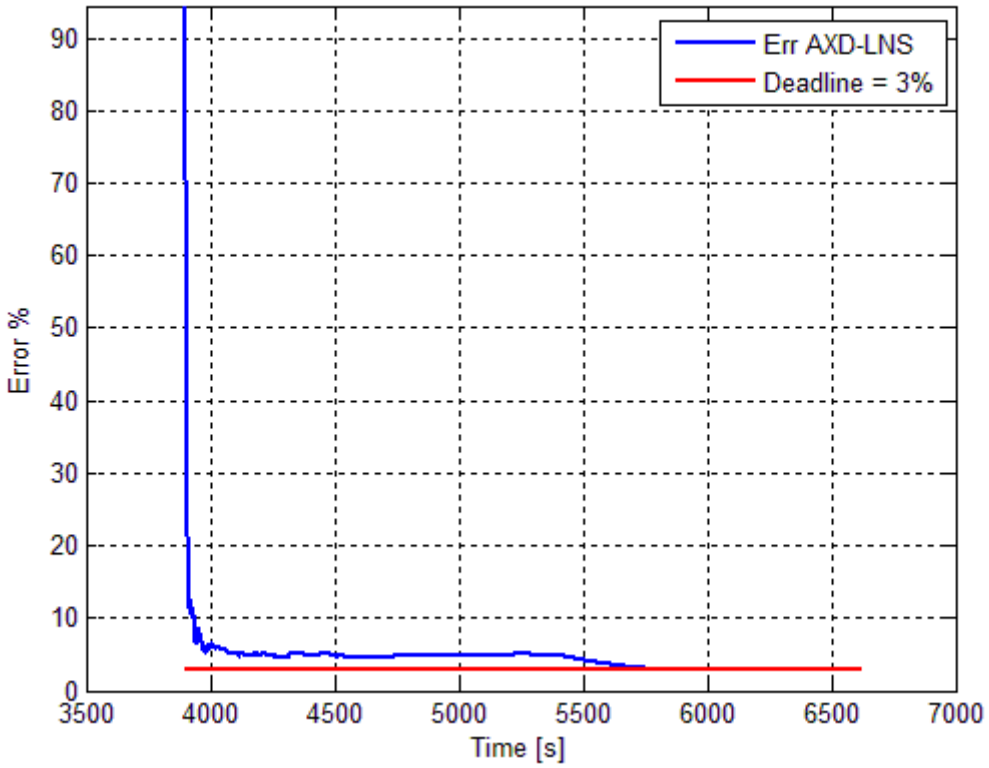

Figure 2.17 – PC Simulation: AXD-LNS Error % after GPS Loss Point when no scale factor correction is applied

Performances (without GPS for 28 Km in about 45 minutes)				
Err Max	Err Mean	Err Std	Err Rms	Err 1 σ
≈ 5.5 %	≈ 4 %	≈ 0.9 %	≈ 4.2 %	≈ 4.9 %

Table 2.8 – PC Simulation: AXD-LNS Performances when no scale factor correction is applied

Consider now the situation where the EKF is able to estimate an odometer scale factor error. Figure 2.18 shows the odometer scale factor estimated by the EKF: it is clear that as soon as the host vehicle starts again to move (around 3400 seconds) the EKF estimates in a few seconds a scale factor value of about 3.5% (remember that the odometer speed has been manually increased of a 4% from 3000 seconds to end).

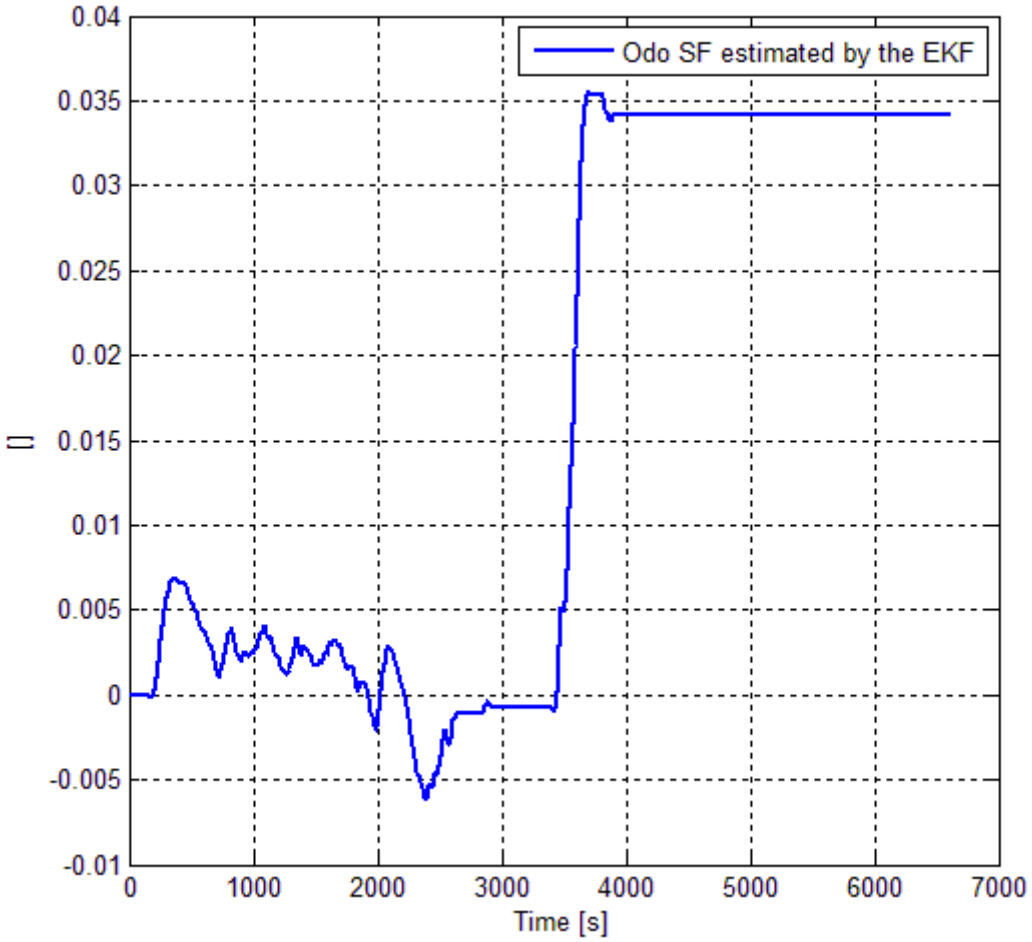

Figure 2.18 – PC Simulation: Odometer Scale Factor Error estimated by the EKF

Figure 2.19 compares the GPS output with the AXD-LNS solution when a scale factor correction is implemented in the EKF. It has been simulated to permanently lose the GPS signal in the same geodetic position (green circle) indicated in Figure 2.16. Finally, Figure 2.20 and Table 2.9 show that the requirement of a percentage error less than the 3% of the travelled distance without receiving the GPS signal is again satisfied. So a correct estimate of the scale factor has clearly a considerable influence on the AXD-LNS performances.

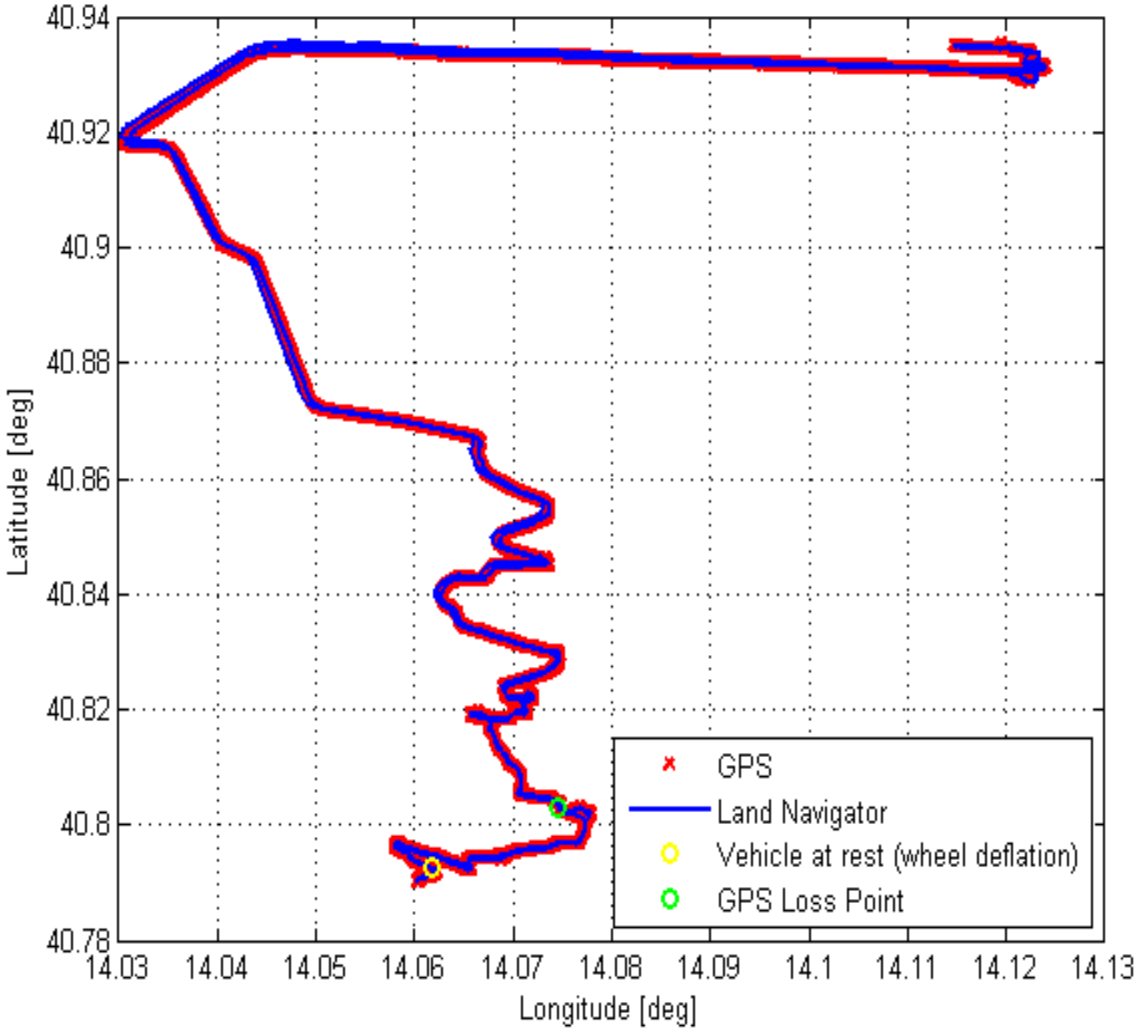

Figure 2.19 – PC Simulation: Geodetic Position comparison between AXD-LNS (blue) and GPS (red) when scale factor correction is applied

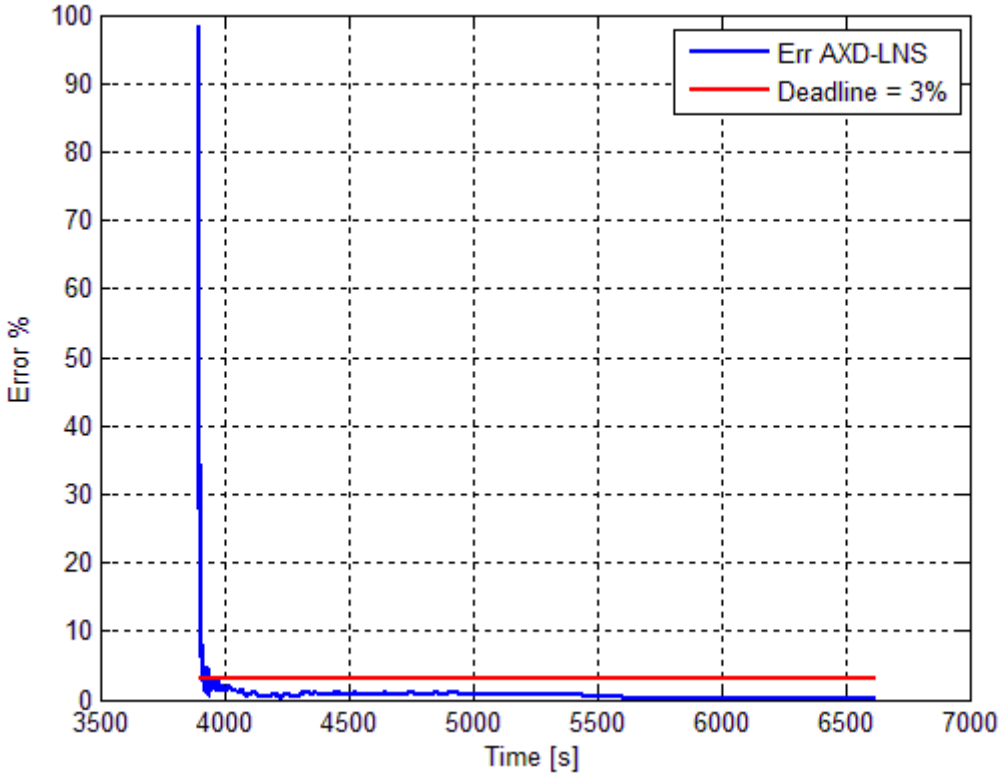

Figure 2.20 – PC Simulation: AXD-LNS Error % after GPS Loss Point when scale factor correction is applied

Performances (without GPS for 28 Km in about 45 minutes)				
Err Max	Err Mean	Err Std	Err Rms	Err 1 σ
< 1.3 %	< 0.6 %	< 0.3 %	< 0.7 %	< 0.9 %

Table 2.9 – PC Simulation: AXD-LNS Performances when scale factor correction is applied

2.5 Results and Conclusions

The availability and reliability of the PVT information in all environments has become a topic research theme for both military and civilian applications during the last years. As a consequence, this research activity has been focused also on developing a self-contained, dead-reckoning system for land applications with the following requirements:

- to compute a PVT solution at higher frequency than the typical GNSS output solution;
- to provide a geodetic position solution error less than the 3% of the travelled distance without receiving the GPS signal.

The AXD-LNS is the final result of this research activity. Previous in this chapter it has been exposed:

- the block diagram of the adopted SW model;
- the MEMS gyroscopes chosen for this application;
- the EKF algorithm implemented;
- the performance evaluation testing activities;
- two PC simulations to evaluate some EKF capabilities.

Table 2.10 summarizes the AXD-LNS overall performances.

AXD-LNS overall Performances				
Err Max	Err Mean	Err Std	Err Rms	Err 1 σ
< 2.0 %	< 0.8 %	< 0.4 %	< 0.9 %	< 1.2 %

Table 2.10 – AXD-LNS overall Performances

So the research requirements have been fully satisfied. Currently, due to its level of performances, the AXD-LNS system is being tested onboard Italian Army land vehicles.

Figure 2.21 – AXD-LNS system mounted on a military vehicle

Chapter 3

3.1 Alignment Applications Scenario

An INS provides a navigation solution output through a mathematical integration of the inertial sensor measurements. Each iteration of the navigation equations exploits the previous computed navigation solution as its starting point in order to calculate the next navigation solution, and so on. As a consequence, before an INS can provide a navigation solution, initial conditions must be determined [28].

Initial position and velocity are taken from an external input: INS position is usually initialized from another navigation system, such as another INS, GNSS or terrestrial radio navigation user equipment [29]. Alternatively, the INS may be placed near a pre-surveyed point, or could initialize its own position by taking range and/or bearing measurements to known landmarks. Where the host vehicle has not moved since the last time the INS was used, the last known position may be stored and used for initialization.

INS Velocity may be initialized simply by maintaining the host vehicle stationary with respect to the Earth or using as reference another navigation system, for example GNSS user equipment, Doppler radar, or another better quality INS.

Attitude (roll, pitch, and heading angles) may be initialized either from an external source or by sensing gravity and the Earth's rotation [30]. The procedure of determining the initial values of the attitude angles is also known as alignment because, in a platform INS, the inertial instruments are physically aligned with the axes of the local navigation frame. Scope of the initial alignment of a strapdown INS is to compute the elements of the rotation matrix from the body frame to the navigation frame and conduct the misalignment angles to zero or as negligible as possible. The initial misalignment is one of the major error sources of the strapdown INS [27], hence it is crucial to have an accurate initial alignment in order to provide an as much accurate navigation solution. For this reason, the initialization process is

often followed by a period of calibration when stationary or against an external reference, typically lasting a few minutes. This is known as fine alignment, as its main role is to reduce the attitude initialization errors. In many applications, it is also essential to achieve an accurate alignment of the strapdown INS within a very short period of time.

Low-cost MEMS IMUs usually embody inertial sensors with high levels of noise and poor bias stability characteristics, therefore it becomes necessary to develop specific algorithms in order to obtain the attitude information of the host vehicle.

Where the host vehicle is stationary, self-alignment shall be used to initialize INS attitude angles. Self-alignment involves a two-step process: a leveling step, which initializes the roll and pitch angles, and a gyrocompassing step, which initializes the heading. The leveling step is typically performed first.

Leveling is based on the consideration that, when the INS is stationary (or traveling at constant velocity), the only specific force sensed by the accelerometers is the reaction to gravity, which is approximately in the negative down direction of the local navigation frame at the Earth's surface. It is possible to demonstrate that roll and pitch angles may be initialized with a good accuracy even if using low quality accelerometers: a simple rule of the thumb states that 1 milli-g accurate accelerometers provide 1 milliradians (mrad) roll and pitch error [28]-[30].

Gyrocompassing is based on the principle that, when the INS is stationary (or traveling in a straight line in an inertial frame), the only rotation it senses is that of the Earth, which is in the z direction of the ECEF frame. Measuring this rotation in the body frame enables the heading to be determined, except at or very near to the poles, where the rotation axis and gravity vector coincide.

The low-cost IMUs usually use gyroscopes with noise levels larger than the Earth's rotation rate, and, as a consequence, they cannot be aligned in the static mode unless exploiting a device that provides reference heading measurements. Exploiting a magnetic compass is a very popular solution for many applications, such as land navigation [31]-[32], outdoor robotics [33], autonomous vehicle navigation [34]-[35],

human motion capture [36]. Another possibility is to transfer the obtained attitudes of another, statically aligned, better quality IMU through the master-slave initialization process [30]. In addition, the dynamic alignment can be performed through the velocity matching techniques by using the velocity updates from an aiding system such as the Differential Global Positioning System (DGPS) or the Doppler radar [37]-[38].

Moreover, a third research topic has been to develop and implement an innovative algorithm in order to accurately initialize a low-cost MEMS based IMU in a very short period of time.

This chapter is structured as here reported:

- first, the algorithm solution adopted to satisfy the above explained requirements, together with a schematic model and a detailed description of this algorithm will be illustrated;
- then it will be explained the testing strategy adopted to fully evaluate the initialization algorithm capabilities;
- finally, the main results of these testing activities will be exposed.

3.2 Adopted Solution for Fine Alignment Applications

After evaluating different solutions, a Zero Velocity Update (ZUPT) algorithm has been developed as fine alignment algorithm to initialize low-cost MEMS based INS. Figure 3.1 shows a block diagram model of the adopted ZUPT algorithm: after a brief coarse alignment phase the INS attitude and the PVT initial solutions are “frozen”, then the inertial navigation equations are numerically integrated but the upgraded attitude and PVT solutions are different from their initial values. Considering that the host vehicle is at rest and non-rotating, the changes in attitude and in the PVT solutions can be due only to uncompensated accelerometers and gyroscopes bias. So the ZUPT algorithm restore the initial attitude and PVT conditions and, in the meanwhile, estimates the inertial sensors bias until the INS indicates itself to be at rest and non-rotating.

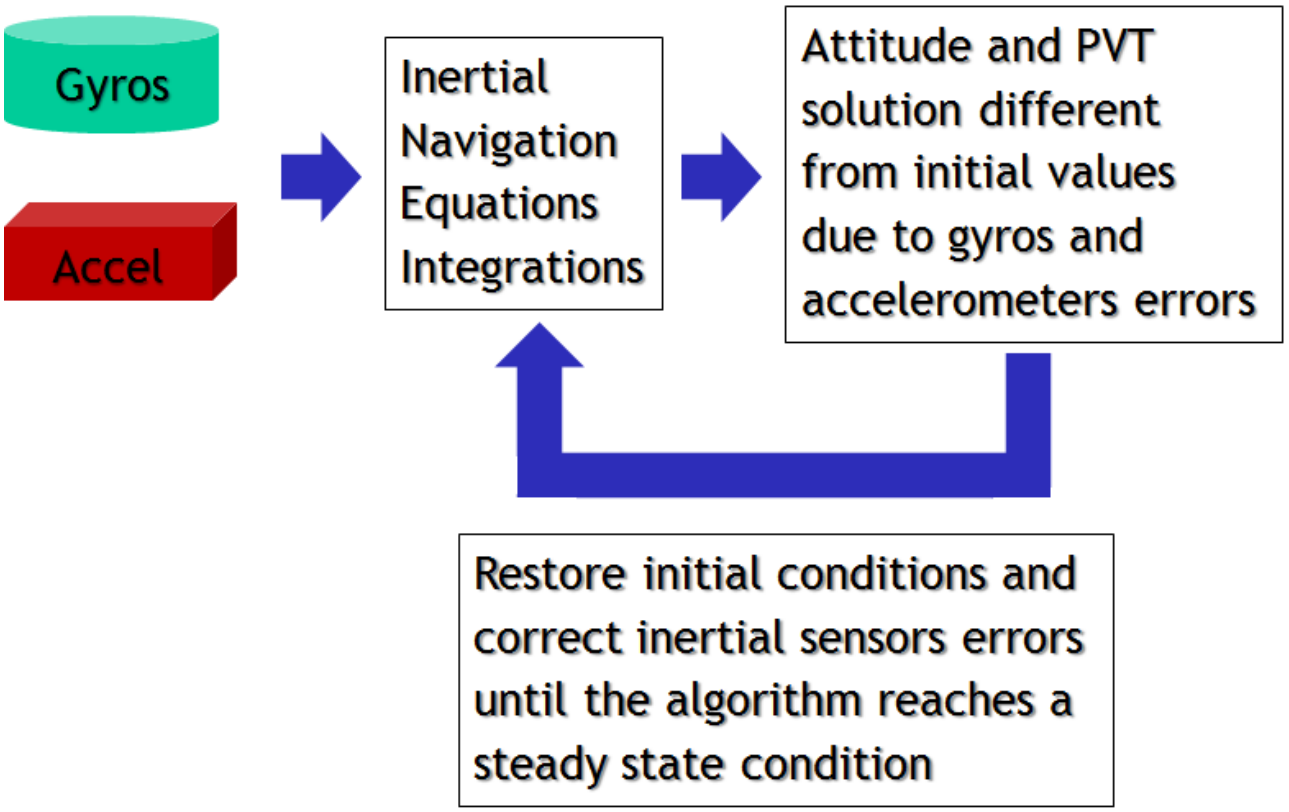

Figure 3.1 – ZUPT Block Diagram Model

ZUPT algorithm will be accurately described in the next section. For more details, consider [30].

3.3 ZUPT Algorithm Description

In this section it will be shown:

- a brief review of the mechanization equations, that will be simplified for ZUPT algorithm application;
- a brief review of the linear perturbation method to apply to the simplified version of the mechanization equations;
- a detailed description of the ZUPT algorithm, step for step.

3.3.1 Inertial Navigation Equation for ZUPT

The mechanization equations for the inertial navigation are:

$$\dot{\varphi} = \frac{V_N}{M+h}$$

3.1. $$\dot{\lambda} = \frac{V_E}{(N+h)\cos\varphi}$$

$$\dot{h} = -V_D$$

3.2. $$\dot{\vec{V}} = C_b^n \vec{f}_b - (2\vec{\omega}_{ie} + \vec{\omega}_{en}) \times \vec{V} + \vec{g}_l^n$$

3.3. $$\dot{q} = \frac{1}{2} q * (\omega_{ib} - C_n^b(\omega_{ie} + \omega_{en}))$$

The following definitions apply:

- $\vec{r} = [\varphi \quad \lambda \quad h]$ is the position vector in the WGS-84 ECEF frame in geodetic coordinates: φ is the latitude, λ is the longitude, h is the height above WGS-84 reference ellipsoid;
- $\vec{V} = [V_N \quad V_E \quad V_D]$ is the velocity vector of the system in local navigation frame which is the North-East-Down (NED) frame. The three components of the velocity vector will be the velocity in South-North direction (V_N), the West-East direction (V_E), the Up-Down direction (V_D);
- $\vec{q} = [q_0 \quad q_1 \quad q_2 \quad q_3]$ is the quaternion representation of the body attitude with respect to the NED frame;
- C_b^n is the direction cosine matrix from the body to the navigation frame function of the quaternion vector q :

$$C_b^n = \begin{bmatrix} q_0^2 + q_1^2 - q_2^2 - q_3^2 & 2(q_1q_2 + q_0q_3) & 2(q_1q_3 - q_0q_2) \\ 2(q_1q_2 - q_0q_3) & q_0^2 - q_1^2 + q_2^2 - q_3^2 & 2(q_2q_3 + q_0q_1) \\ 2(q_1q_3 + q_0q_2) & 2(q_2q_3 - q_0q_1) & q_0^2 - q_1^2 - q_2^2 + q_3^2 \end{bmatrix}^T$$

- The direction cosine matrix from the navigation frame to the body is $C_n^b = (C_b^n)^T$
- M and N are, respectively, the *meridian and traverse radii of curvature* in the Earth ellipsoid and are calculated as follows:

$$N = \frac{a}{\sqrt{1 - e^2 \sin^2 \varphi}}$$
$$M = \frac{a(1 - e^2)}{\sqrt{\left(1 - e^2 \sin^2 \varphi\right)^3}}$$

where *a* is the equatorial earth radius and *e* is the eccentricity of the Earth ellipsoid. Both values are based on the WGS-84 model.

- $\vec{\omega}_{ie}$ is Earth rate Ω resolved in the navigation frame:

$$\vec{\omega}_{ie} = \begin{bmatrix} \Omega \cos \varphi \\ 0 \\ -\Omega \sin \varphi \end{bmatrix}$$

- $\vec{\omega}_{en}$ is the transport rate of the navigation frame:

$$\vec{\omega}_{en} = \begin{bmatrix} \dot{\lambda} \cos \varphi \\ -\dot{\varphi} \\ -\dot{\lambda} \sin \varphi \end{bmatrix} = \begin{bmatrix} \frac{V_E}{(N+h)} \\ -\frac{V_N}{(M+h)} \\ -\frac{V_E \tan \varphi}{(N+h)} \end{bmatrix}$$

- The local gravity vector g_l^n includes the combine effects of the mass attraction of the Earth (***gravitational* vector** $\gamma(\varphi, h)$) and centripetal acceleration caused by Earth's rotation $\left(\omega_{ie} \times \omega_{ie} \times R\right)$ where $R = \sqrt{M \cdot N}$.

Hence, the gravity vector is:

$$g_l^n = \begin{bmatrix} 0 \\ 0 \\ \gamma(\varphi,h) \end{bmatrix} - \omega_{ie}^n \times \omega_{ie}^n \times \vec{R} = \begin{bmatrix} 0 \\ 0 \\ \gamma(\varphi,h) \end{bmatrix} - \Omega^2 (R_0 + h) \begin{bmatrix} \sin\varphi\cos\varphi \\ 0 \\ 1-\sin^2\varphi \end{bmatrix}$$

The WGS-84 gravity at the surface of the ellipsoid (Somigliana formula) is:

$$\gamma(\varphi,0) = \gamma_a \frac{1+k_\gamma \sin^2\varphi}{\sqrt{1-e^2\sin^2\varphi}} [m/s^2]$$

where

$k_\gamma = 0.00193185138639$
$e^2 = 0.00669437999013$
$\gamma_a = 9.7803267714 [m/s^2]$
$a = R_0 = 6378137.0$ [m]
$\Omega = 7.2922115146\text{e-}5$ [rad/s]

The WGS-84 gravity at height *h* from the surface of the ellipsoid is:

$$\gamma(\varphi,h) \cong \gamma(\varphi,0) + \frac{0.87}{10000} \exp\left(-0.116\left(\frac{h}{1000}\right)^{1.047}\right) \cong \gamma(\varphi,0)\left(\frac{1}{1+\frac{h}{\sqrt{M \cdot N}}}\right)$$

- $\vec{f}_b$ is the acceleration vector measured by the IMU in the body frame: these will be corrected with the stochastic accelerometers' bias estimated vector $\vec{b}_a = [b_{ax} b_{ay} b_{az}]^T$ estimated by the ZUPT algorithm.
- $\vec{\omega}_{ib}$ is the angular rate vector measured by the IMU in the body frame: these will be corrected with the stochastic gyroscopes' bias vector $\vec{b}_g = [b_{gx} b_{gy} b_{gz}]^T$ estimated by the ZUPT algorithm.

Taking in account that the ZUPT algorithm can be applied only when the host vehicle is stationary and non-rotating and that this algorithm has to last only few minutes, the transport terms can be neglected from the above explained mechanization equations. Hence, the simplified version of the mechanization equations for the ZUPT algorithm implementation is:

$$\dot{\varphi} = \frac{V_N}{M+h}$$

3.4. $$\dot{\lambda} = \frac{V_E}{(N+h)\cos\varphi}$$

$$\dot{h} = -V_D$$

3.5. $$\dot{\vec{V}} = C_b^n \vec{f}_b - 2\vec{\omega}_{ie} \times \vec{V} + \vec{g}_l^n$$

3.6. $$\dot{q} = \frac{1}{2} q * \left(\omega_{ib} - C_n^b \omega_{ie}\right)$$

3.3.2 Inertial Navigation Equation for ZUPT: Linear Perturbation Method

The linear perturbation method is applied to mechanization equations and the following perturbation equations apply, where the estimated variables are labeled with the 'hat' superscript.

The perturbation equation of the direction cosine matrix from the body to the navigation frame is:

3.7. $$C_b^n(\hat{q}) \equiv B(\delta q) C_b^n(q)$$

where q is the quaternion vector that represents the attitude of the body with respect to the true reference frame (NED), $\hat{q}$ is the quaternion vector that represents the

attitude of the body with respect to the estimated reference frame ($\hat{N}\hat{E}\hat{D}$) and $B(\delta q)$ is defined as the direction cosine matrix function of the quaternion error vector δq that rotates the true reference axes to the current estimated reference frame.

From Eqn. 3.7 we have:

3.8. $C_b^n(q) = B^{-1}(\delta q) C_b^n(\hat{q})$

Since $B(\cdot)$ has the properties of a direction cosine matrix: $B^{-1}(\delta q) = B(\delta q^{-1})$, and, hence,

3.9. $C_b^n(q) \equiv B(\delta q^{-1}) C_b^n(\hat{q})$

Using the equivalence of the quaternion multiplication $\otimes$ and direction cosine matrices: $q = \delta q^{-1} \otimes \hat{q}$, where the non-commutative multiplication of two quaternion q^a and q^b is defined as:

3.10. $$q^a \otimes q^b \equiv \begin{bmatrix} q_0^b & -q_1^b & -q_2^b & -q_3^b \\ q_1^b & q_0^b & q_3^b & -q_2^b \\ q_2^b & -q_3^b & q_0^b & q_1^b \\ q_3^b & q_2^b & -q_1^b & q_0^b \end{bmatrix} \begin{bmatrix} q_0^a \\ q_1^a \\ q_2^a \\ q_3^a \end{bmatrix}$$

and, the quaternion inverse q^{-1} (per normalized quaternion) is:

3.11. $$q^{-1} = [q_0 \quad -q_1 \quad -q_2 \quad -q_3]^T$$

If the small angle error model is applied:

3.12. $$\delta q \cong [1 \quad \varepsilon_N \quad \varepsilon_E \quad \varepsilon_D]^T$$

we have:

3.13. $$B(\delta q) \cong \left(I^{3x3} - E\right)$$

with

3.14. $$E = \begin{bmatrix} 0 & -\varepsilon_D & \varepsilon_E \\ \varepsilon_D & 0 & -\varepsilon_N \\ -\varepsilon_E & \varepsilon_N & 0 \end{bmatrix}$$

skew symmetric. Hence, Eqn. 3.7 transforms as:

3.15. $$\hat{C}_b^n \equiv \left(I^{3x3} - E\right) C_b^n$$

The perturbation equation of the position vector is:

3.16. $$\hat{\vec{r}} = \vec{r} + \delta\vec{r} \quad \text{with } \vec{r} \equiv \begin{bmatrix} \varphi \\ \lambda \\ h \end{bmatrix} \quad \text{and} \quad \delta\vec{r} = \begin{bmatrix} \delta\varphi \\ \delta\lambda \\ \delta h \end{bmatrix}$$

The perturbation equation of the velocity vector is:

3.17. $$\hat{\vec{V}} = \vec{V} + \delta\vec{v} \text{ with } \vec{V} \equiv \begin{bmatrix} V_N \\ V_E \\ V_D \end{bmatrix} \text{ and } \delta\vec{v} \equiv \begin{bmatrix} \delta V_N \\ \delta V_E \\ \delta V_D \end{bmatrix}$$

The error model for the acceleration is:

3.18. $$\hat{\vec{f}} \equiv \vec{f} + \delta\vec{f}$$

where the accelerometers errors $\delta\vec{f}$ are:

3.19. $$\delta\vec{f} = \vec{b}_a + \vec{\eta}_a$$

The accelerometers measurements noise $\vec{\eta}_a$ is modeled as a zero-mean Gaussian noise. The stochastic component of the accelerometers bias is $\vec{b}_a = \begin{bmatrix} b_{ax} & b_{ay} & b_{az} \end{bmatrix}$. The time model for the accelerometer bias is:

3.20. $$\dot{\vec{b}}_a(t) = \vec{\eta}_{ba}(t)$$

where $\vec{\eta}_{ba}(t)$ is a zero-mean Gaussian noise. The accelerometers bias is driven by random-walk process.

The error model for the angular rate is:

3.21. $$\hat{\vec{\omega}} \equiv \vec{\omega} + \delta\vec{\omega}$$

where the gyroscopes errors $\delta\vec{\omega}$ are

3.22. $$\delta\vec{\omega} = \vec{b}_g + \vec{\eta}_g$$

The gyroscopes measurements noise $\vec{\eta}_g$ is modeled as a zero-mean Gaussian noise. The stochastic component of the gyroscopes bias is $\vec{b}_g = \begin{bmatrix} b_{gx} & b_{gy} & b_{gz} \end{bmatrix}$. The time model for the gyroscopes bias is

3.23. $$\dot{\vec{b}}_g(t) = \vec{\eta}_{bg}(t)$$

where $\vec{\eta}_{bg}(t)$ is a zero-mean Gaussian noise. The gyroscopes bias is driven by a random-walk process.

With the above definitions, the following time-continuous error model is derived:

3.24. $$\dot{\delta x}(t) = F(t)\delta x(t) + G(t)\eta(t)$$

where the full 15-dimension augmented state error vector for the ZUPT algorithm is:

3.25. $$\delta x = [\delta\varphi \quad \delta\lambda \quad \delta h \quad \delta V_N \quad \delta V_E \quad \delta V_D \quad \varepsilon_N \quad \varepsilon_E \quad \varepsilon_D \quad \delta b_{ax} \quad \delta b_{ay} \quad \delta b_{az} \quad \delta b_{gx} \quad \delta b_{gy} \quad \delta b_{gz}]^T$$

while the system state vector is:

3.26. $$x = [\varphi \quad \lambda \quad h \quad V_N \quad V_E \quad V_D \quad q_0 \quad q_1 \quad q_2 \quad q_3 \quad b_{ax} \quad b_{ay} \quad b_{az} \quad b_{gx} \quad b_{gy} \quad b_{gz}]^T$$

The system noise covariance matrix is:

3.27. $$E[\eta(t)\eta^T(t')] = Q\delta(t-t')$$

The process noise vector is:

3.28. $$\eta(t) = \left[\vec{\eta}_a(t) \quad \vec{\eta}_g(t) \quad \vec{\eta}_{ba}(t) \quad \vec{\eta}_{bg}(t)\right]^T$$

The time-dependent process transition matrix $F(t)$ and the process noise matrix $G(t)$ are obtained deriving the equations

$$F(t) = \frac{\partial f(x,0)}{\partial x}\Big|x = \hat{x} \quad \text{and} \quad G(t) = \frac{\partial f(x,\eta)}{\partial \eta}\Big|x = \hat{x} \quad \text{where} \quad x = \left[\vec{r} \quad \vec{V} \quad q \quad \vec{b}_a \quad \vec{b}_g\right]$$

Hence,

3.29. $$F = \begin{bmatrix} F_{rr} & F_{rv} & 0_{3x3} & 0_{3x3} & 0_{3x3} \\ F_{vr} & F_{vv} & F_{v\varepsilon} & C_b^n & 0_{3x3} \\ F_{\varepsilon r} & 0_{3x3} & F_{\varepsilon\varepsilon} & 0_{3x3} & -C_b^n \\ 0_{3x3} & 0_{3x3} & 0_{3x3} & 0_{3x3} & 0_{3x3} \\ 0_{3x3} & 0_{3x3} & 0_{3x3} & 0_{3x3} & 0_{3x3} \end{bmatrix}$$

3.30. $$G = \begin{bmatrix} 0_{3x3} & 0_{3x3} & 0_{3x3} & 0_{3x3} \\ -C_b^n & 0_{3x3} & 0_{3x3} & 0_{3x3} \\ 0_{3x3} & C_b^n & 0_{3x3} & 0_{3x3} \\ 0_{3x3} & 0_{3x3} & I_{3x3} & 0_{3x3} \\ 0_{3x3} & 0_{3x3} & 0_{3x3} & I_{3x3} \end{bmatrix}$$

where 0_{3x3} is a 3x3 matrix filled with zeroes, I_{3x3} is a 3x3 identity matrix and C_b^n is the direction cosine matrix from the body to the navigation frame function of the quaternion vector currently estimated by the ZUPT algorithm. Also the following calculation applies:

3.31. $$F_{rr} \equiv \begin{bmatrix} \frac{\partial \dot{\varphi}}{\partial \varphi} & \frac{\partial \dot{\varphi}}{\partial \lambda} & \frac{\partial \dot{\varphi}}{\partial h} \\ \frac{\partial \dot{\lambda}}{\partial \varphi} & \frac{\partial \dot{\lambda}}{\partial \lambda} & \frac{\partial \dot{\lambda}}{\partial h} \\ \frac{\partial \dot{h}}{\partial \varphi} & \frac{\partial \dot{h}}{\partial \lambda} & \frac{\partial \dot{h}}{\partial h} \end{bmatrix} = \begin{bmatrix} 0 & 0 & -\frac{V_N}{(M+h)^2} \\ \frac{V_E \sin\varphi}{(N+h)\cos^2\varphi} & 0 & -\frac{V_E}{(N+h)^2\cos\varphi} \\ 0 & 0 & 0 \end{bmatrix}$$

3.32. $$F_{rv} \equiv \begin{bmatrix} \frac{\partial \dot{\varphi}}{\partial V_N} & \frac{\partial \dot{\varphi}}{\partial V_E} & \frac{\partial \dot{\varphi}}{\partial V_D} \\ \frac{\partial \dot{\lambda}}{\partial V_N} & \frac{\partial \dot{\lambda}}{\partial V_E} & \frac{\partial \dot{\lambda}}{\partial V_D} \\ \frac{\partial \dot{h}}{\partial V_N} & \frac{\partial \dot{h}}{\partial V_E} & \frac{\partial \dot{h}}{\partial V_D} \end{bmatrix} = \begin{bmatrix} \frac{1}{M+h} & 0 & 0 \\ 0 & \frac{1}{(N+h)\cos\varphi} & 0 \\ 0 & 0 & -1 \end{bmatrix}$$

3.33. $$F_{vr} \equiv \begin{bmatrix} \frac{\partial \dot{V}_N}{\partial \varphi} & \frac{\partial \dot{V}_N}{\partial \lambda} & \frac{\partial \dot{V}_N}{\partial h} \\ \frac{\partial \dot{V}_E}{\partial \varphi} & \frac{\partial \dot{V}_E}{\partial \lambda} & \frac{\partial \dot{V}_E}{\partial h} \\ \frac{\partial \dot{V}_D}{\partial \varphi} & \frac{\partial \dot{V}_D}{\partial \lambda} & \frac{\partial \dot{V}_D}{\partial h} \end{bmatrix} = \begin{bmatrix} -2\Omega\cos\varphi V_E & 0 & 0 \\ 2\Omega(-\sin\varphi V_D + \cos\varphi V_N) & 0 & 0 \\ +2\Omega\sin\varphi V_E & 0 & 0 \end{bmatrix}$$

3.34. $$F_{vv} \equiv \begin{bmatrix} \frac{\partial \dot{V}_N}{\partial V_N} & \frac{\partial \dot{V}_N}{\partial V_E} & \frac{\partial \dot{V}_N}{\partial V_D} \\ \frac{\partial \dot{V}_E}{\partial V_N} & \frac{\partial \dot{V}_E}{\partial V_E} & \frac{\partial \dot{V}_E}{\partial V_D} \\ \frac{\partial \dot{V}_D}{\partial V_N} & \frac{\partial \dot{V}_D}{\partial V_E} & \frac{\partial \dot{V}_D}{\partial V_D} \end{bmatrix} = \begin{bmatrix} 0 & -2\Omega\sin\varphi & 0 \\ 2\Omega\sin\varphi & 0 & 2\Omega\cos\varphi \\ 0 & -2\Omega\cos\varphi & 0 \end{bmatrix}$$

3.35. $$F_{v\varepsilon} \equiv \begin{bmatrix} \frac{\partial \dot{V}_N}{\partial \varepsilon_N} & \frac{\partial \dot{V}_N}{\partial \varepsilon_E} & \frac{\partial \dot{V}_N}{\partial \varepsilon_D} \\ \frac{\partial \dot{V}_E}{\partial \varepsilon_N} & \frac{\partial \dot{V}_E}{\partial \varepsilon_E} & \frac{\partial \dot{V}_E}{\partial \varepsilon_D} \\ \frac{\partial \dot{V}_D}{\partial \varepsilon_N} & \frac{\partial \dot{V}_D}{\partial \varepsilon_E} & \frac{\partial \dot{V}_D}{\partial \varepsilon_D} \end{bmatrix} = \begin{bmatrix} 0 & -f_D & f_E \\ f_D & 0 & -f_N \\ -f_E & f_N & 0 \end{bmatrix}$$

3.36. $$F_{\varepsilon r} \equiv \begin{bmatrix} \frac{\partial \dot{\varepsilon}_N}{\partial \varphi} & \frac{\partial \dot{\varepsilon}_N}{\partial \lambda} & \frac{\partial \dot{\varepsilon}_N}{\partial h} \\ \frac{\partial \dot{\varepsilon}_E}{\partial \varphi} & \frac{\partial \dot{\varepsilon}_E}{\partial \lambda} & \frac{\partial \dot{\varepsilon}_E}{\partial h} \\ \frac{\partial \dot{\varepsilon}_D}{\partial \varphi} & \frac{\partial \dot{\varepsilon}_D}{\partial \lambda} & \frac{\partial \dot{\varepsilon}_D}{\partial h} \end{bmatrix} \equiv \begin{bmatrix} -\Omega \sin\varphi & 0 & 0 \\ 0 & 0 & 0 \\ -\Omega \cos\varphi & 0 & 0 \end{bmatrix}$$

3.37. $$F_{\varepsilon\varepsilon} \equiv \begin{bmatrix} \frac{\partial \dot{\varepsilon}_N}{\partial \varepsilon_N} & \frac{\partial \dot{\varepsilon}_N}{\partial \varepsilon_E} & \frac{\partial \dot{\varepsilon}_N}{\partial \varepsilon_D} \\ \frac{\partial \dot{\varepsilon}_E}{\partial \varepsilon_N} & \frac{\partial \dot{\varepsilon}_E}{\partial \varepsilon_E} & \frac{\partial \dot{\varepsilon}_E}{\partial \varepsilon_D} \\ \frac{\partial \dot{\varepsilon}_D}{\partial \varepsilon_N} & \frac{\partial \dot{\varepsilon}_D}{\partial \varepsilon_E} & \frac{\partial \dot{\varepsilon}_D}{\partial \varepsilon_D} \end{bmatrix} = \begin{bmatrix} 0 & -\Omega \sin\varphi & 0 \\ \Omega \sin\varphi & 0 & \Omega \cos\varphi \\ 0 & -\Omega \cos\varphi & 0 \end{bmatrix}$$

3.3.3 ZUPT Initialization Step

Eqn. 3.26 represent the INS state vector that the ZUPT algorithm has to estimate:

$$x = [\varphi \quad \lambda \quad h \quad V_N \quad V_E \quad V_D \quad q_0 \quad q_1 \quad q_2 \quad q_3 \quad b_{ax} \quad b_{ay} \quad b_{az} \quad b_{gx} \quad b_{gy} \quad b_{gz}]^T$$

At the beginning of the ZUPT algorithm,

- the LLH position is provided by an external reference device, like a GPS receiver;
- the velocity components are set to zero (the host vehicle is at rest);
- roll and pitch angles are computed through a coarse levelling based on the accelerometers output, the heading angle is provided by an external input. Then it is very simple to convert these initial values in a quaternion representation through the following relations:

3.38. $$q_0 = \cos\left(\frac{Roll_{init}}{2}\right)\cos\left(\frac{Pitch_{init}}{2}\right)\cos\left(\frac{Head_{init}}{2}\right) + \sin\left(\frac{Roll_{init}}{2}\right)\sin\left(\frac{Pitch_{init}}{2}\right)\sin\left(\frac{Head_{init}}{2}\right)$$

3.39. $$q_1 = \sin\left(\frac{Roll_{init}}{2}\right)\cos\left(\frac{Pitch_{init}}{2}\right)\cos\left(\frac{Head_{init}}{2}\right) - \cos\left(\frac{Roll_{init}}{2}\right)\sin\left(\frac{Pitch_{init}}{2}\right)\sin\left(\frac{Head_{init}}{2}\right)$$

3.40. $$q_2 = \cos\left(\frac{Roll_{init}}{2}\right)\sin\left(\frac{Pitch_{init}}{2}\right)\cos\left(\frac{Head_{init}}{2}\right) + \sin\left(\frac{Roll_{init}}{2}\right)\cos\left(\frac{Pitch_{init}}{2}\right)\sin\left(\frac{Head_{init}}{2}\right)$$

3.41. $$q_3 = \cos\left(\frac{Roll_{init}}{2}\right)\cos\left(\frac{Pitch_{init}}{2}\right)\sin\left(\frac{Head_{init}}{2}\right) - \sin\left(\frac{Roll_{init}}{2}\right)\sin\left(\frac{Pitch_{init}}{2}\right)\cos\left(\frac{Head_{init}}{2}\right)$$

- the inertial sensors bias are all set to zero (because they are unknown).

Since the simplified mechanization equations and their linearized version have been shown, it is now possible to describe the ZUPT algorithm various steps.

3.3.4 ZUPT Predictor and Integrator Step

At the beginning of this step, first of all it is necessary to subtract from the gyroscope output the last computed bias and the Earth rate components projected along the NED reference frame using the last computed $\hat{C}_n^b$ matrix:

3.42. $$\begin{bmatrix} \hat{\omega}_{x\,k+1,k} \\ \hat{\omega}_{y\,k+1,k} \\ \hat{\omega}_{z\,k+1,k} \end{bmatrix} = \begin{bmatrix} \hat{\omega}_{xm} \\ \hat{\omega}_{ym} \\ \hat{\omega}_{zm} \end{bmatrix} - \begin{bmatrix} \hat{b}_{gx_{k+1,k}} \\ \hat{b}_{gy_{k+1,k}} \\ \hat{b}_{gz_{k+1,k}} \end{bmatrix} - \hat{C}_n^b \vec{\omega}_{ie}$$

Then, defining T_s as the inertial sensors sample time, Eqn. 3.6 can be numerically integrated

3.43. $$\hat{q}_{k+1,k} = \left[I_{4x4}\left(1 - \frac{T_s^2 \left\|\hat{\omega}_{k+1,k}\right\|^2}{8}\right) + \Omega(\hat{\omega}_{k+1,k})\left(\frac{T_s}{2} - \frac{T_s^3}{48}\left\|\hat{\omega}_{k+1,k}\right\|^2\right)\right]\hat{q}_k$$

with

3.44. $$\left\|\hat{\omega}_{k+1,k}\right\|^2 = \hat{\omega}^2_{x\,k+1,k} + \hat{\omega}^2_{y\,k+1,k} + \hat{\omega}^2_{z\,k+1,k}$$

and

3.45. $$\Omega(\hat{\omega}_{k+1,k}) = \begin{bmatrix} 0 & -\hat{\omega}_{x\,k+1,k} & -\hat{\omega}_{y\,k+1,k} & -\hat{\omega}_{z\,k+1,k} \\ \hat{\omega}_{x\,k+1,k} & 0 & \hat{\omega}_{z\,k+1,k} & -\hat{\omega}_{y\,k+1,k} \\ \hat{\omega}_{y\,k+1,k} & -\hat{\omega}_{z\,k+1,k} & 0 & \hat{\omega}_{x\,k+1,k} \\ \hat{\omega}_{z\,k+1,k} & \hat{\omega}_{y\,k+1,k} & -\hat{\omega}_{x\,k+1,k} & 0 \end{bmatrix}$$

The following step is to subtract from the accelerometer output the last computed bias:

3.46. $$\hat{\vec{f}}_b = \begin{bmatrix} \hat{f}_{x\,k+1,k} \\ \hat{f}_{y\,k+1,k} \\ \hat{f}_{z\,k+1,k} \end{bmatrix} = \begin{bmatrix} \hat{f}_{xm} \\ \hat{f}_{ym} \\ \hat{f}_{zm} \end{bmatrix} - \begin{bmatrix} \hat{b}_{axk+1,k} \\ \hat{b}_{ay_{k+1,k}} \\ \hat{b}_{azk+1,k} \end{bmatrix}$$

Then Eqn. 3.5 can be numerically integrated

3.47. $$\hat{\vec{V}}_{k+1,k} = \hat{\vec{V}}_{k,k} + \left(\hat{C}_b^n \hat{\vec{f}}_b - 2\vec{\omega}_{ie} \times \hat{\vec{V}}_{k,k} + \vec{g}_l^n\right)T_s$$

where $\hat{C}_b^n$ is computed from the updated and normalized quaternions (Eqn. 3.43). Since $\hat{\vec{V}}_{k+1,k}$ is now known, it is finally possible to numerically integrate Eqn. 3.4 in the following manner:

$$\hat{\varphi}_{k+1,k} = \hat{\varphi}_{k,k} + \frac{1}{2}\left(\frac{\hat{V}_{N_{k+1,k}}}{M + \hat{h}_{k,k}} + \frac{\hat{V}_{N_{k,k}}}{M + \hat{h}_{k,k}} \right) T_s$$

3.48. $$\hat{\lambda}_{k+1,k} = \hat{\lambda}_{k,k} + \frac{1}{2}\left(\frac{\hat{V}_{E_{k+1,k}}}{N + \hat{h}_{k,k}} + \frac{\hat{V}_{E_{k,k}}}{N + \hat{h}_{k,k}} \right) T_s$$

$$\hat{h}_{k+1,k} = \hat{h}_{k,k} + \frac{1}{2}\left(-\hat{V}_{D_{k+1,k}} - \hat{V}_{D_{k,k}} \right) T_s$$

At the end of the predictor and integrator step it is performed the propagation of the error state covariance matrix $P_{k,k}$

3.49. $$P_{k+1,k} = \Phi_k P_{k,k} \Phi_k^T + \Gamma_k = (I + F_k T_s) P_{k,k} (I + F_k T_s)^T + (G_k Q_k G_k^T) T_s$$

where I is the 15x15 identity matrix, F_k is the process discretized matrix (§ 3.3.2) and Q_k is the 12x12 covariance matrix of the process noise $\eta(t) = \left[\vec{\eta}_a(t) \quad \vec{\eta}_g(t) \quad \vec{\eta}_{ba}(t) \quad \vec{\eta}_{bg}(t) \right]^T$, whose elements are below defined.

The accelerometers noise statistics are:

3.50. $$Q_k(1,1) = Q_k(2,2) = Q_k(3,3) = \sigma_a^2$$

The gyroscopes noise statistics are:

3.51. $$Q_k(4,4) = Q_k(5,5) = Q_k(6,6) = \sigma_g^2$$

The accelerometers bias noise statistics are:

3.52. $$Q_k(7,7) = Q_k(8,8) = Q_k(9,9) = \sigma_{ba}^2$$

The gyroscopes bias noise statistics are:

3.53. $$Q_k(10,10) = Q_k(11,11) = Q_k(12,12) = \sigma_{bg}^2$$

The off-diagonal element of Q_k are zero (Q_k is a diagonal matrix). The diagonal element of Q_k shall be evaluated through an Allan Variance analysis.

3.3.5 ZUPT Corrector Step

Due to uncompensated inertial sensors' bias, the updated system state resulting from Eqns. 3.43, 3.47 and 3.48 will be different from the previous one. Hence, every second (that is 100 steps for this application) it is executed a state correction. After an easy conversion from updated quaternions (evaluated with Eqn. 3.43) to updated roll, pitch and heading angles, realized through the following relations (where *atan2* is the four-quadrant inverse tangent function and *asin* is the inverse sine function):

3.54. $$Roll_{k+1,k} = atan2\left(2(q_{0_{k+1,k}} q_{1_{k+1,k}} + q_{2_{k+1,k}} q_{3_{k+1,k}}), 1 - 2(q_{1_{k+1,k}}^2 + q_{2_{k+1,k}}^2)\right)$$

3.55. $$Pitch_{k+1,k} = -a\sin\left(2(q_{1_{k+1,k}} q_{3_{k+1,k}} - q_{0_{k+1,k}} q_{2_{k+1,k}})\right)$$

3.56. $$Heading_{k+1,k} = atan2\left(2(q_{1_{k+1,k}} q_{2_{k+1,k}} + q_{0_{k+1,k}} q_{3_{k+1,k}}), 1 - 2(q_{3_{k+1,k}}^2 + q_{2_{k+1,k}}^2)\right)$$

the measurement innovation shall be computed as difference between current estimated state vector value (with roll, pitch and heading instead of quaternions) and the initial estimated state vector values:

3.57. $$\nu_{k+1} = \begin{bmatrix} \varphi_{init} - \hat{\varphi}_{k+1,k} \\ \lambda_{init} - \hat{\lambda}_{k+1,k} \\ h_{init} - \hat{h}_{k+1,k} \\ -\hat{V}_{N_{k+1,k}} \\ -\hat{V}_{E_{k+1,k}} \\ -\hat{V}_{D_{k+1,k}} \\ Roll_{k+1,k} - Roll_{init} \\ Pitch_{k+1,k} - Pitch_{init} \\ Head_{k+1,k} - Head_{init} \end{bmatrix}$$

Then the Kalman gain matrix can be evaluated

3.58. $$K_{k+1} = P_{k+1,k}\left(H_k\right)^T\left(H_k P_{k+1,k}(H_k)^T + R_k\right)^{-1}$$

where H_k is the 9x9 identity matrix and R_k represents the measurement noise matrix. R_k is 9x9 a diagonal matrix, whose elements reflects the uncertainty in the initial state vector evaluation.

Hence the error covariance matrix can be updated according to:

3.59. $$P_{k+1,k+1} = (I - K_{k+1}H_k)P_{k+1,k}$$

and the state error vector may be updated with

3.60. $$\delta\hat{x}_{k+1} = K_{k+1}\vec{v}_{k+1}$$

where the full 15-dimension augmented state error vector for the ZUPT algorithm is:

$$\delta\hat{x}_{k+1} = \left[\delta\varphi_{k+1} \quad \delta\lambda_{k+1} \quad \delta h_{k+1} \quad \delta\hat{\vec{V}}_{k+1} \quad \varepsilon_{N_{k+1}} \quad \varepsilon_{Ek+1} \quad \varepsilon_{D_{k+1}} \quad \delta\hat{\vec{b}}_{a_{k+1}} \quad \delta\hat{\vec{b}}_{g_{k+1}}\right]^T$$

The final step is to update the state vector:

- The position error vector $\delta\vec{r}_{k+1} = \delta\hat{x}_{k+1}\big|_{1,2,3} = \left[\delta\varphi_{k+1} \quad \delta\lambda_{k+1} \quad \delta h_{k+1}\right]$ made of geodetic latitude $\delta\lambda_{k+1}$ error, the geodetic longitude $\delta\lambda_{k+1}$ error and height δh_{k+1} is feedback to the system:

3.61. $$\hat{\varphi}_{k+1,k+1} = \hat{\varphi}_{k+1,k} + \delta\varphi_{k+1}$$

3.62. $$\hat{\lambda}_{k+1,k+1} = \hat{\lambda}_{k+1,k} + \delta\lambda_{k+1}$$

3.63. $$\hat{h}_{k+1,k+1} = \hat{h}_{k+1,k} + \delta h_{k+1}$$

- The velocity error vector $\delta\vec{v}_{k+1} = \delta\hat{x}_{k+1}\big|_{4,5,6} = \left[\delta\hat{V}_{N_{k+1}} \quad \delta\hat{V}_{E_{k+1}} \quad \delta\hat{V}_{D_{k+1}}\right]^T$ is directly feedback to the system in a single step:

3.64. $\hat{\vec{V}}_{k+1,k+1} = \hat{\vec{V}}_{k+1,k} + \delta\hat{\vec{V}}_{k+1}$

- The attitude error vector $\delta\vec{\varepsilon}_{k+1} = \delta\hat{x}_{k+1}\big|_{7,8,9} = \begin{bmatrix}\delta\varepsilon_{N_{k+1}} & \delta\varepsilon_{E_{k+1}} & \delta\varepsilon_{D_{k+1}}\end{bmatrix}$ is directly feedback to the system attitude quaternion vector in a single rotation step:

3.65. $\hat{q}_{k+1,k+1} = \delta\hat{q}_{k+1}^{-1} \otimes \hat{q}_{k+1,k}$

where $\otimes$ is the quaternion multiplication operator and

$$\delta\hat{q}_{k+1}^{-1} \equiv \begin{bmatrix} \cos\left(\frac{\varepsilon}{2}\right) \\ -\frac{\delta\varepsilon_{N_{k+1}}}{\varepsilon}\sin\left(\frac{\varepsilon}{2}\right) \\ -\frac{\delta\varepsilon_{E_{k+1}}}{\varepsilon}\sin\left(\frac{\varepsilon}{2}\right) \\ -\frac{\delta\varepsilon_{D_{k+1}}}{\varepsilon}\sin\left(\frac{\varepsilon}{2}\right) \end{bmatrix}$$

$$\varepsilon \equiv \sqrt{\left(\delta\varepsilon_{N_{k+1}}\right)^2 + \left(\delta\varepsilon_{E_{k+1}}\right)^2 + \left(\delta\varepsilon_{D_{k+1}}\right)^2}$$

- The gyroscopes bias error $\delta\hat{\vec{b}}_{g_{k+1}} = \delta\hat{x}_{k+1}\big|_{13,14,15}$ and accelerometers bias error $\delta\hat{\vec{b}}_{a_{k+1}} = \delta\hat{x}_{k+1}\big|_{10,11,12}$ are directly feedback to the system biases:

3.66. $\hat{\vec{b}}_{ak+1,k+1} = \hat{\vec{b}}_{ak+1,k} + \delta\hat{\vec{b}}_{ak+1}$

3.67. $\hat{\vec{b}}_{g_{k+1,k+1}} = \hat{\vec{b}}_{g_{k+1,k}} + \delta\hat{\vec{b}}_{g_{k+1}}$

3.4 ZUPT Testing Activities

The Axitude AX1-GNS5 system is a GPS-aided MEMS-based INS for high-g dynamics applications and, as the AX1-GNS3 product, it is provided of MEMS industrial-grade gyroscopes and accelerometers.

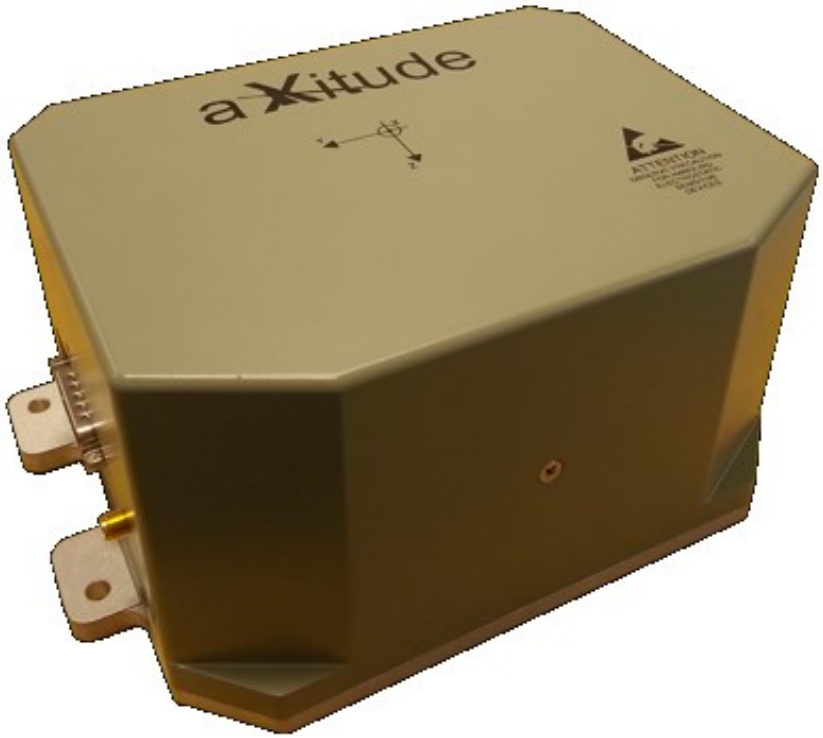

Figure 3.2 – AX1-GNS5 system

AX1-GNS5 is provided of an integrated GPS receiver (unlike AX1-GNS3 product), it is magnetometer-less and it utilizes the ZUPT algorithm described in the previous section § 3.3 as fine alignment algorithm. As a consequence, AX1-GNS5 testing activities included the ZUPT algorithm performances evaluation: hence, the AX1-GNS5 has been mounted on a rate table at different positions (consider the following Figure 3.3 and 3.4) to evaluate its output and its time of convergence.

Figure 3.3 – AX1-GNS5 system mounted on the rate table

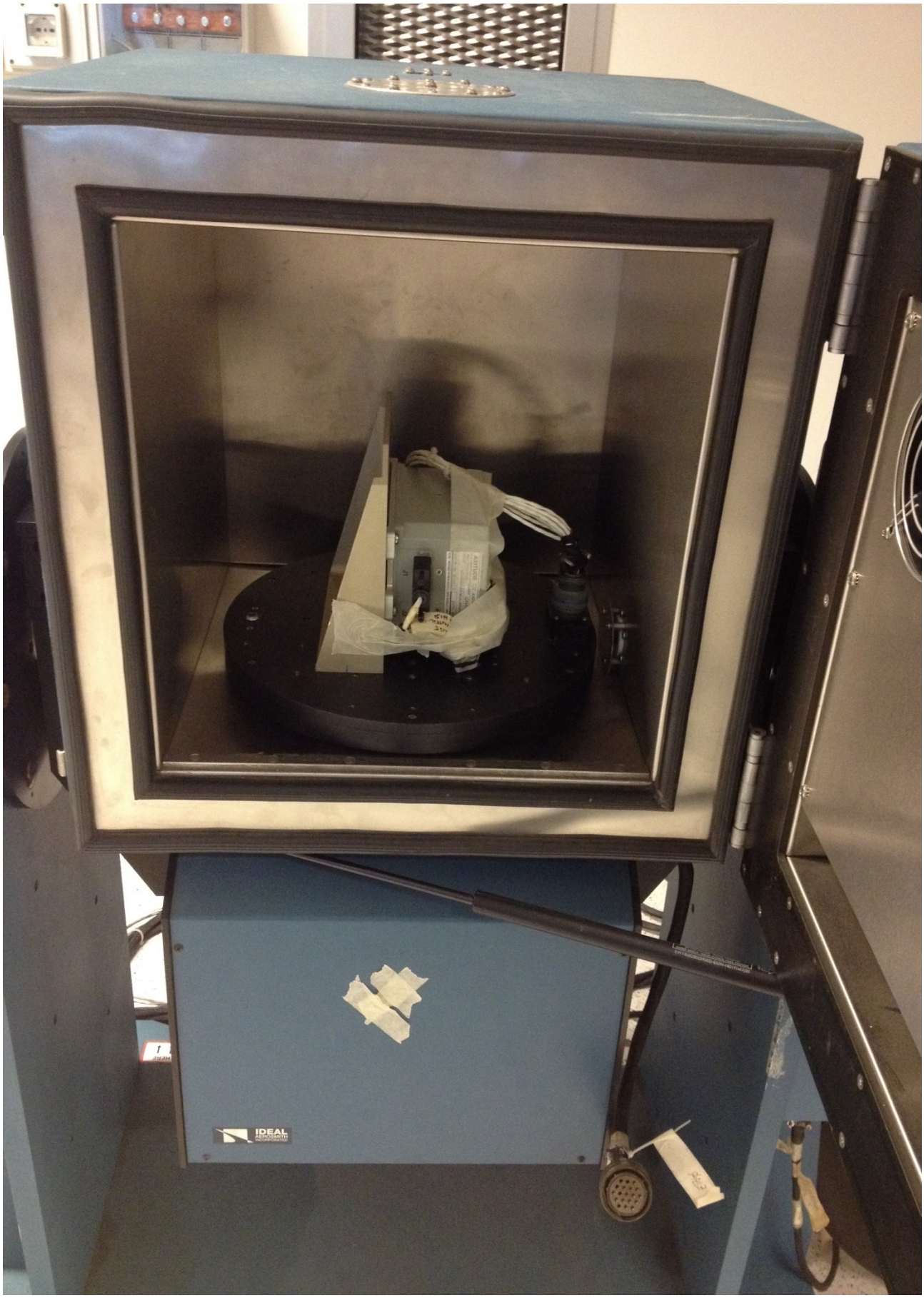

Figure 3.4 – AX1-GNS5 system mounted on the rate table (other position)

3.5 ZUPT Testing Results

The following figures report an example of the ZUPT output as it was collected after one of several carried out field tests. In more details, in this test the AX1-GNS5 was mounted in a levelled configuration on the rate table and roughly aligned towards the geographic north: hence a zero degree heading angle is provided as input for the AX1-GNS5 system. Then the integrated GPS receiver was connected to an external GPS antenna and the AX1-GNS5 system was linked to a Test Interface PC, as shown in Figure 3.5.

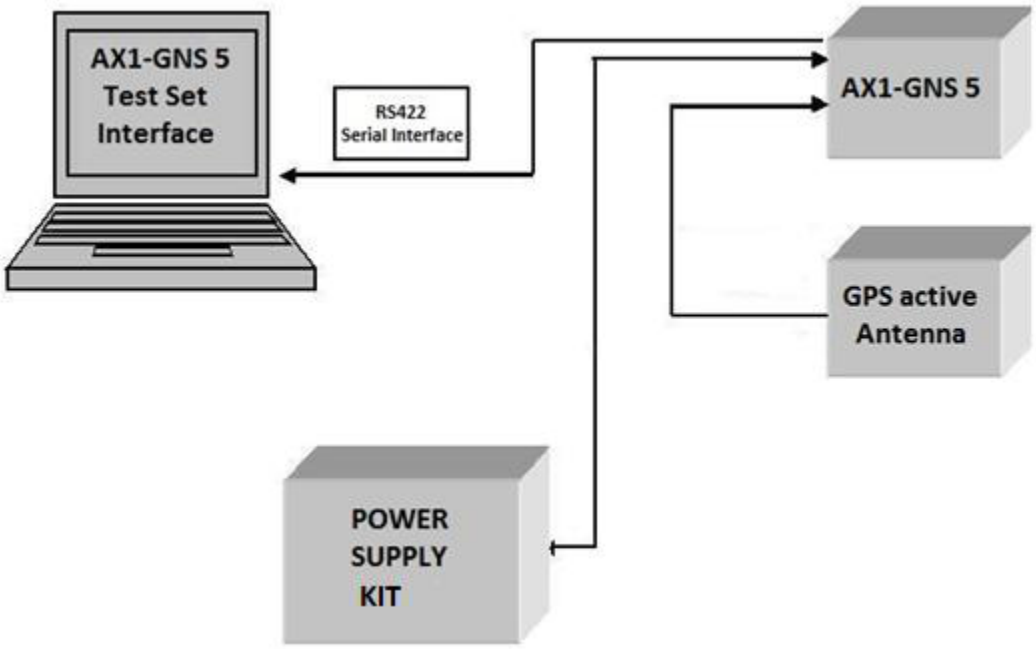

Figure 3.5 – AX1-GNS5 Test Equipment Configuration

Figure 3.6 reports the roll, pitch and heading angles in degrees as estimated by the ZUPT algorithm. Since at the beginning of the algorithm the gyroscopes bias are unknown, the mechanization equations integration provides an attitude output that tends to move away from its initial conditions. But, as soon as the ZUPT algorithm

- estimates the gyroscopes bias;
- subtracts these estimates from the gyroscopes output;
- and the estimated bias tend to the “real” bias values

the roll, pitch and heading angles computed by the ZUPT algorithm tend to converge to their initial values, and this convergence happens in less than a minute.

Figure 3.7 shows the gyroscopes bias in radians per second estimated by the ZUPT algorithm. These bias start from a zero value and rapidly converge to quasi-stationary values that are of a magnitude order of 10^{-2},10^{-3} radians per second, typical values for industrial-grade gyroscopes.

Figure 3.8 depicts the geodetic position as provided by the AX1-GNS5 during the initialization phase. Latitude and Longitude are expressed in degrees, WGS-84 altitude in meters. Figure 3.9 reports the linear velocity components in meters per second projected in the NED reference frame, as estimated by the ZUPT algorithm. From these two figures it is clear that, at the beginning of the algorithm, due to uncompensated inertial sensors errors, the AX1-GNS5 refers that it is moving from its initial position. As soon as the ZUPT algorithm

- estimates the inertial sensors bias;
- subtracts these estimates from the gyroscopes and accelerometers output;
- and the estimated bias tend to the “real” bias values

the AX1-GNS5 refers that it is at rest: after less than two minutes the NED velocity components estimated by the ZUPT algorithm are practically zero and, as a consequence, the LLH geodetic position remains constant with time.

Figure 3.10 shows the accelerometers bias in milli-g estimated by the ZUPT algorithm. These bias start from a zero value and in less than two minutes converge to quasi-stationary values that are of a milli-g magnitude order, as expected for industrial-grade accelerometers.

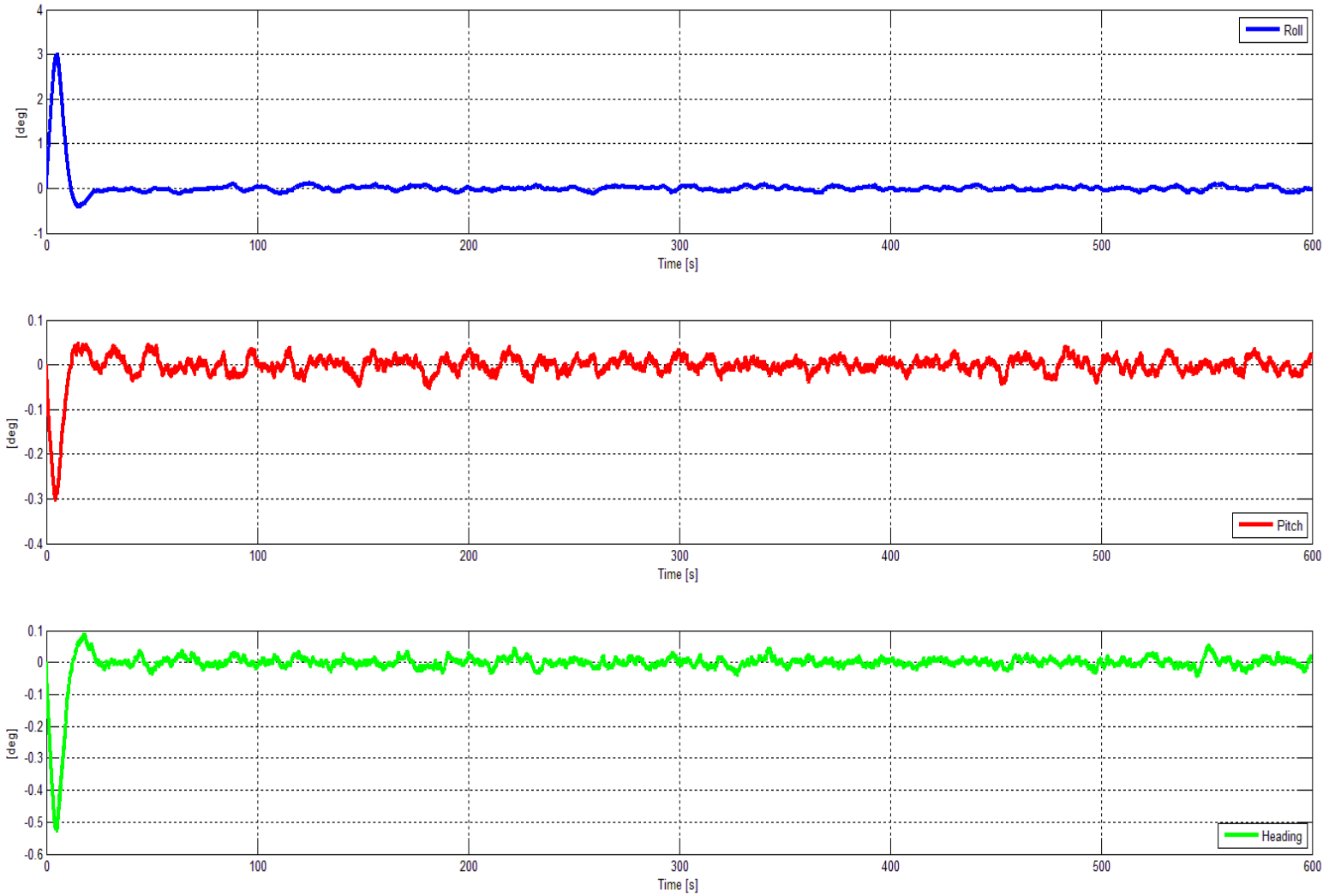

Figure 3.6 – Roll, Pitch and Heading angles estimated by the ZUPT algorithm

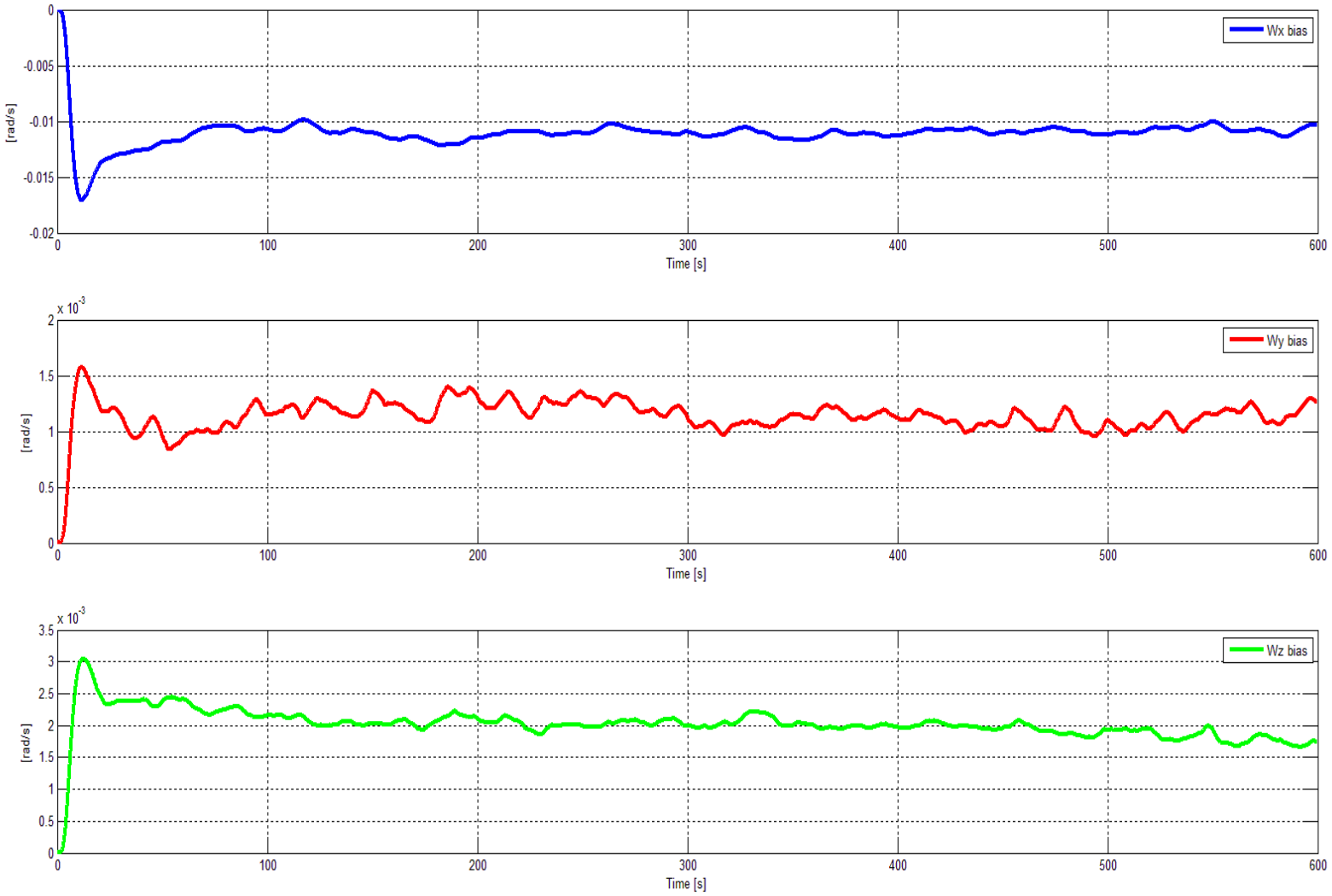

Figure 3.7 – Gyroscopes bias estimated by the ZUPT algorithm

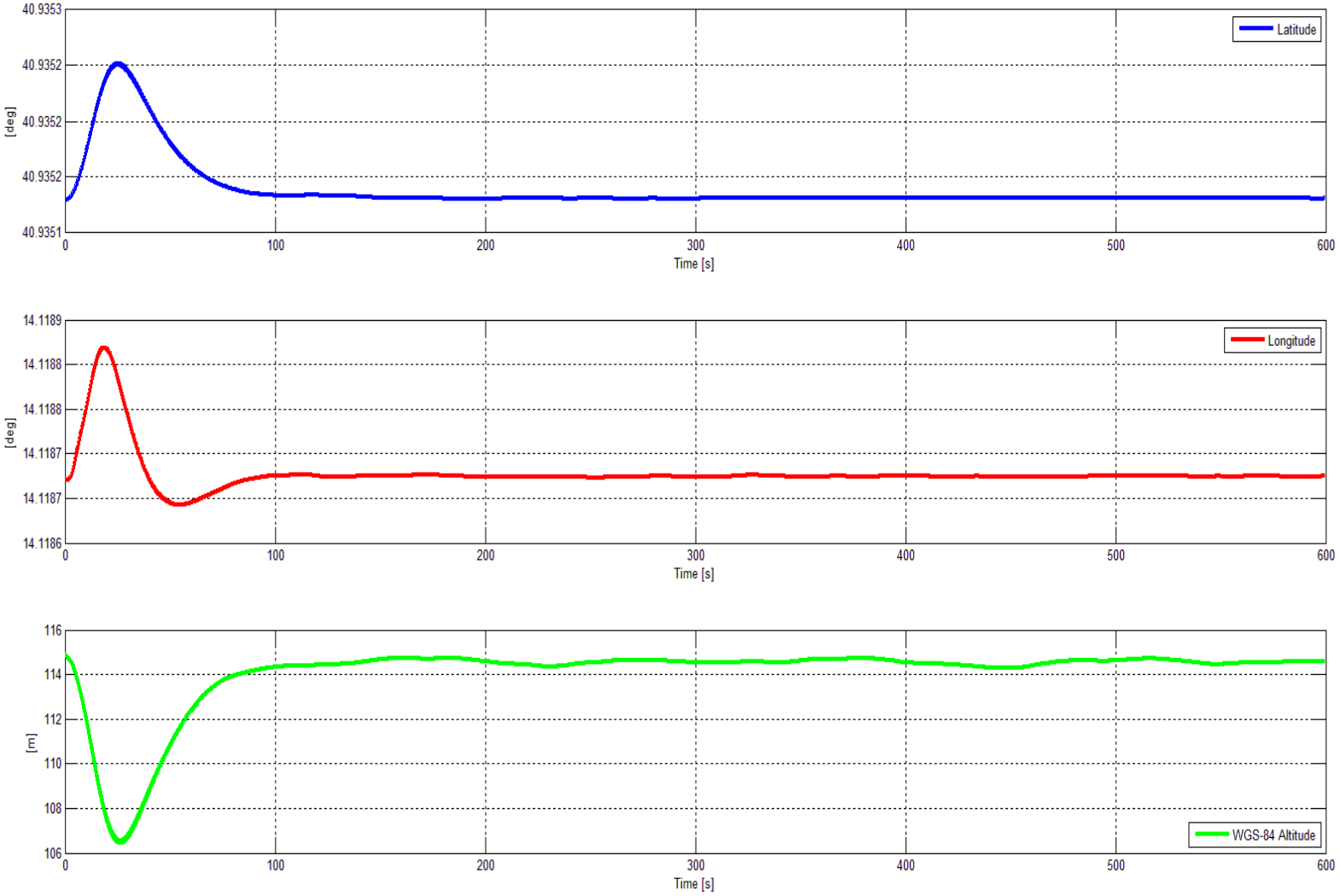

Figure 3.8 – LLH Geodetic Position estimated by the ZUPT algorithm

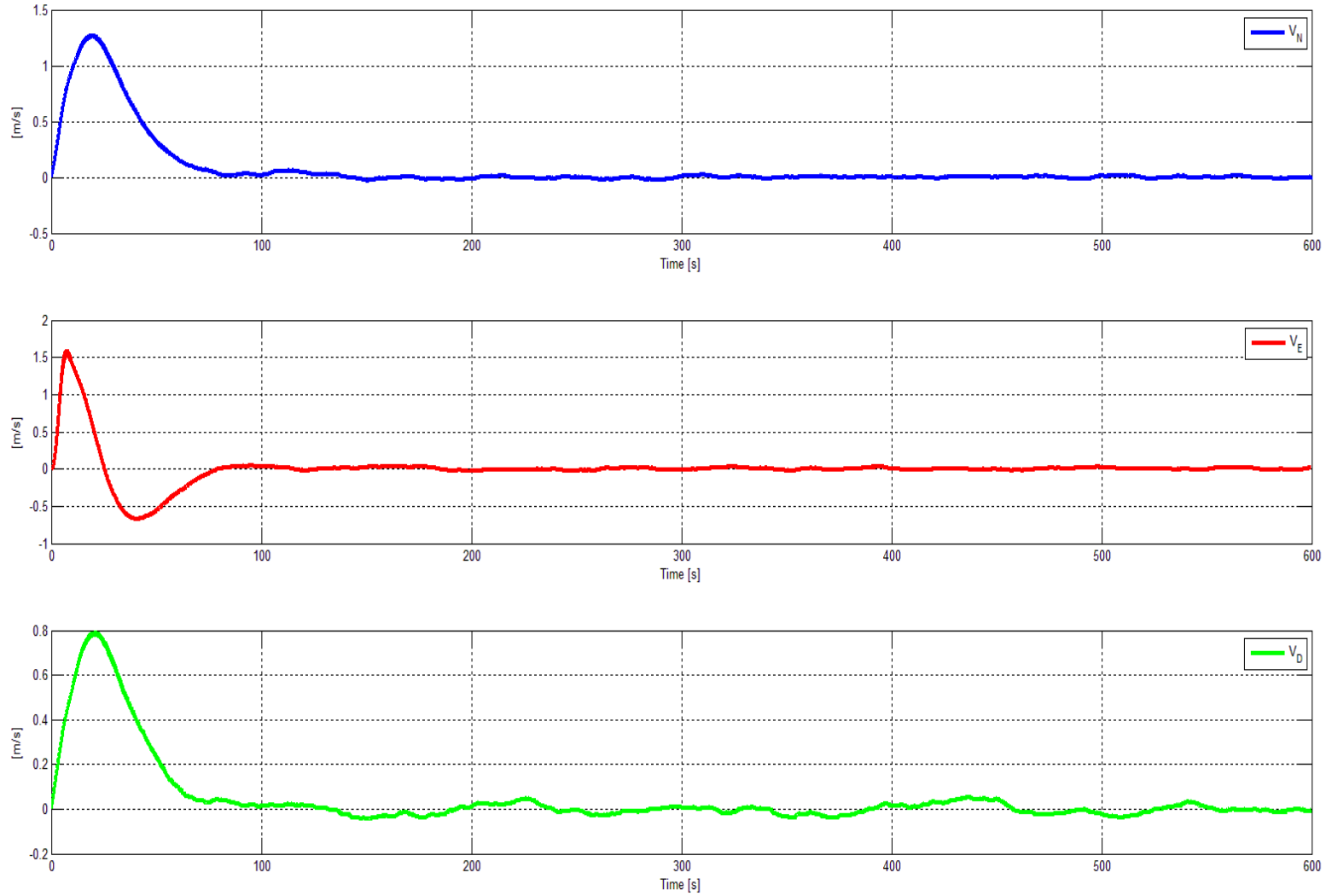

Figure 3.9 – NED Velocity components estimated by the ZUPT algorithm

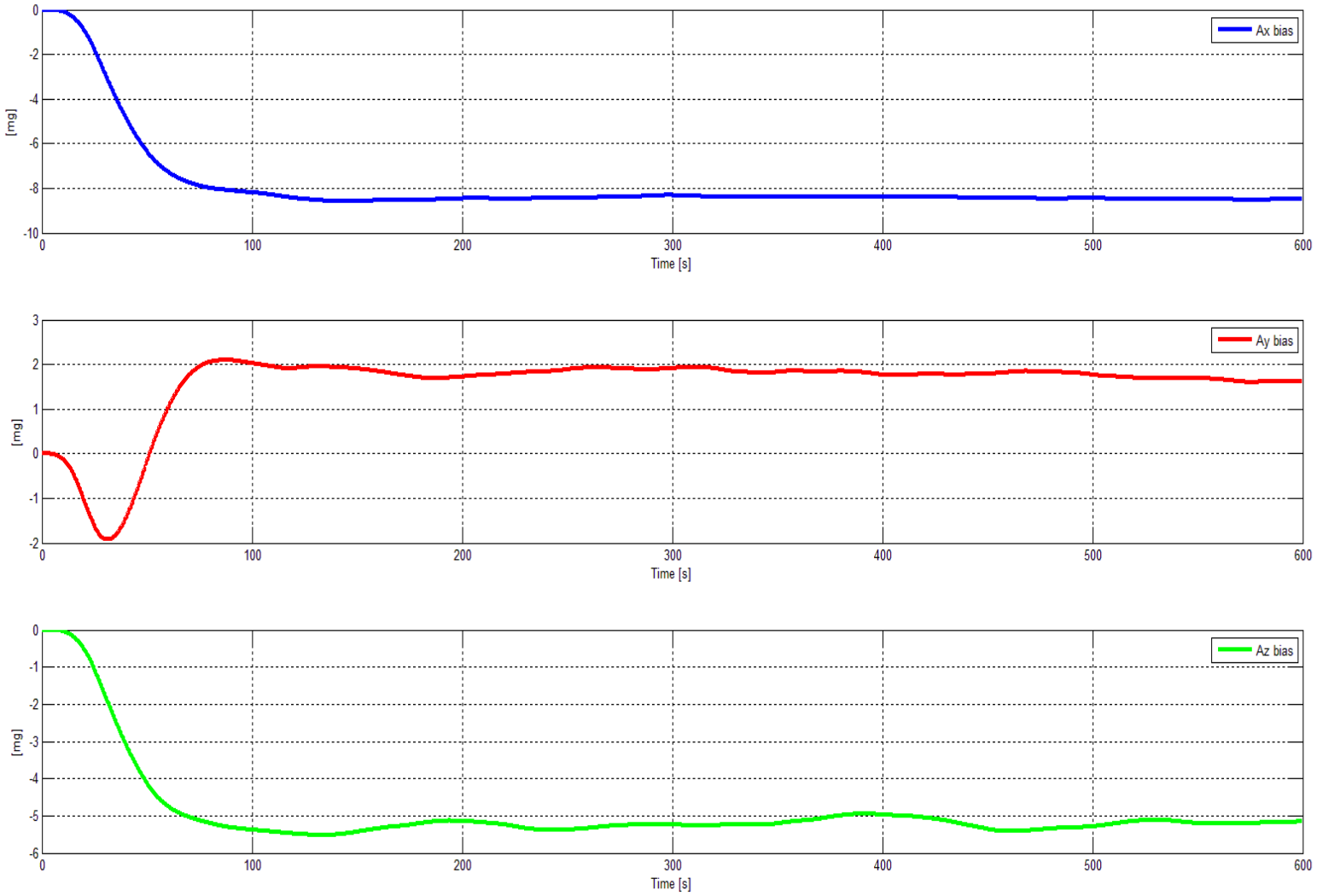

Figure 3.10 – Accelerometers bias estimated by the ZUPT algorithm

3.6 ZUPT Conclusions: Pros/Cons

ZUPT algorithm has been successfully tested, demonstrating to be able to provide an accurate initialization solution in a very short alignment time. This capability, joined with the AX1-GNS5 performances into providing an accurate navigation output, makes this INS suitable to be utilized in harsh scenarios, such as high-g dynamics applications. Currently, the AX1-GNS5 system is used on-board the Mirach-100, the integrated aerial target system designed and manufactured by Selex ES company to train and qualify worldwide Armed Forces major weapon systems.

Figure 3.11 – Mirach-100 missile target drone developed by SELEX-ES™

The Axitude AX1-GNS3 system exploits a magnetometer and gravity aiding as reference output to initialize roll, pitch and heading angles, together with the gyroscopes bias. In comparison, the ZUPT algorithm has the following advantages:

- also accelerometers bias are estimated;

- no gravity aiding is required: the accelerometers are used only for roll and pitch coarse estimation and in the predictor/integrator step, not in the measurement update step, as in the AX1-GNS3 product;
- no magnetometer is required: since it is largely influenced by external interferences and it is helpful only in the alignment phase but practically unused during the navigation phase, it is preferable to develop magnetometer-less configurations and initialize the heading angle in a different way than measuring the Earth magnetic field.

The main ZUPT algorithm drawback is the need for an external input to set the initial heading angle value. As a consequence, the reported research activity has been focused on the development of MEMS-based north-finding techniques, as illustrated in the next chapter.

Chapter 4

4.1 North-finding Applications Scenario

In the last years there has been an ever increasing need for devices able to north-finding with milliradian (mrad) uncertainty in a short alignment time and north-seeking in a wide dynamic range for applications such as inertial navigation or stabilization, pointing, tracking and guidance of remote operated devices [39]-[40]. North identification is typically obtained or measuring the Earth magnetic field or observing the Earth rotation rate (operation referred as gyrocompassing). In the first case, digital magnetic compasses (DCMs) are usually adopted and their current versions are compact, low-cost and demonstrates sub-degree accuracies capabilities [41], but spatial and temporal distortions in the Earth magnetic field and electromagnetic interferences can easily degrade these performances. In contrast gyrocompassing is unaffected by such factors, but mrad or sub-mrad commercial available systems based on Fiber Optical Gyros (FOGs), Ring Laser Gyros (RLGs) and Dynamically Tuned Gyros (DTGs) are generally heavy, bulky, quite expensive and power requiring: these drawbacks make such systems not suitable for man-portable and small-platform applications [42]. MEMS technology, conversely, have a number of inherent benefits: they are light-weight, low-power consumption, batch-fabricated, compact and low-cost, but gyrocompassing requires repeatable and stable measurements of extremely low angular rates (fractions of the Earth's rate). Moreover, even if MEMS gyroscopes capability to measure Earth's rate has been demonstrated [43]-[44], MEMS technology has not been considered for many years suitable to be employed in high-precision applications [45] due to accuracies far away from 1 mrad. Recently the scenario is changed due to hardware and architectural improvements: many researchers have reported silicon MEMS gyroscopes with less than 1 °/hr Allan deviation bias instability (consider [46] to [51]). However, some form of bias compensation, such as carouseling [52]-[53] or

maytagging [43]-[50]-[54], or some bias mitigation technique, for example redundant gyroscope configurations [55], are still required if the target remains a north-finding system with 1 milliradian accuracy in a short alignment time.

In the remainder of this chapter the description of research activities aimed at developing a MEMS-based device able to demonstrate north-finding performances comparable with FOGs, RLGs and DTGs is illustrated.

In more details:

- the adopted methods and gyroscopes are explained;
- the lab testing activities are described;
- finally, the testing activities results are exposed.

4.2 Adopted Methods and HW Solutions

MEMS gyroscopes exhibit substantial long-term bias drift, turn-on to turn-on bias shift, and bias variation over temperature. Due to these errors, as mentioned previously some form of bias compensation or mitigation is required to be suitable MEMS gyroscopes for north-finding applications.

Carouseling is a compensation technique that can significantly reduce the effect of bias on heading computation error [52]-[53]: the gyroscope is rigidly fixed on a rotating platform whose axis is parallel to the local Earth's vertical. When the gyroscope input axis is oriented horizontally and the platform rotates continuously, if the carouseling frequency is substantially faster than the time scale of the bias variation it is reasonable to consider the gyroscope bias errors sufficiently stable within a lap, hence the gyroscope output signal varies as a harmonic sine function. The amplitude of the sine is a reading of the horizontal Earth's rate angular rotation and its phase is a measure of the heading to the Earth's True North. Three are the main advantages of the carouseling method: it is not affected by thermal drift, allows a full gyroscope bias nulling and is not affected by scale factor errors. The main drawback consists in the realization and qualification of a complex rotation system.

Maytagging method is a variant of carouseling. It is a true north detection method accomplished by the ±180° turning of the gyroscope sensitive axis.
The system is initially set to an arbitrary azimuth angle ψ, and then rotated to 180° in either clockwise or counterclockwise direction. Taking into account that $\cos(\psi + 180°) = -\cos\psi$, the measurements of a gyroscope aligned to the local vertical level during maytagging in the ideal case are:

4.1. $S_x m_1 = \Omega_e \cos\psi \cos\varphi + b_x$

4.2. $S_x m_2 = -\Omega_e \cos\psi \cos\varphi + b_x$

where Ω_e is the Earth's rotation rate, φ is the latitude angle, ψ is the azimuth angle, m_1 and m_2 are the gyroscope output in its initial position and after the 180° turn, S_x and b_x are the gyroscope scale factor and bias errors (supposed constant during maytagging). Hence summing Eqns. 4.1 and 4.2 it is possible to observe the common bias value, while the azimuth is computed subtracting the same equations:

4.3. $\psi = \cos^{-1} \frac{S_x(m_1 - m_2)}{2\Omega_e \cos\varphi}$

The arccosine function ranges between 0° and 180°, so the azimuth angle ψ computed using Eqn. 4.3 suffers of a ±180° ambiguity: this issue can be easily resolved if two orthogonal gyroscopes are employed. Moreover, with this solution it is not more necessary to know the geodetic latitude value. Referring m_3 and m_4 as the orthogonal gyroscope output in its initial position and after the 180° turn, and S_y and b_y as the orthogonal gyroscope scale factor and bias errors (supposed constant during maytagging):

4.4. $S_y m_3 = -\Omega_e \sin\psi \cos\varphi + b_y$

4.5. $S_y m_4 = \Omega_e \sin\psi \cos\varphi + b_y$

Combining Eqns. 4.1, 4.2, 4.4 and 4.5 leads to:

4.6. $\psi = \tan^{-1} \frac{S_y(m_4 - m_3)}{S_x(m_1 - m_2)}$

The trade-off, however, is the increased sensitivity to bias drifts between the two orthogonal measurements. The platform rotation can be accurately obtained employing two mechanical stoppers, so the complexity of the overall mechanical system gets simplified since there is no need for an accurate control of the platform and a precise angular encoding system, as it happens for the carouseling method. This leads also to short alignment times. On the negative side, the gyroscope scale factor error and the thermal drift contribute to the azimuth measurement error.

Refer to [56] for an interesting comparison between carouseling and maytagging methods.

Redundant gyroscope configuration is an emerging method. It relies on the fact that more than two gyroscope are installed in the platform horizontal plane so that several biased samples of horizontal Earth rate component can be estimated at the same time. The overall effect of single gyroscope bias may be controlled by averaging multiple observations. This technique is simple, low-cost and light and there is no need for moving platform, but, on the other side, it is affected by thermal drift (so thermal compensation is necessary), it allows only a reduced gyroscope bias nulling and requires longer setup time.

The carouseling method was discarded due to the complex realization and qualification issues linked with the platform rotation, hence only maytagging and redundant gyroscope configuration have been investigated as possible methods to develop a 1 milliradian MEMS-based north-finding system.

The following step has been the research of a MEMS gyroscope with north-finding capabilities. For this purpose it is necessary to investigate in more details how the

gyroscope bias and scale factor errors contribute to the azimuth measurement error. Consider the case of a single-axis gyroscope perfectly aligned with the local vertical level described in Eqns. 4.1 and 4.2: in these equations it has been assumed that both bias b_x and scale factor S_x errors remain constant during the 180° turn. In reality, denoting the bias shift δb and the scale factor shift ε_s observed during the rotation as:

4.7.: $b_2 = b_1 + \delta b$

4.8. $S_2 = S_1(1 + \varepsilon_s)$

Eqns. 4.1 and 4.2 become:

4.9.: $S_1 m_1 = \Omega_e \cos\psi \cos\varphi + b_1$

4.10. $S_2 m_2 = -\Omega_e \cos\psi \cos\varphi + b_2$

Rearranging Eqns. 4.7, 4.8, 4.9 and 4.10 it possible to deduce [50] the following expression for the azimuth measurement error ε:

4.11. $\varepsilon = \frac{1}{2\Omega_e \sin\psi \cos\varphi}\left[\delta b - \frac{\varepsilon_s}{1+\varepsilon_s}(-\Omega_e \cos\psi \cos\varphi + b_2)\right]$

Hence, ε depends on the latitude, the actual azimuth angle ψ, the bias and bias variation values, the scale factor shift. Eqn. 4.11 shows that the maytagging method shall be carried out roughly orienting the gyroscope toward east or west in order to mitigate the effects of the gyroscope errors. With this assumption and considering $\varepsilon_s \ll 1$ Eqn. 4.11 can be easily simplified as:

4.12. $\varepsilon = \frac{1}{2\Omega_e \cos\varphi}[\delta b - \varepsilon_s b_2]$

Hence the azimuth measurement error depends on the gyro bias stability, the latitude of the measurement, the bias and the scale factor stability over the alignment time.

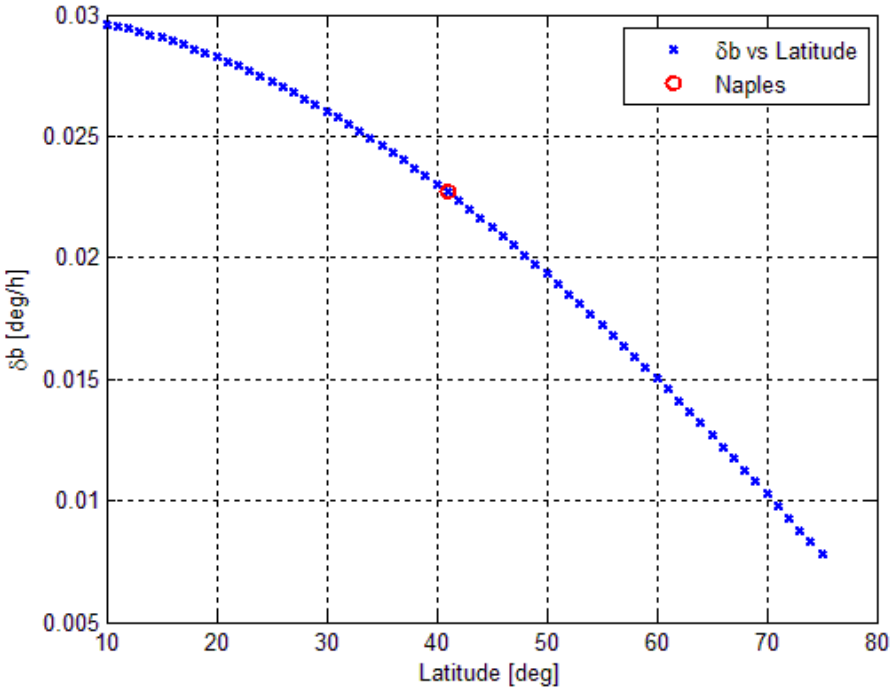

Figure 4.1 – Gyro δb requirement as a function of latitude for 1 mrad accuracy

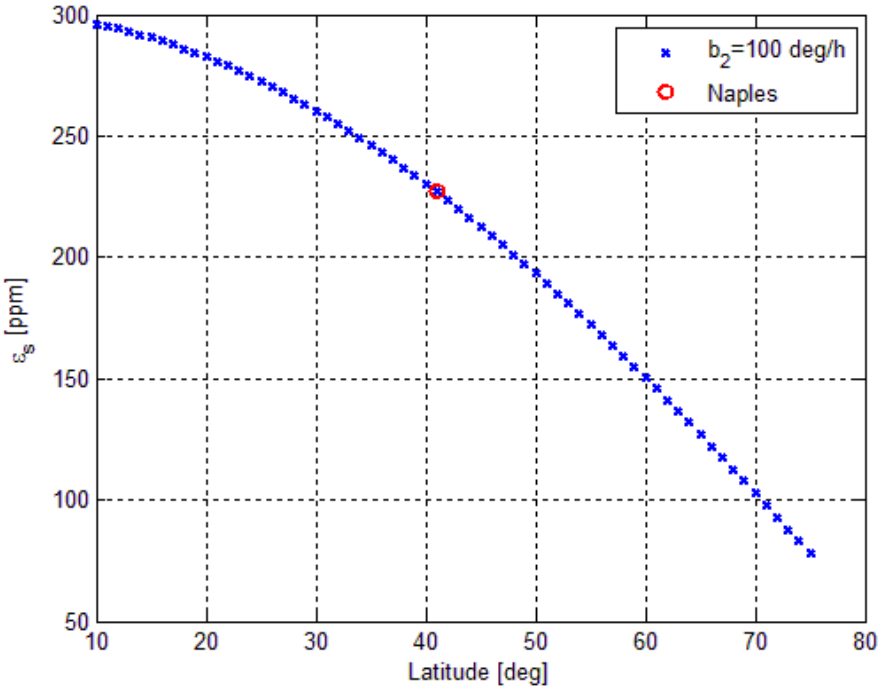

Figure 4.2 – Gyro ε_s requirement as a function of latitude for 1 mrad accuracy

As an illustration, Figures 4.1 and 4.2 above provide the gyro bias and scale factor requirements as a function of the angle latitude when the bias and the scale factor errors each contribute to a 1 mrad error.

At 40.8 degree latitude (Naples), for a 1 mrad accuracy, the bias stability over the alignment time period has to be 0.023 deg/hr and, assuming a bias offset of 100 deg/hr, the scale factor stability requirement becomes less than 230 ppm.

A two axis cylindrical Coriolis Vibrating Gyroscopes has been chosen as candidate sensor for north-finding applications. It declares bias offset small enough that the scale factor requirement less than 230 ppm is unlikely to be a problem. An Allan Variance analysis conducted on this cylindrical CVG is depicted in Figure 4.3 and Table 4.1 reports the Angular Random Walk and the Bias Instability values.

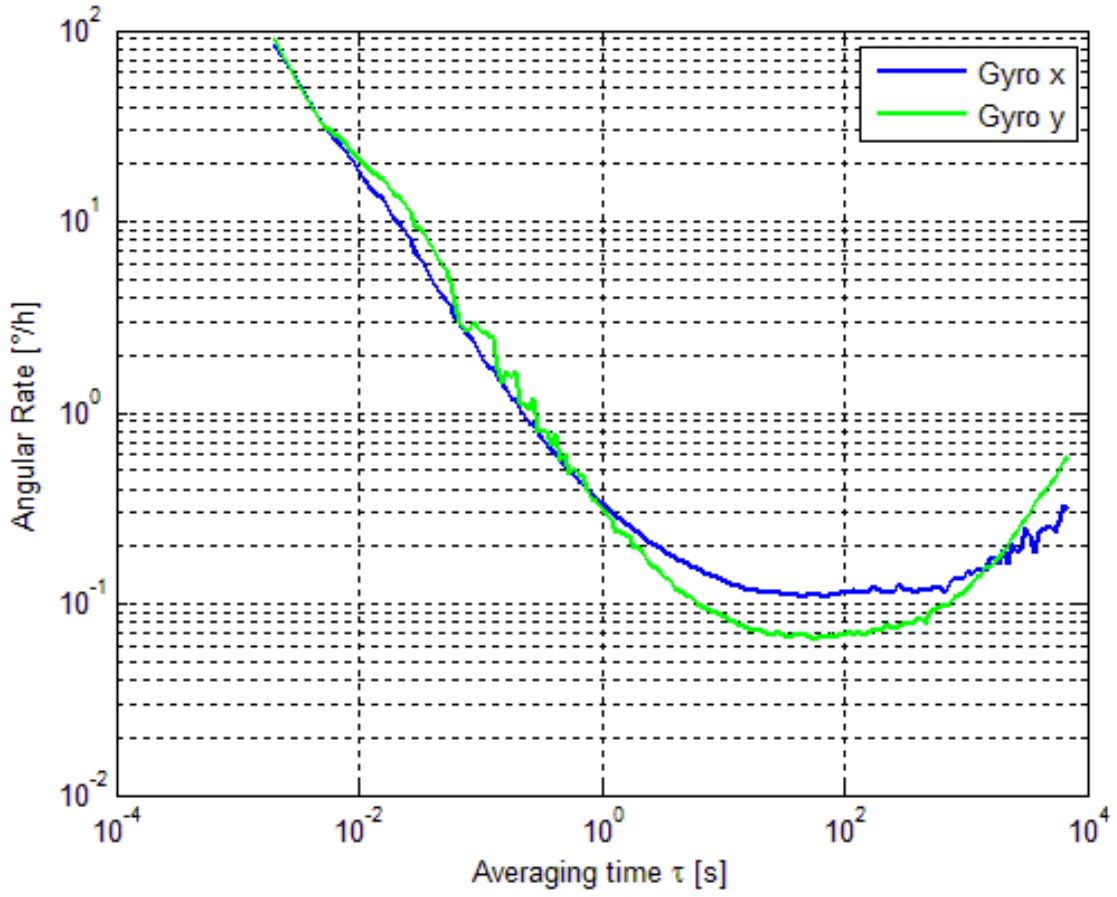

Figure 4.3 – Allan Variance of cylindrical CVG sensors

	ARW $(°/\sqrt{h})$	Bias Instability $(°/h)$
Gyro X	~ 0.0055 (99.7%)	~ 0.11 (97.7 %)
Gyro Y	~ 0.0043 (99.7%)	~ 0.066 (97.4 %)

Table 4.1 – Allan Variance main parameters of INL-CVG-U2200A

It is possible to note that these gyroscopes have an ARW two orders of magnitude less than the gyroscopes that have been chosen both for UAV and land navigation applications. The bias instability is two order of magnitude less than the sensors utilized in the AX1-GNS3 and one order of magnitude less than the gyroscopes employed in the AXD-LNS. However a ratio of about 4 is required in terms of bias instability coefficient improvement to theoretically reach 1 mrad north-finding accuracy at Naples latitude.

4.3 Lab Testing Activities

Waiting for a customized version of this cylindrical CVG with an improved bias instability, some lab testing activities have been carried out with the maytagging and redundant gyroscope configuration methods.

Figure 4.4 shows the functional block diagram of the equipment under test (EUT).

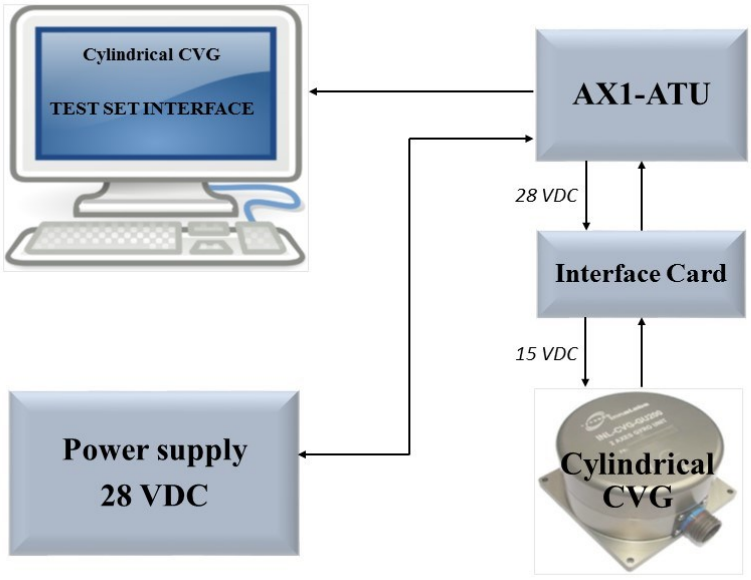

Figure 4.4 – Cylindrical CVG test configuration block diagram

The system under test, as shown in Figure 4.5, is composed by the following devices:

- Cylindrical CVG;
- Interface Card required to amplify the signal, to execute a filtering at a 50 Hz frequency and to provide the power supply to the CVG;
- AHRS made up of :
    1. 16 bit analog-to-digital-converter (*ADC*);
    2. *FPGA*: it is an hardware subsystem of the AHRS that performs the reading of the data, the conversion at 16 kHz from the sensors' analog output in digital representation, a data filtering in 32-bit floating-point representation and a decimation of the filtered samples at the frequency of 512 Hz; it also execute a compensation through a set of calibration coefficients that best fit the sensors' error model;
    3. *Microprocessor*.

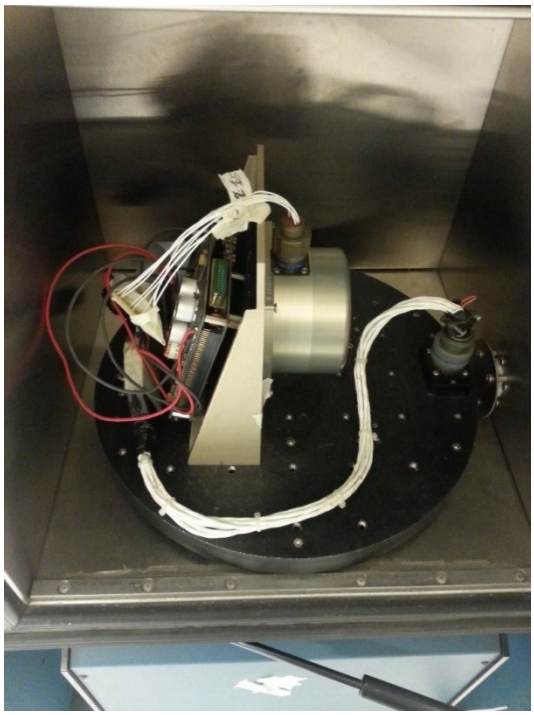

Figure 4.5 – Equipment under test (EUT)

Table 4.2 reports a summary and a brief description of the tests that have been carried out.

Sequence	Description
0	The EUT performs four full turns with a 10° step angle. Each position is held for 60 seconds. The unit is turned on at room temperature and turned off for one hour before the following test.
1	The EUT is initially set to the home position (see Figure 4.5) and then rotated to 180° in clockwise direction. Each position is held for 60 seconds and carried out 40 times, so that the test duration is of about 90 minutes. The unit is turned on at room temperature and turned off for one hour before the following test.
2	Repetition of sequence 1
3	Repetition of sequence 2
4	Repetition of sequence 3
5	The EUT is set to a position rotated with respect to the home position of 90° and then rotated to 180° in clockwise direction. Each position is held for 60 seconds and carried out 40 times, so that the test duration is 90 minutes. The unit is turned on at room temperature and turned off for one hour before the following test.
6	Repetition of sequence 5
7	Repetition of sequence 6
8	The EUT is initially set to the home position (see Figure 4.5) and then rotated to 360° in clockwise direction by steps of 45°. Each position (0°-45°-90°-135°-180°-225°-315°) is held for 60 seconds and carried out 10 times, so that the test duration is 80 minutes. The unit is turned on at room temperature and the measurements are extracted after one hour after the starting.
9	The EUT is initially set to the home position (see Figure 4.5) and then rotated to 360° in clockwise direction with a step of 45°. Each position (0°-45°-90°-

	135°-180°-225°-315°) is held for 60 seconds and carried out 10 times, so that the test duration is 80 minutes. The unit is turned on at room temperature and turned off for one hour before the following test. The measurements are extracted one hour after the starting.
10	Repetition of sequence 10
11	Repetition of sequence 11
12	The EUT is initially set to the home position (see Figure 4.5) and then rotated to 360° in clockwise direction with a step of 45°. Each position (0°-45°-90°-135°-180°-225°-315°) is held for 60 seconds and carried out 10 times, so that the test duration is 80 minutes. The unit is turned on at room temperature and the measurements are extracted immediately.

Table 4.2 – Test sequences description

The sequence zero has been carried out to demonstrate the cylindrical CVG capability to measure the Earth's rate horizontal component. Maytagging method has been tested during sequences from 1 to 7 and sequences from 8 to 12 have been used to simulate a redundant gyroscope configuration.

4.4 Results and Conclusions

4.4.1 Earth Rate Measurement

Figure 4.6 shows the Earth's rate horizontal component as measured from the cylindrical CVG after executing four full turn with a 10 degrees step angle and holding each position for one minute (sequence zero in Table 4.2).

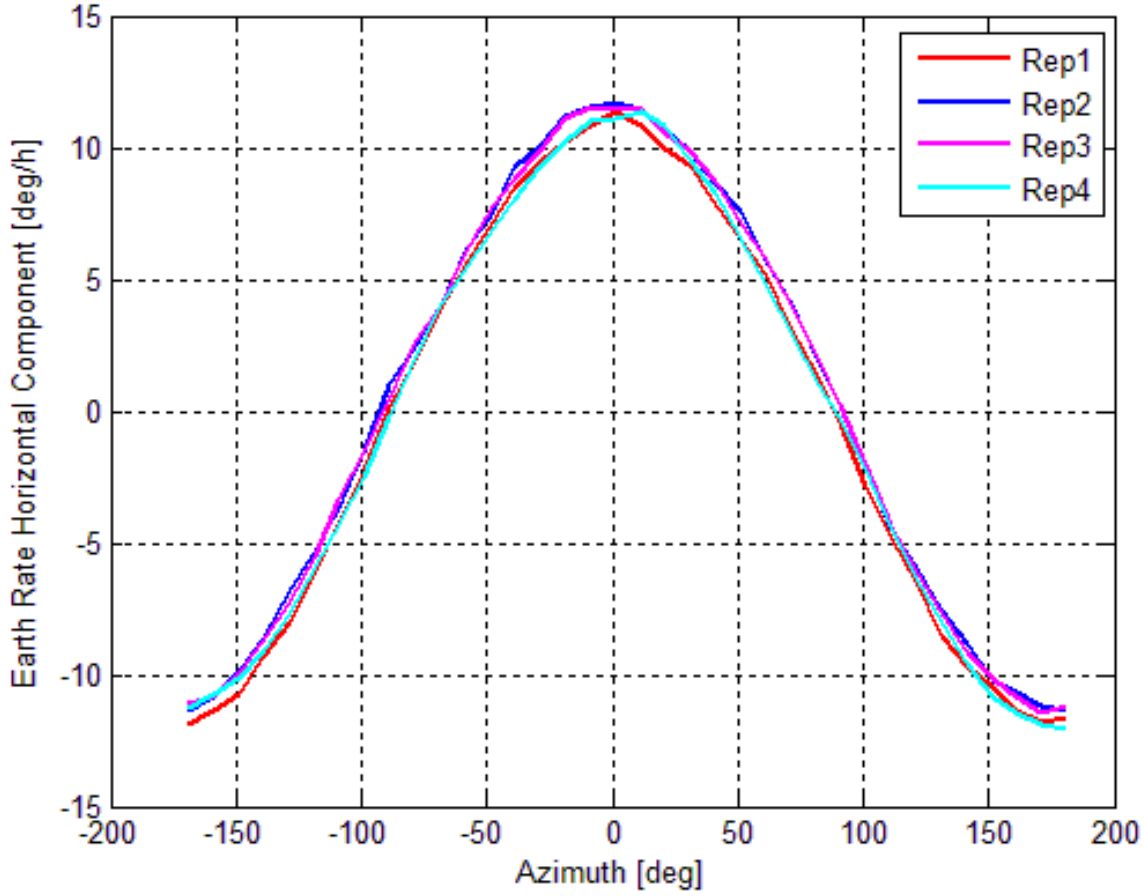

Figure 4.6 – Earth's rate horizontal component measurement

In this figure four sinusoids are depicted, with maximum and minimum values of about 11 degrees per hour, that is the Earth's rate horizontal component value at Naples latitude. This is a first demonstration of the north-finding capabilities of the cylindrical CVG sensors.

4.4.2 Maytagging Method

The angular rates sampled in the sequences from 1 to 7, after the power on, are averaged over 60 seconds in order to calculate an azimuth angle every 60 seconds using Eqn. 4.6 and to have at the end 80 different values. The values are represented in Figures 4.7 - 4.13, where it is also possible to note the distances of each sample from the mean value over the whole test.

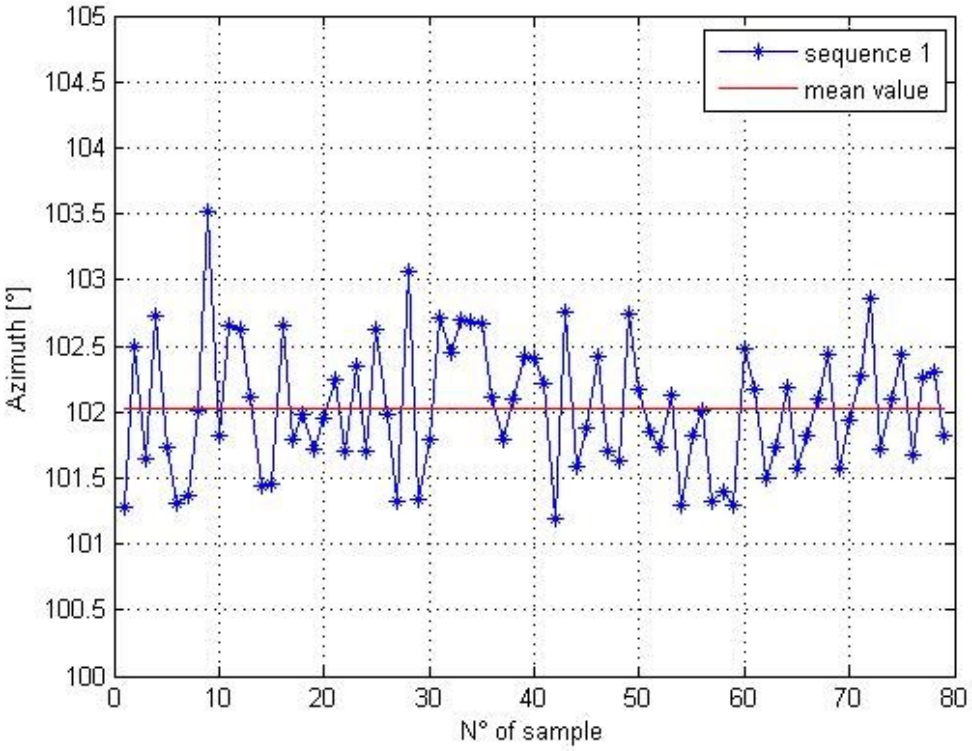

Figure 4.7 – Azimuth over sequence 1

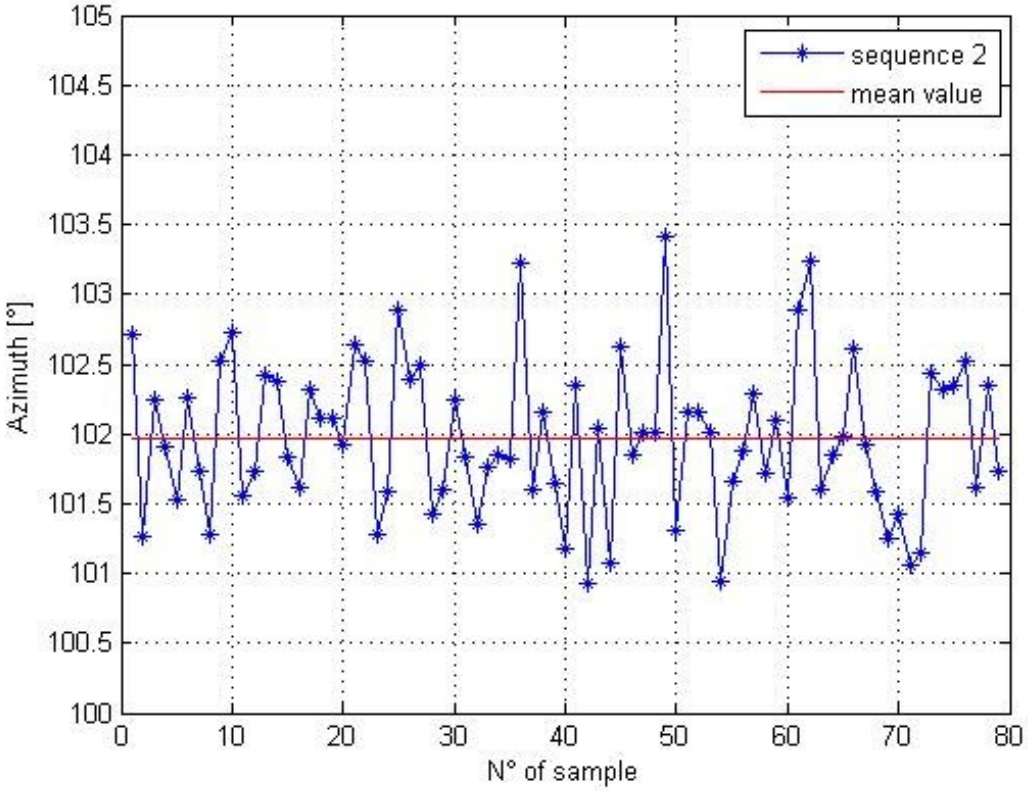

Figure 4.8 – Azimuth over sequence 2

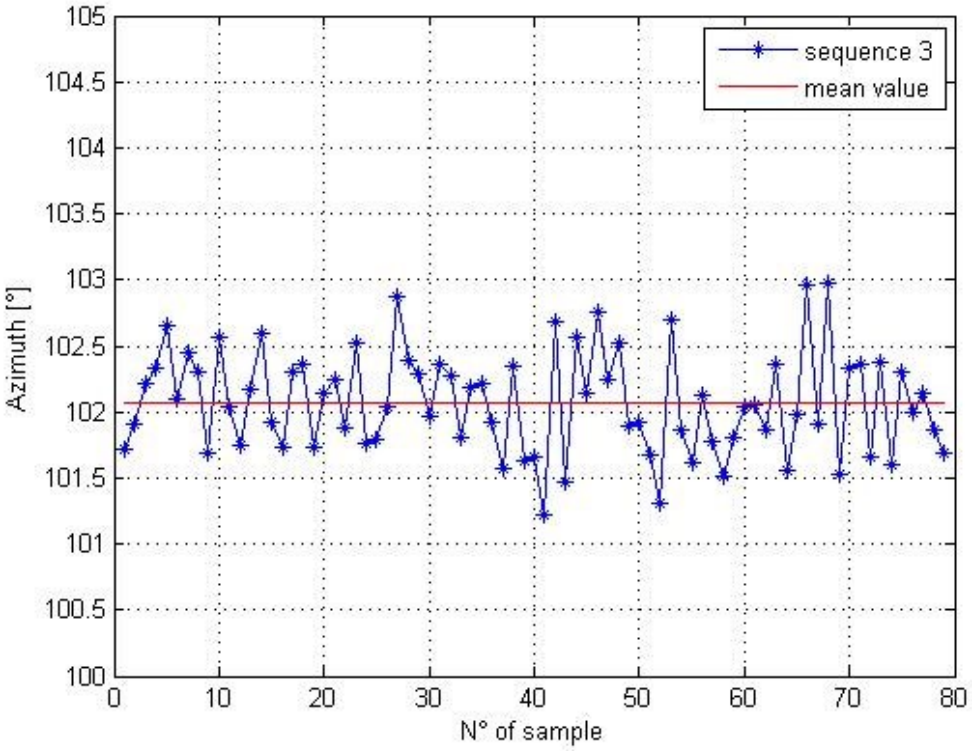

Figure 4.9 – Azimuth over sequence 3

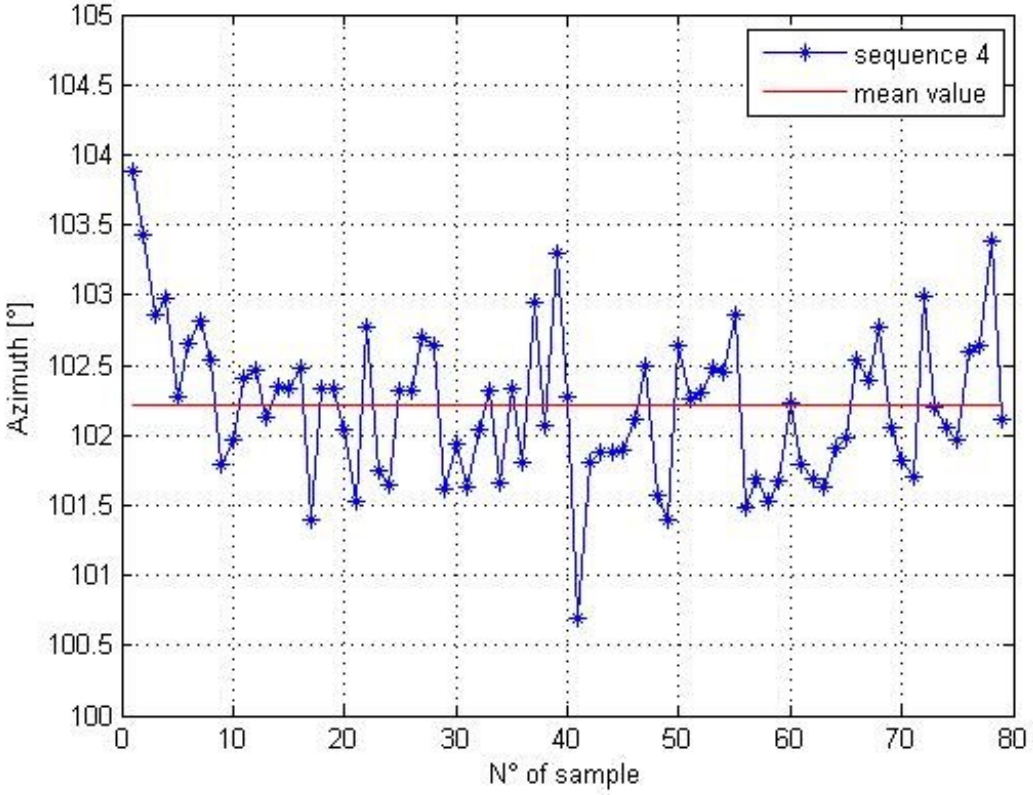

Figure 4.10 – Azimuth over sequence 4

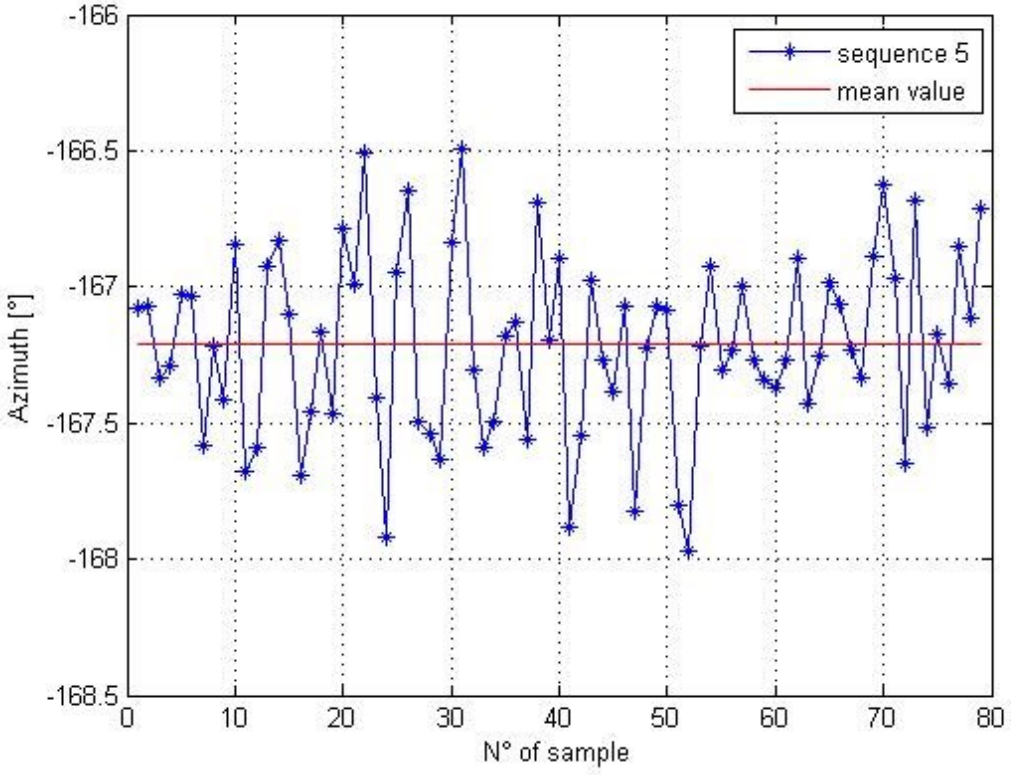

Figure 4.11 – Azimuth over sequence 5

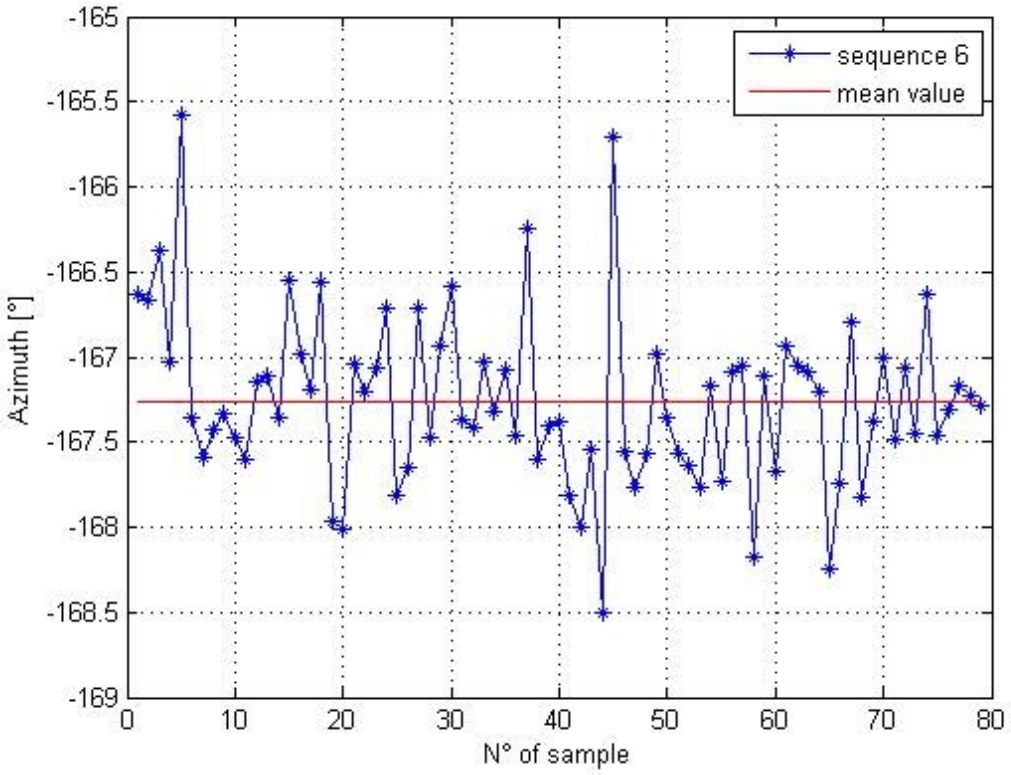

Figure 4.12 – Azimuth over sequence 6

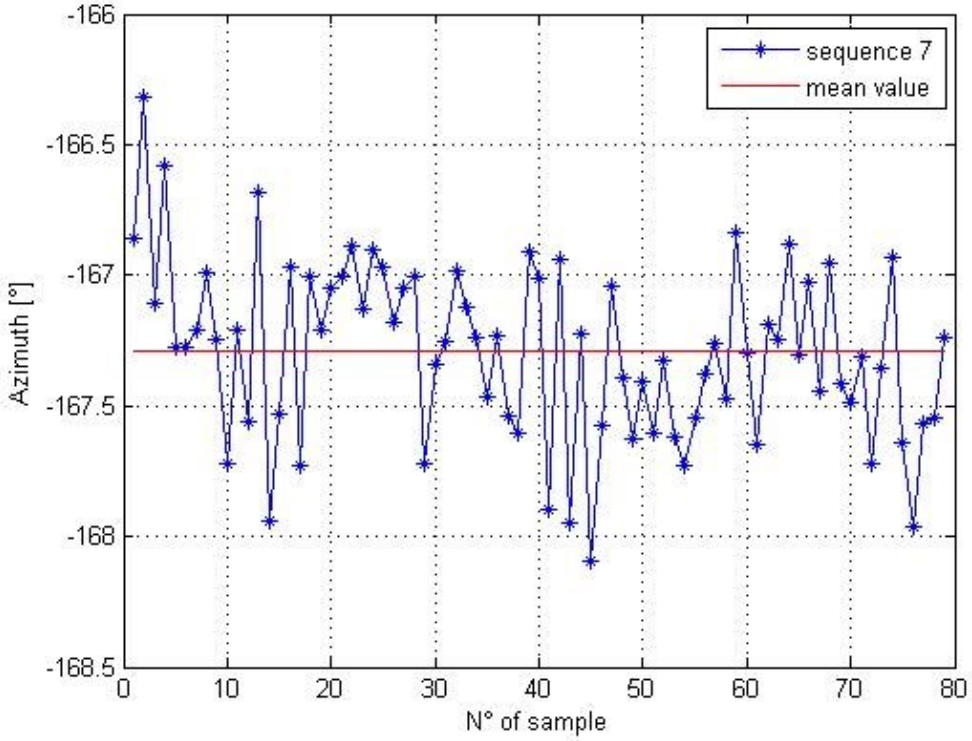

Figure 4.13 – Azimuth over sequence 7

The mean values for each sequence and the corresponding standard deviations are the following:

Sequence	Mean Value [°]	Standard Deviation [mrad]
1	102.03	8.60
2	101.96	9.47
3	102.07	6.75
4	102.21	9.33
5	-167.21	5.83
6	-167.26	8.80
7	-167.29	5.90

Table 4.3 – Maytagging statistics

The repeatability of the measurement was evaluated considering the distance of the mean value of each sequence (from 1 to 4 and from 5 to 7) with respect to the mean value over all the sequences, Figures 4.14 and 4.15. The maximum value of these distances are equal to 2.4 mrad and 0.75 mrad.

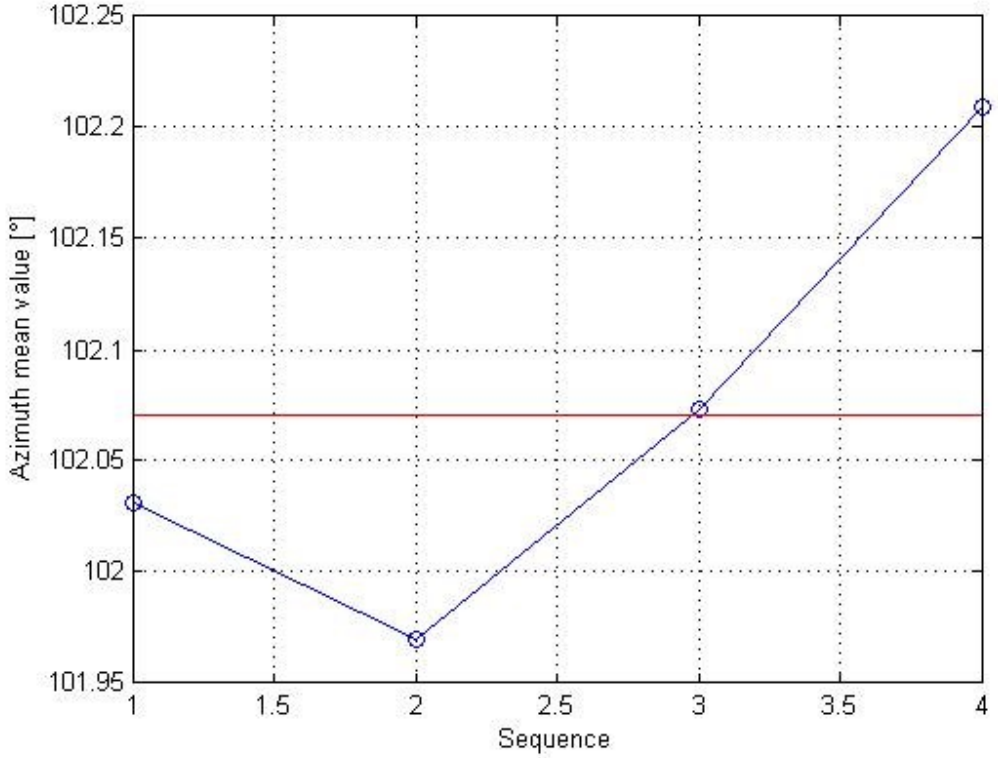

Figure 4.14 – Azimuth repeatability over sequences from 1 to 4

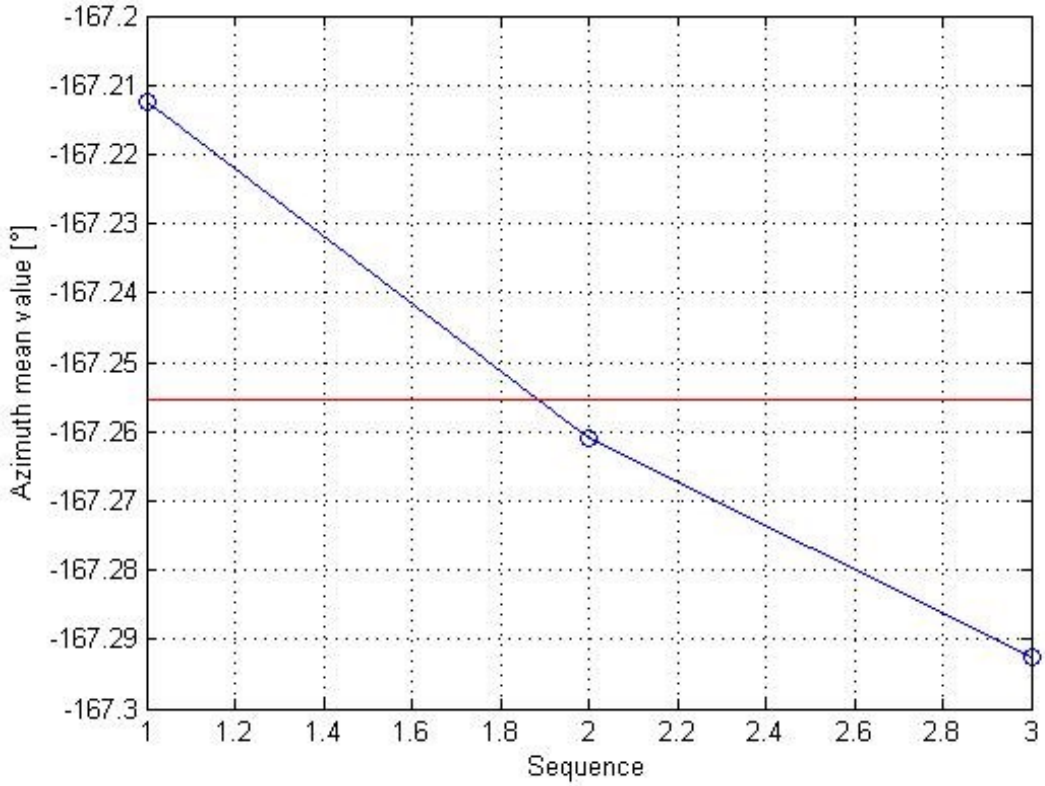

Figure 4.15 – Azimuth repeatability over sequences from 5 to 7

4.4.3 Redundant Gyroscope Configuration Simulations

Sequences from 8 to 12 have been used to simulate a redundant gyroscopes configuration in order to evaluate its north-finding performances. Since only a two-axis gyroscope configuration is available, a four-axis configuration is simulated coupling the gyro's measurements along x-axis and y-axis every two consecutive positions, in order that a skewed configuration with a first axis direct along ψ, the second along $\psi + 45°$, the third along $\psi + 90°$ and the last along $\psi + 135°$ may be obtained. According to this process there are 8 different possible couples (0°-45°; 45°-90°; 90°-135°; 135°-180°; 180°-225°; 225°-270°; 270°-315°; 315°-0°) and so 8 different azimuth estimations 10 times for each of the five tests (10 full turns have been carried out for each of the five sequences, as reported in Table 4.2).

Using these data sets, it is possible to define the repeatability of the measurement, evaluated considering the distance of the mean value of each configuration repeated five times with respect to the mean value over all the tests performed, Figures 4.16 - 4.23.

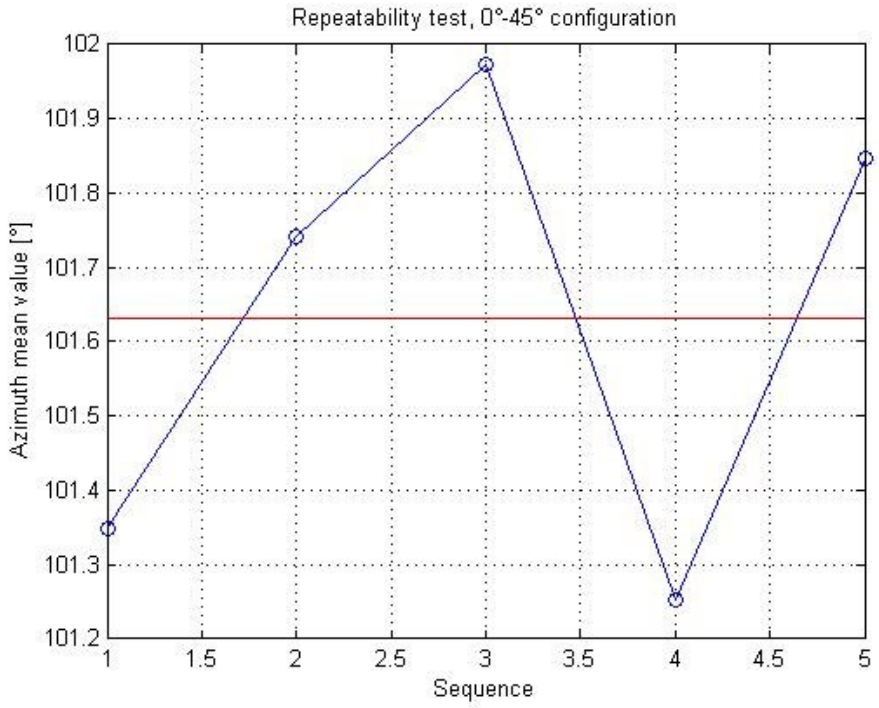

Figure 4.16 – Azimuth repeatability for 0°- 45° configuration

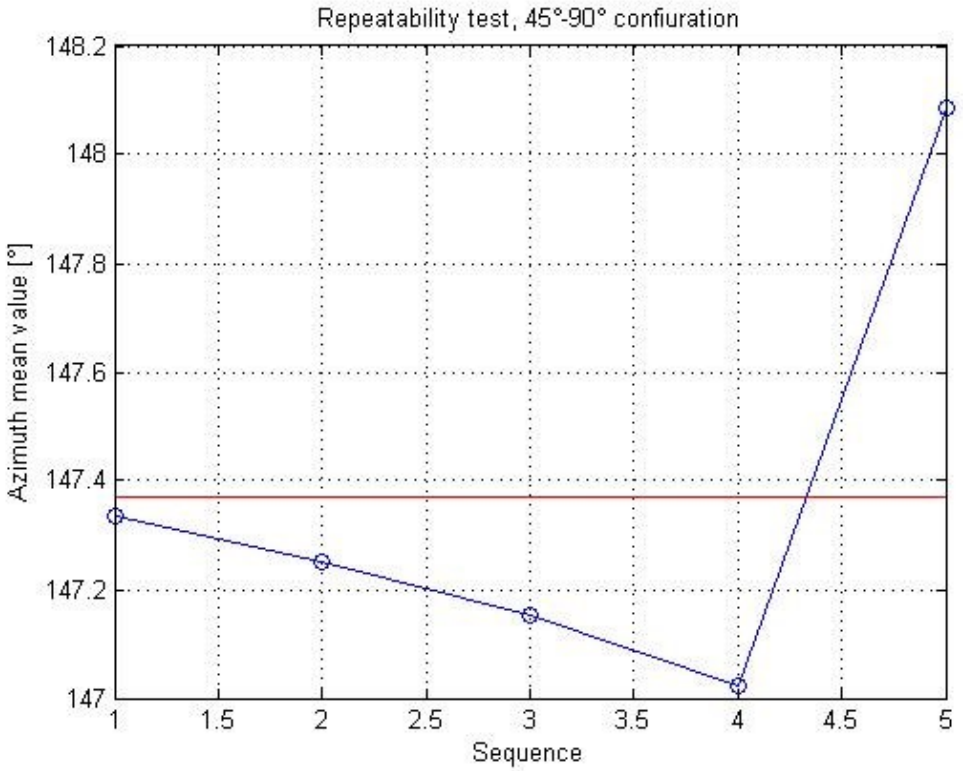

Figure 4.17 – Azimuth repeatability for 45°- 90° configuration

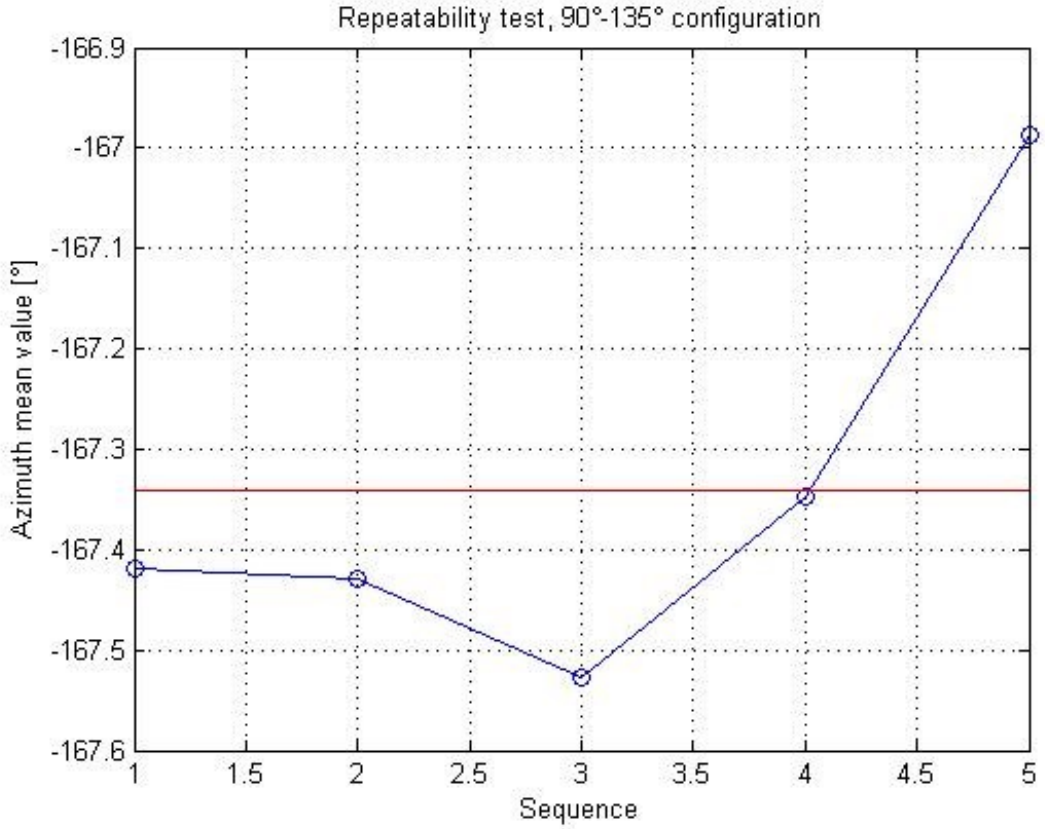

Figure 4.18 – Azimuth repeatability for 90°- 135° configuration

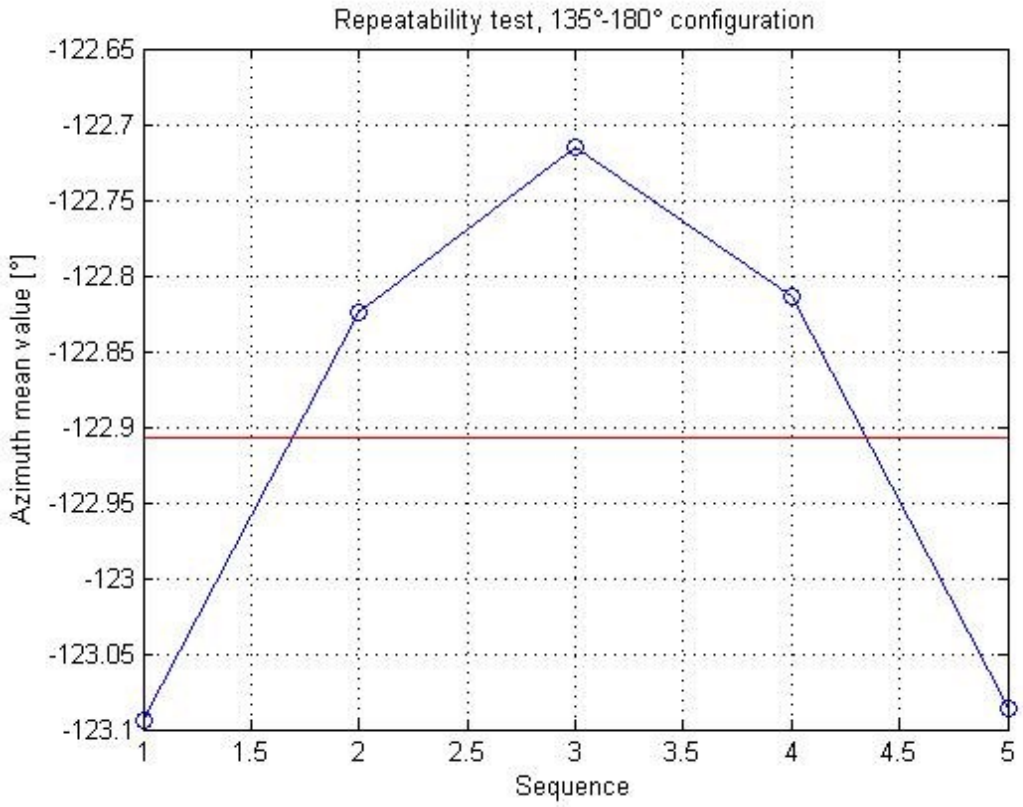

Figure 4.19 – Azimuth repeatability for 135°- 180° configuration

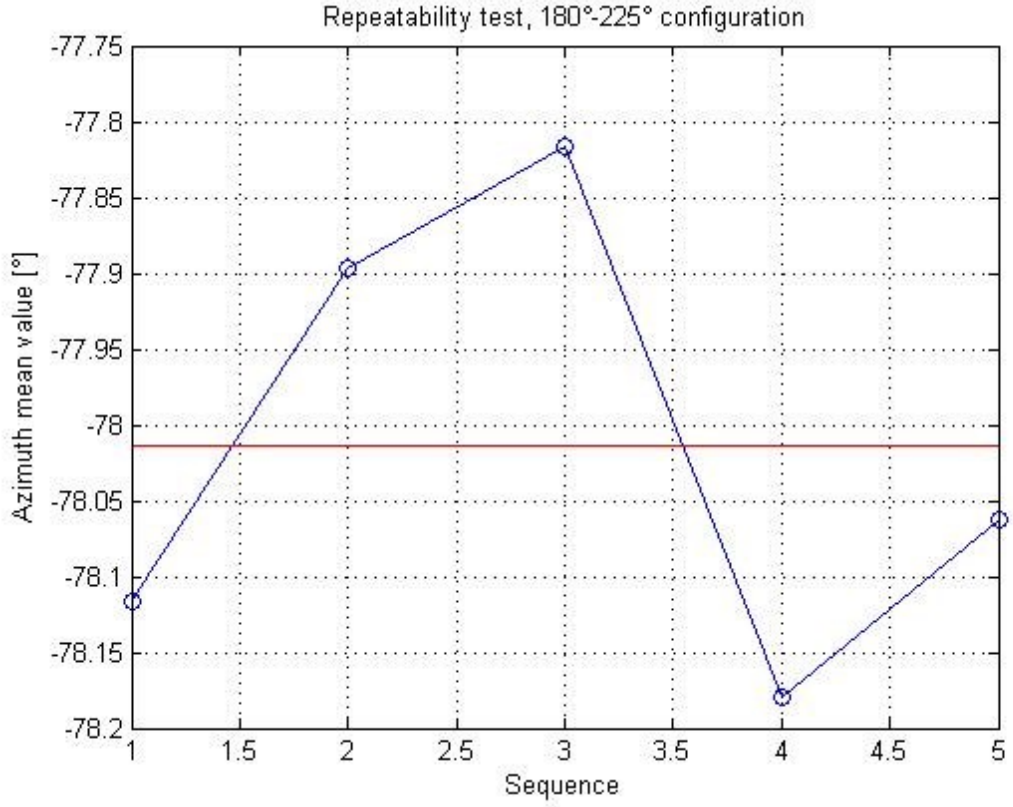

Figure 4.20 – Azimuth repeatability for 180°- 225° configuration

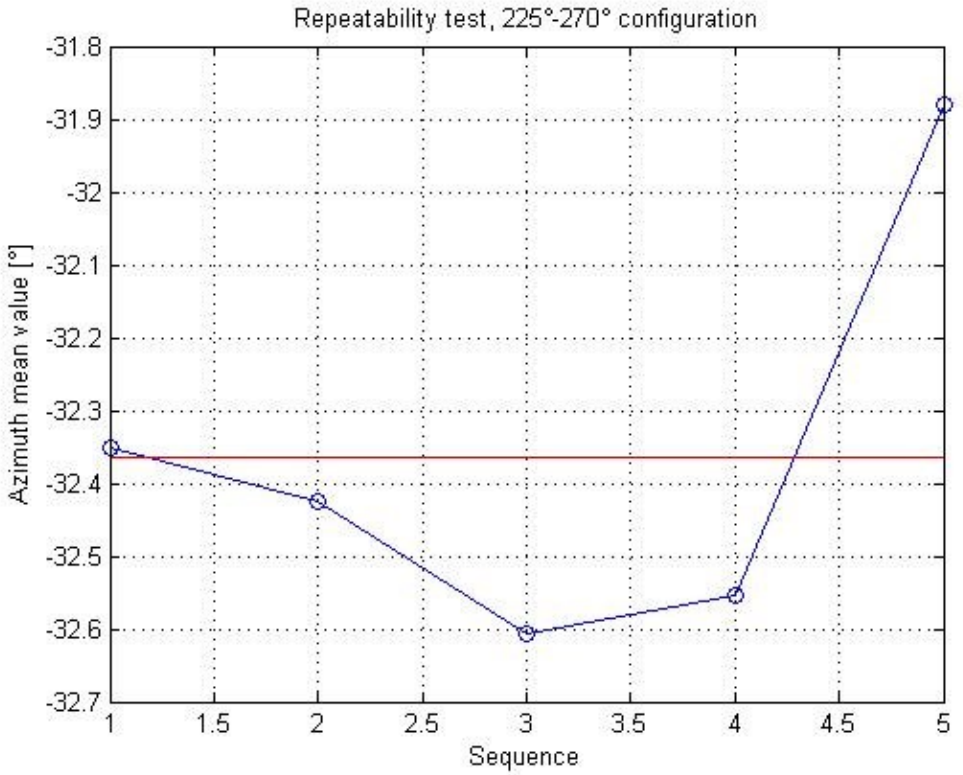

Figure 4.21 – Azimuth repeatability for 225°- 270° configuration

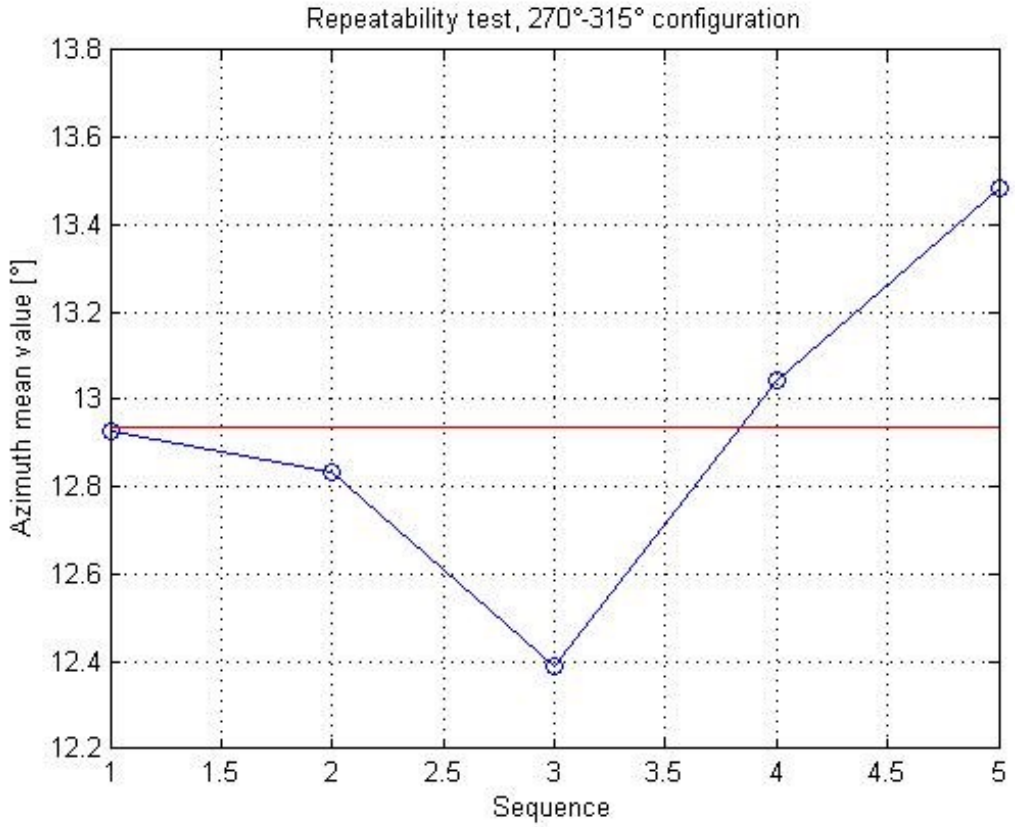

Figure 4.22 – Azimuth repeatability for 270°- 315° configuration

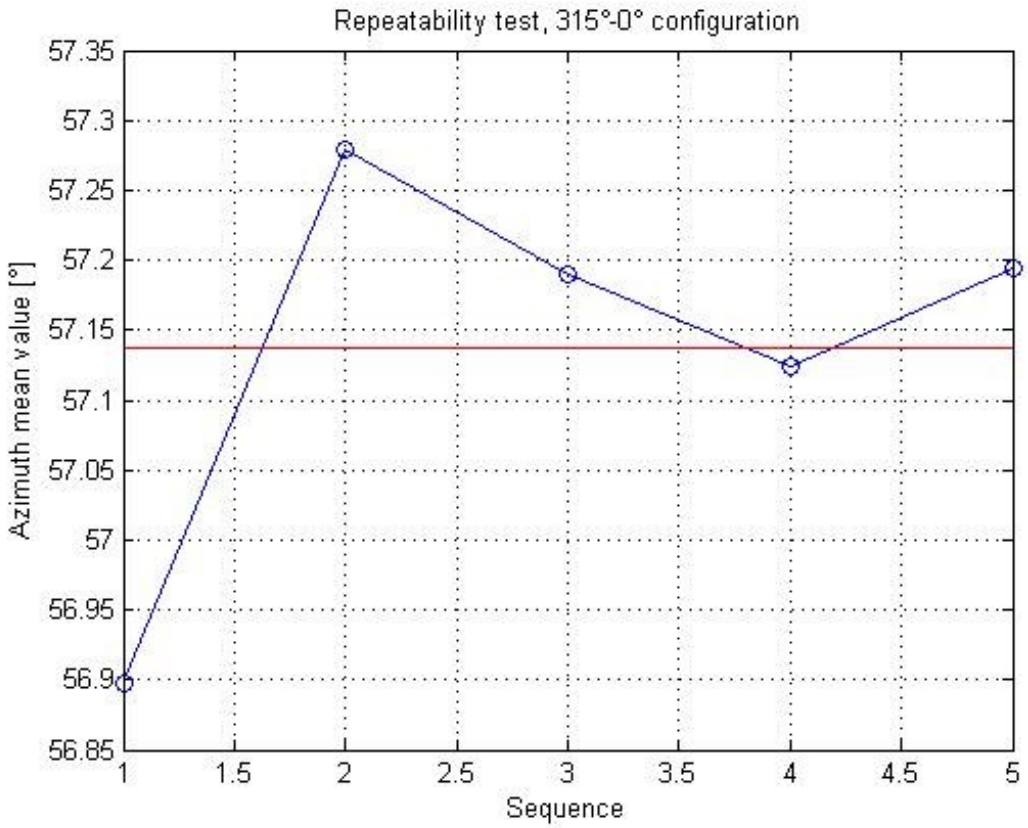

Figure 4.23 – Azimuth repeatability for 315°- 0° configuration

The maximum value of these distance are listed in the following table:

Configuration	Repeatability [mrad]	Repeatability [°]
0°-45°	6.63	0.38
45°-90°	12.49	0.71
90°-135°	6.18	0.35
135°-180°	3.34	0.19
180°-225°	3.46	0.20
225°-270°	8.46	0.49
270°-315°	9.56	0.55
315°-0°	4.17	0.23

Table 4.4 – Simulated Redundant Configuration statistics

In conclusion, this cylindrical CVG device has demonstrated a sub-degree repeatability for north-finding applications, both using the standard maytagging method and the promising redundant gyroscope configuration.

Conclusions and further recommendations

The main scope of this research activity has been to explore and develop low-cost innovative Hardware and Software architectures for MEMS-based inertial systems combining new generation MEMS sensors and innovative data fusion algorithms in order to replace Fiber Optic technology in several applications.

First of all, the research focused on the realization of a MEMS-based INS able to provide an attitude solution suitable for UAS applications. Indeed, the standard attitude measurement accuracy FAA requirements, i.e. 1° rms for pitch and roll and 3° rms for heading, are intended for typical mission profiles that where adopted in the past. After a careful design phase, involving the inertial sensors' choice and the HW and SW architectures' definition, the AX1-GNS3 system has been manufactured. It is a GPS Navigation and GPS-aided Attitude and Heading reference system, built around three separate devices: an IMU employing industrial-grade inertial sensors, a magnetometer and GPS receiver/antenna equipment. An EKF is utilized to fuse data coming from these different devices. Lab testing activities have been conducted on the AX1-GNS3 system in order to adequately compensate the inertial sensors' deterministic errors and to stochastically characterize the sensors' random noise. Subsequently, van testing activities have been carried out to allow an EKF tuning and to validate the embedded SW. Experimental results demonstrated the AX1-GNS3 system capabilities to provide an attitude measurement accuracy much higher than FAA requirements, a level of accuracy suitable for UAV applications. Indeed, currently the AX1-GNS3 system has been installed on the Alenia SKY-Y UAS and onboard the Italian largest UAV ever produced, the Piaggio Hammer Head MALE.

Further studies may involve the development of a device employing higher grade gyroscopes in a magnetometer-less configuration, with the aim to eliminate the magnetometer drawbacks and, at the same time, maintain an high level of accuracy in the attitude determination.

A second research theme regarded the realization of a MEMS-based LNS suitable to satisfy the growing demand from both civil and military markets of a self-contained, dead-reckoning device able to provide a continuous and affordable PVT solution even in GNSS denied or degraded environments. A target performance of a geodetic position solution error less than the 3% of the travelled distance without receiving a GPS signal was established. At the end of the design phase, involving the inertial sensors' choice and the HW and SW architectures' definition, the AXD-LNS system has been manufactured. It is a MEMS-based IMU employing industrial-grade accelerometers and quasi-tactical grade gyroscopes, linked to a GPS receiver and, via CAN bus, to the host vehicle odometer. The EKF implemented in this device has been described and some PC simulations have been conducted in order to demonstrate some EKF capabilities, such as fast recovery of a large initial heading error and the need for adequately estimate the odometer scale factor error in order to achieve the target performance. Results from a van testing campaign demonstrated the AXD-LNS system capabilities to successfully meet the target performance. Currently, due to its level of performances, the AXD-LNS system is being tested onboard Italian Army land vehicles.

Further activities may involve the implementation of a more complicated EKF able to accurately estimate the accelerometers bias relying on GPS measurements, if available, or on odometer measurements when GPS signal is lost. These activities shall improve the system capability to evaluate the pitch angle and, as a consequence, the altitude estimation. Moreover, it would be possible to provide a PVT solution through an integration process of the accelerometers output in case of a contemporary odometer fault and GPS signal loss.

A third research activity covered the implementation of an advanced data fusion algorithm to accurate initialize a MEMS-based INS navigation state within a short alignment time. Especially for low-cost INS, the initial alignment is a challenging issue because of the high noises from the low-cost inertial sensors. Relying on the fact that the host vehicle is at rest and non-rotating during the initialization phase, it

has been established to implement a ZUPT algorithm to accomplish the fine alignment task. A model block diagram and an analytical ZUPT algorithm description have been illustrated, together with a discussion on the ZUPT pros/cons when compared with the AX1-GNS3 fine alignment algorithm. ZUPT algorithm has been successfully tested, demonstrating to be able to provide an accurate initial navigation solution in a very short alignment time. Currently, the ZUPT algorithm is implemented in the AX1-GNS5 system, the Axitude MEMS-based INS designed for high-g dynamics environments that employs industrial-grade inertial sensors and that is equipped with an integrated GPS receiver. Due to its navigation performances, the AX1-GNS5 product is currently being tested onboard the Mirach-100, the integrated aerial target system designed and manufactured by Selex ES company to train and qualify worldwide Armed Forces major weapon systems.

An interesting activity may be to implement a ZUPT algorithm in a PF version instead of the actual EKF version, in order to compare the two solutions in terms of accuracy and alignment time.

A fourth research activity concerned with the development of a MEMS-based device able to self-initialize azimuth angle with 1 mrad accuracy. Low-cost INS usually relies on Earth's magnetic field measurements to initialize heading angle, but the accuracy of this solution is limited by local Earth's magnetic field distortions and by host vehicle internal and external magnetic interferences. An alternative approach is the gyrocompassing, that provides an azimuth angle through an observation of Earth's rate horizontal component, but this procedure requires accurate and stable measurements capabilities. Hence, gyrocompassing by MEMS has not been retained possible for many years, but due to recent performance improvements it has been established to explore again this solution, very interesting from both academic and industrial viewpoints. In order to perform a gyrocompassing by MEMS, it has been chosen to apply the well-established maytagging technique and to explore the capabilities of the promising redundant gyroscope configuration method. A two-axis tactical-grade CVG gyroscope has been utilized to compare these two solutions.

Experimental tests applying the maytagging method and numerical simulations with redundant gyroscope configuration demonstrated the CVG capability to reach a sub-degree repeatability for north-finding applications, even if the target performance of 1 mrad accuracy is very close but not completely fulfilled, especially with the second technique.

Further activities may regard the repetition of the experimental tests using a customized version of the CVG device with improved performances and a demonstration of the redundant gyroscope configuration technique real capabilities employing a four-axis CVG configuration.

References

[1] Renga, A., Graziano, M.D., D'Errico, M., Moccia, A., Menichino, F., Vetrella, S., Accardo, D., Corraro, F., Cuciniello, G., Nebula, F., and Del Monte, L. "*Galileo-based space-airborne bistatic SAR for UAS navigation*", Aerospace Science and Technology, 27 (1), pp. 193-200, 2013.

[2] S. Verhagen, "*The GNSS integer ambiguities: estimation and validation*", Ph.D. Thesis, Delft TU, 2005.

[3] P. J. G. Teunissen, S. Verhagen , "*Integer Aperture Estimation A framework for GNSS Ambiguity Acceptance Testing*", Inside GNSS, March/April 2011, pp. 66-73.

[4] R. Hulsing, "*MEMS Inertial Rate and Acceleration Sensor*", IEEE Position Location and Navigation Symposium, 1998.

[5] D. W. Allan, "*Statistics of Atomic Frequency Standards*", Proceedings of IEEE, Vol. 54, No. 2, 1966.

[6] D. W. Allan, "*Time and Frequency (Time-Domain) Characterization, Estimation and Prediction of Precision Clocks and Oscillators*", IEEE Transportation on Ultrasonics, Ferroelectrics and Frequency Control, Vol. UFFC-34, No. 6, 1987.

[7] R. E. Kalman, "*A New Approach to Linear Filtering and Prediction Problems*", ASME Transactions, Vol. 182D, 1960.

[8] A. Renga, G. Fasano, A. Simonetti, D. Accardo, and M. Grassi, "*Fusion of multi-antenna carrier phase differential GPS and inertial measurements for performance evaluation of high accuracy integrated aircraft navigation systems*", in Proceedings of the American Institute of Aeronautics and Astronautics (AIAA'12), p. 21, Garden Grove, California, USA, September 2012.

[9] G. Fasano, A. Renga, D. Accardo, M. Grassi, and R. Senatore, "*An advanced system for performance evaluation of integrated navigation systems*", in Proceedings of the 30th Digital Avionics Systems Conference (DASC '11), pp. 1–13, Seattle, Wash, USA, October 2011.

[10] iNAV-FMS: "*NAV_Command: Operation and User Instructions*", iMAR GmbH.

[11] Trimble BD960: "*Trimble BD960 GNSS Receiver Module User Guide*", Trimble Company.

[12] B. Hoffmann-Wellenhof, H. Lichtenegger, and J. Collins, "*Global Positioning System: Theory and Practice*", Springer, New York, NY, USA, 1992.

[13] E.D. Kaplan and J. Hegarty, "*Fundamentals of satellite navigation*", in Understanding GPS: Principles and Applications, E. D. Kaplan, Ed., ArtechHouseMobile Communications Series, 2nd edition, 2006.

[14] Lachapelle, G., "*High Sensitivity GNSS Limitations in RF Perturbed Environments",* NATO STO Lecture Series SET-197, Navigation Sensors and Systems in GNSS Degraded and Denied Environments, Oct. 2013.

[15] S. Sukkarieh, E.M. Nebot and H.F. Durrant-Whyte, "*A High Integrity IMU/GPS Navigation Loop for Autonomous Land Vehicle Applications*", IEEE Transactions on Robotics and Automation, Vol. 15, NO. 3, June 1999.

[16] Zhao, Y., "*GPS/IMU Integrated System for Land Vehicle Navigation based on MEMS*", Licentiate Thesis in Geodesy, Royal Institute of Technology, Stockholm (Sweden), September 2011.

[17] Titterton D.H. and Weston, J.L. (1997): "*Strapdown inertial navigation technology*", Peter Peregrinus Ltd., London, UK, 1997.

[18] J. Houghton and S. Kennedy, "*Analysis of a Tightly-Coupled MEMS IMU based GNSS/INS with an External Odometer*", NovAtel Inc., Calgary, AB, Canada.

[19] E.M. Hemerly and V.R. Schad, "*Implementation of a GPS/INS/Odometer Navigation System*", ABCM Symposium Series in Mechatronics, Vol. 3, pp. 519-524, 2008.

[20] Y-W. Huang and K-W. Chiang, "*Improving the Performance of MEMS IMU/GPS Pos Systems for Land based MMS utilizing Tightly Coupled Integration and Odometer*", ISPRS Proceedings, 2010.

[21] M. Ilyas, Y. Yang, Q. Shi Qian, R. Zhang, "*Low-Cost IMU/Odometer/GPS Integrated Navigation Aided with Two Antennae Heading Measurements for Land Vehicle Applications*", IEEE Control and Decision Conference, Guiyang, China, 25-27 May 2013.

[22] J. Georgy, A. Noureldin and M. Bayoumi, "*Mixture Particle Filter for Low Cost INS/Odometer/GPS Integration in Land Vehicles*", IEEE Vehicular Technology Conference, Barcelona, Spain, 26-29 April 2009.

[23] M. Cossaboom, J. Georgy, T. Karamat and A. Noureldin, "*Augmented Kalman Filter and Map Matching for 3D RISS/GPS Integration for Land Vehicles*", International Journal of Navigation and Observation, Hindawi Publishing Corporation, Volume 2012, 16 pages.

[24] U. Iqbal, T.B. Karamat, A.F. Okou and A. Noureldin, "*Experimental Results on an Integrated GPS and Multisensor System for Land Vehicle Positioning*", International Journal of Navigation and Observation, Hindawi Publishing Corporation, Volume 2009, 18 pages.

[25] D. Sun, M.G. Petovello and M.E. Cannon, "*GPS/Reduced IMU with a Local Terrain Predictor in Land Vehicle Navigation*", International Journal of Navigation and Observation, Hindawi Publishing Corporation, Volume 2008, 15 pages.

[26] D. Sun, M.G. Petovello and M.E. Cannon, "*Ultratight GPS/Reduced-IMU Integration for Land Vehicle Navigation*", IEEE Transactions on Aerospace and Electronic Systems, Vol. 49, NO. 3, July 2013.

[27] Rogers, R.M., "*Applied Mathematics in Integrated Navigation Systems*", AIAA Education Series, 2nd edition, 2003.

[28] Farrell J.A. and Barth M. (1999). "*The Global Positioning System & Inertial Navigation*", McGraw-Hill, New York.

[29] Savage P. G., "*Strapdown Analytics*", 2nd edition, Strapdown Associates, Inc. 2007.

[30] Groves P., "*Principles of GNSS, Inertial, and Multisensor Integrated Navigation Systems*", Artech House, © 2008.

[31] Bistrov V., "*Performance Analysis of Alignment Process of MEMS IMU*", International Journal of Navigation and Observation, Hindawi Publishing Corporation, Volume 2012, 11 pages.

[32] C. Cristina, B. Ludovico, and C. Alessandro, "*Design of a low-cost GPS/magnetometer system for land-based navigation: integration and autocalibration algorithms*," in TS07F - Mobile and Asset Mapping Systems, Marrakech, Morocco, 2011.

[33] Jew M., El-Osery A. and Bruder S., "*Implementation of an FPGA-based Aided IMU on a Low-Cost Autonomous Outdoor Robot*", IEEE/ION Position Location and Navigation Symposium (PLANS), Indian Wells, CA, USA, 4-6 May 2010.

[34] Elkaim G.H., Lizarraga M., Pedersen L., "*Comparison of low-cost GPS/INS sensors for Autonomous Vehicle applications*", IEEE/ION Position Location and Navigation Symposium (PLANS), Monterey, CA, USA, 5-8 May 2008.

[35] H. Chao, C. Coopmans, L. Di, and Y. Q. Chen, "*A comparative evaluation of low-cost IMUs for unmanned autonomous systems*", in Proceedings of the IEEE Conference on Multisensor Fusion and Integration for Intelligent Systems (MFI '10), pp. 211–216, University of Utah, Salt Lake City, Utah, USA, September 2010.

[36] Brigante C.M.N., Abbate N., Basile A., Faulisi A.C., Sessa S., "*Towards Miniaturization of a MEMS-based Wearable Motion Capture System*", IEEE Transactions on Industrial Electronics, August 2011.

[37] A. Priyanka, S. Zainab, N. Aboelmagd, and E. Naser, "*MEMS Based Integrated Navigation*", Artech House, London, UK, 2010.

[38] M. S. Grewal, L. R. Weill, and A. P. Andrews, "*Global Positioning Systems, Inertial Navigation, and Integration*", John Wiley & Sons, New York, NY, USA, 2001.

[39] A. Shke1, "*Microtechnology comes of age*", GPS World, pp. 43-50, 2011.

[40] "*MEMS Accelerometer, Gyroscope and IMU market 2008-2013*", Yole Développement, 2009.

[41] Datasheet for Honeywell μPoint HMR3600 digital magnetic compass, Honeywell International Inc., 2006.

[42] P. B. Ruffin, "*Progress in the development of gyroscopes for use in tactical weapon systems*", in SPIE Proceedings on Smart Structures and Materials 2000: Smart Electronics and MEMS, Vol. 3990, pp. 2-12, June 2000.

[43] Arnaudov R. and Angelov Y., "*Earth rotation measurement with micromechanical yaw-rate gyro*", IOP Measurement Science and Technology, Vol. 16, no. 11, pp. 2300-2303, 2005.

[44] Iozan L. I., Collin J., Pekkalin O., Hautamaki J., Takala J. and Rusu C., "*Measuring the Earth's rotation rate using a low-cost MEMS gyroscope*", in Symposium Gyro Technology, Karlsruhe (Germany), 2010.

[45] F. Ayazi, "*Multi-DOF inertial MEMS: From gaming to dead reckoning*", in IEEE International Solid-State Sensors, Actuators and Microsystems Conference, pp. 2805-2808, Beijing (China), June 2011.

[46] I. Prikhodko, S. Zotov, A. Trusov, and A. Shke1, "*Sub-degree-per-hour silicon MEMS rate sensor with 1 million Q-factor*", in IEEE 16th International Conference on Solid-State Sensors, Actuators and Microsystems, pp. 2809-2812, Beijing (China), June 2011.

[47] W. Geiger, et al., "*MEMS IMU for AHRS applications*", IEEE/ION Position Location and Navigation Symposium, pp. 225-231, Monterey, CA, May 2008.

[48] B. Chaumet, B. Leverrier, C. Rougeot, S. Bouyat, "*A new silicon tuning fork gyroscope for aerospace applications*", Symposium Gyro Technology, Karlsruhe (Germany), September 2009.

[49] D. Lapadatu, B. Blixhavn, R. Holm, T. Kvisteroy, "*SAR500 - A High-Precision High-Stability Butterfly Gyroscope with North Seeking Capability*", IEEE/ION Position Location and Navigation Symposium, Indian Wells, CA, May 3-6, 2010.

[50] J. Beitia, C. Fell., I. Okon, and P. Sweeney, "*Low cost CVG for high-grade north finders and targeting systems*", Inertial Sensors and Systems Symposium, Karlsruhe (Germany), September 2014.

[51] M. F. Zaman, A. Sharma, Z. Hao, F. Ayazi, "*A mode-matched silicon-yaw tuning-fork gyroscope with subdegree-per-hour Allan deviation bias instability*", Journal of Microelectromechanical Systems, Vol. 17, no. 6, pp. 1526-1536, December 2008.

[52] Burgess R. Johnson, Eugen Cabuz, Howard B. French, Ryan Supino, "*Development of a MEMS Gyroscope for North finding Applications*", IEEE/ION Position Location and Navigation Symposium, Indian Wells, CA, May 3-6, 2010.

[53] B. M. Renkoski, "*The effect of carouseling on MEMS IMU performance for gyrocompassing applications*," Thesis (S.M.), Massachusetts Institute of Technology, Dept. of Aeronautics and Astronautics, June 2008.

[54] L. I. Iozan, M. Kirkko-Jaakkola, J. Collin, J. Takala and C. Rusu, "*Using a MEMS gyroscope to measure the Earth's rotation for gyrocompassing applications*", IOP Measurement Science and Technology, Vol. 23, no. 2, January 2012.

[55] Song L., Zhang C. and Lu J., "*Self-alignment of full skewed RSINS: Observability analysis and full-observable Kalman Filter*", IEEE Journal of Systems Engineering and Electronics, Vol. 25, issue 1, March 2014.

[56] I. Prikhodko, S. Zotov, A. Trusov, and A. Shke1, "*What is MEMS Gyrocompassing? Comparative Analysis of Maytagging and Carouseling*", in Journal of Microelectromechanical Systems, Vol. 22, no. 6, December 2013.